

Developments in Large Scale Multi-Reference Coupled Cluster Monte Carlo



Zijun Zhao

Supervisor: Dr. Alex J. W. Thom

Yusuf Hamied Department of Chemistry
University of Cambridge

This dissertation is submitted for the degree of
Master of Philosophy

To Yi Ting

Declaration

This thesis is the result of my own work and includes nothing which is the outcome of work done in collaboration except where specifically indicated in the text.

Zijun Zhao
Aug 2022

Acknowledgements

I would like to thank, first and foremost, my supervisor, Dr Alex Thom, for guiding me through the various projects in this work, and for being a font of knowledge for all things to do with stochastic electronic structure methods, and for reviewing my code. Thank you also for all the kind words in moments of doubt and stress, and for providing ample moments of merriment in an otherwise busy year.

I would like to express heartfelt gratitude to my parents for having the unending faith in me to charter a path for myself, encouraging me to take a step into the unknown so many years ago, and what a difficult decision that must have been. Without their support, financial and otherwise, this work would have been impossible.

I'd like to thank Maria-Andreea Filip for her expert help in explaining the ins and outs of the HANDE code base, for thoroughly proofreading this work, and for her encouragements throughout. I must also thank Nicholas Lee for bringing so much life into the office, teatimes and lunchtimes, and for helping me with the more mathematical aspects of this work. I'd like to extend my gratitude to all other members of the Thom group: Chiara, Fabio, Kripa, Lila, and Daniel, for all the erudite conversations about quantum chemistry, languages, philosophy, current affairs, and more. Thank you for making my post-graduate year at Cambridge a memorable and fulfilling one.

This work used the ARCHER2 UK National Supercomputing Service (<https://www.archer2.ac.uk>).

Abstract

This work is mainly concerned with developing new methods to accelerate the convergence of large scale multi-reference coupled cluster Monte Carlo calculations. First we review the foundations of classical quantum chemical methods, and then the quantum Monte Carlo (QMC) methods that they underpin. In this work, we specifically focus on the coupled cluster Monte Carlo (CCMC) method, and to a lesser extent, the full configuration interaction quantum Monte Carlo (FCIQMC) method.

We first introduce a metric-tree based determinant searching algorithm to speed up the time consuming step in the multi-reference CCMC (MR-CCMC) algorithm of accepting clusters, spawns, and deaths. An order of magnitude reduction in computational time is typically observed with this algorithm. Several further schemes that trade eliminating small contributions for large computational savings are also introduced and benchmarked.

The previous approach shows one way to reduce the size of the reference space without minimal sacrifice in accuracy. A more tunable approach is conceived by leveraging the existing (initiator) FCIQMC algorithm to generate the model/reference space for a MR-CCMC calculation, by time-averaging the CI expansion coefficients and extracting the most important contributions by certain schemes, essentially serving as a static correlation solver coupled to the MR-CCMC algorithm. We show that this is a viable way of controlling the amount of static correlation to capture, while keeping the costs down from a ‘quasi-exponential’ scaling arising from larger complete active spaces.

We then move on to consider the projector underpinning both FCIQMC and CCMC methods, the first order Taylor series expansion to the exponential projector. Here, we consider an alternative projector, which is a Chebyshev polynomial expansion of the wall function, which satisfies several attractive properties which enables us to accommodate this drastically different projector with minimal changes to the original FCIQMC/CCMC algorithm. We also show that a significant speed-up can be achieved due in part to the automatic determination of appropriate (effective) time steps, which is implemented alongside the new projector.

Lastly, going back to the default linear projector, we consider performing the important part of the projection deterministically. We describe the new semi-stochastic CCMC (ss-CCMC) algorithm, which is shown to reduce projection noise considerably which leads to

faster statistical convergence. We also discuss its parallelisation with a mixed OpenMP/MPI parallelism, enabling it to be deployed to large systems.

Table of contents

1	Introduction	1
1.1	Review of classical electronic structure theory	1
1.1.1	Hartree–Fock theory	2
1.1.2	Møller–Plesset perturbation theory	3
1.1.3	coupled cluster theory	3
1.1.4	Full configuration interaction	5
1.2	Quantum Monte Carlo: an overview	7
1.3	Fock-space QMC methods	8
1.3.1	FCIQMC	8
1.3.2	CCMC	10
1.3.3	Estimators	11
1.3.4	Recent developments	13
2	Towards massively multi-reference coupled cluster Monte Carlo	17
2.1	Theory	17
2.1.1	Formulation of multi-reference CCMC	17
2.1.2	Excitation rank as a metric space	18
2.2	Efficient approximate search in an excitation-rank metric space	20
2.3	Compression of the model space	21
2.4	Methods and computational details	21
2.4.1	Basis sets and point group symmetries	21
2.4.2	Symmetry screening	22
2.4.3	Cluster discarding	22
2.5	Results and discussions	23
2.5.1	BK-tree	23
2.5.2	Symmetry screening	23
2.5.3	Model space compression	24
2.5.4	Cluster discarding	26

2.5.5	Binding curve of the carbon dimer	26
3	FCIQMC-tailored multi-reference CCMC	28
3.1	Motivation	28
3.2	Towards a black-box generation of MR-CCMC model space	29
3.2.1	FCIQMC as a static correlation solver	30
3.2.2	MR-CCMC as a dynamic correlation solver	30
3.3	Algorithm	31
3.3.1	Fixed-number scheme	31
3.3.2	Fixed-weight scheme	32
3.4	Results and discussion	33
3.4.1	Application to the carbon dimer	33
3.4.2	Breaking the beryllium dimer	33
3.4.3	Automerisation of cyclobutadiene	36
4	Accelerating convergence with non-linear projectors	40
4.1	Theory of projectors	40
4.1.1	The ground state projector	40
4.2	The wall-Chebyshev projector	42
4.3	Application to FCIQMC and CCMC	44
4.4	Restoring the shift update procedure	46
4.5	Results	48
5	Semi-stochastic CCMC	51
5.1	Theory	51
5.1.1	Semi-stochastic FCIQMC	51
5.1.2	Semi-stochastic CCMC	53
5.2	Selection of deterministic space	53
5.3	Algorithmic considerations and OpenMP parallelism	54
5.3.1	Initialisation	54
5.3.2	Deterministic Hamiltonian	54
5.3.3	Accumulation of the deterministic vector	56
5.3.4	OpenMP parallelism	57
5.4	MPI parallelism	57
5.4.1	Accumulation of the deterministic vector	57
5.4.2	Distribution of deterministic states	58
5.4.3	Integrated sampling scheme	59

5.5	Results and discussion	59
6	Conclusions and outlook	66
6.1	Concluding remarks	66
6.2	Future work	67
Appendix A The model space compression theorem		68
Appendix B Properties of projectors		71
B.1	Convergence properties of generators	71
B.2	Higher Taylor expansions of the exponential projector	72
B.3	Properties of the wall-Chebyshev projector	73
Appendix C The replicated sampling scheme for semi-stochastic CCMC		75
References		78

Chapter 1

Introduction

1.1 Review of classical electronic structure theory

Modern molecular electronic structure theory mainly concerns itself with low-scaling, generalisable and systematically improvable methods of electron correlation. There are, broadly speaking, two branches of the field: wavefunction methods and density functional theory (DFT). The former, which are the focus of this work, generally have high polynomial scaling, with Hartree–Fock (HF) starting at $\mathcal{O}(N^4)$, and post-HF theories starting at $\mathcal{O}(N^5)$ for Møller–Plesset second-order perturbation theory (MP2), up to full configuration interaction (FCI), which scales like $\mathcal{O}(N!)$. Though expensive, they are all systematically improvable. DFT, or more specifically, density functional approximation (DFA), has lower-order polynomial scaling, with the generalised gradient approximation (GGA) functionals having $\mathcal{O}(N^3)$ scaling, and the meta-GGA and hybrid functionals scaling as $\mathcal{O}(N^4)$. However, DFA does not provide a clear path to systematically improving the quality of calculations, although there exists the so-called Jacob’s ladder that provides a heuristic for pseudo-systematic improvability [1].

Among the wavefunction-based theories, HF provides a single-determinant, uncorrelated wavefunction that forms the basis of all other post-HF theories. The three main approaches to wavefunction-based electron correlation are many-body perturbation theories (MBPT), coupled cluster (CC) theories and configuration interaction (CI) theories.

1.1.1 Hartree–Fock theory

Hartree–Fock theory is the cornerstone of all wavefunction-based electron correlation schemes. It starts with a semi-classically motivated one-electron effective Hamiltonian:

$$\hat{\mathbf{h}}^{\text{HF}}(\mathbf{r}_i) = -\frac{1}{2}\nabla_i^2 - \sum_{\mu} \frac{1}{r_{\mu i}} + v^{\text{HF}}(\mathbf{r}_i) \quad (1.1)$$

where v^{HF} is the mean-field potential of all other electrons, and the μ indices denote nuclei. This effective Hamiltonian, also known as the *Fock operator*, $\hat{f}(\mathbf{r}_i)$, can be seen to arise from the variational extremisation of a specific N -electron trial wavefunction $|\Psi\rangle$ that consists of an anti-symmetrised (outer) product of orbitals $\{|\phi_i\rangle\}$:

$$|\Psi\rangle = \hat{\mathcal{A}} \bigotimes_i^N |\phi_i\rangle, \quad \hat{\mathcal{A}} \equiv \sum_u \sigma_u \hat{P}_u \quad (1.2)$$

where $\hat{\mathcal{A}}$ is the antisymmetriser, σ_u is the parity of the permutation brought about by \hat{P}_u . Functional extremisation of the energy expectation value of the trial wavefunction leads to Hartree–Fock solutions as stationary points:

$$\frac{\delta \langle \Psi | \hat{\mathbf{H}} | \Psi \rangle}{\delta \phi_i} = 0 \Rightarrow \hat{f}|\tilde{\phi}_i\rangle = \epsilon_i |\tilde{\phi}_i\rangle, \quad (1.3)$$

where $\{|\tilde{\phi}_i\rangle\}$ are the extremised single-particle orbitals.

In a finite basis set of atomic orbital (AO) functions η_{μ} , ϕ_i can be expanded as follows:

$$\phi_i = \sum_{\mu}^N c_{i\mu} \eta_{\mu} \quad (1.4)$$

The Roothaan–Hall equation [2, 3] enables practical computation of the Hartree–Fock equation within a finite basis set. Where \mathbf{S} is the overlap matrix between AO basis functions, the equation is given by:

$$\mathbf{FC} = \mathbf{SC}\epsilon \quad (1.5)$$

This equation is then solved iteratively to yield the HF eigenvalues and eigenvectors, for use in post-HF methods.

1.1.2 Møller–Plesset perturbation theory

Møller–Plesset perturbation theory (MPPT) [4] is an instance of MBPT. It scales as $\mathcal{O}(N^5)$, and is one of the cheapest wavefunction-based electron correlation methods available. It is size-extensive (total correlation energy scales linearly with the size of the system), but only order-by-order [5, p. 724] (the energy correction formula for each order of perturbation, as a whole, is size-extensive, but individual terms that contribute may not be). The Møller–Plesset partitioning of the electronic Hamiltonian into a diagonal, zero-order one-electron operator and a perturbation operator is given by [6, p. 80]:

$$\hat{\mathbf{H}} = \underbrace{\sum_i^n \left[\hat{\mathbf{h}}(\mathbf{r}_i) + v^{\text{HF}}(\mathbf{r}_i) \right]}_{\hat{\mathbf{H}}^{(0)}} + \underbrace{\sum_{i < j} \frac{1}{r_{ij}} - \sum_i^n v^{\text{HF}}(\mathbf{r}_i)}_{\hat{\mathbf{H}}^{(1)}} \quad (1.6)$$

As the zero-order Hamiltonian is the Fock operator, the zero-order, *i.e.* reference, wavefunctions are the Hartree–Fock wavefunctions and excitations thereof; and the zero-order energies are the sums of HF orbital energies in the reference functions. The substitution of these into the standard Rayleigh–Schrödinger perturbation equations [6, Ch. 2.2] gives:

$$E^{(2)} = \frac{1}{4} \sum_{ijab} \frac{(\langle ij|ab \rangle - \langle ij|ba \rangle)^2}{D_{ij}^{ab}} \quad (1.7)$$

where $D_{ij}^{ab} = \epsilon_i - \epsilon_a + \epsilon_j - \epsilon_b$ are the standard MBPT denominators, and

$$\langle ij|ab \rangle = \iint \phi_i^*(\mathbf{r}_1) \phi_j^*(\mathbf{r}_2) r_{12}^{-1} \phi_a(\mathbf{r}_1) \phi_b(\mathbf{r}_2) d\mathbf{r}_1 d\mathbf{r}_2 \quad (1.8)$$

are the two-electron integrals.

1.1.3 coupled cluster theory

coupled cluster theory is related to MPPT by the coupled cluster perturbation theory [5]. Starting at a higher computational complexity of $\mathcal{O}(N^6)$ for CCSD (coupled cluster singles and doubles), it provides systematic convergence towards the FCI limit with increasing truncation level than $\text{MP}n$ methods do with increasing order of perturbation. This is accomplished by the compact

form of the *exponential ansatz*:

$$\begin{aligned}
 |\Psi_{\text{CC}}\rangle &= \exp(\hat{T})|\Psi_0\rangle, \\
 \hat{T} &= \sum_{\mu}^{\kappa} \hat{T}_{\mu}, \quad \kappa \text{ being the truncation level,} \\
 \hat{T}_{\mu} &= \sum_{\substack{\text{perm.} \\ \text{unique}}} t_{i\dots}^{a\dots} \hat{\tau}_{i\dots}^{a\dots}, \quad \hat{\tau}_{i\dots}^{a\dots} = \hat{a}_a^{\dagger} \dots \hat{a}_i \dots,
 \end{aligned} \tag{1.9}$$

where the \hat{T} 's are excitation operators, the t 's are cluster amplitudes and $\hat{\tau}$'s are cluster operators.

The derivation of the unlinked coupled cluster equations usually starts with the projection of Schrödinger equation by the Møller–Plesset zero-order wavefunctions:

$$\hat{\mathbf{H}}|\Psi_{\text{CC}}^{\text{full}}\rangle = E_{\text{exact}}|\Psi_{\text{CC}}^{\text{full}}\rangle \tag{1.10a}$$

$$\Downarrow \text{ (projection by } \langle\Psi^{(0)}|)$$

$$\langle\Psi_0|\hat{\mathbf{H}}\exp(\hat{T})|\Psi_0\rangle = E_{\text{CC}} \tag{1.10b}$$

$$\langle\Psi_{i\dots}^{a\dots}|\hat{\mathbf{H}}\exp(\hat{T})|\Psi_0\rangle = E_{\text{CC}}\langle\Psi_{i\dots}^{a\dots}|\exp(\hat{T})|\Psi_0\rangle \tag{1.10c}$$

where Equation (1.10b) is known as the *energy equation*, and Equation (1.10c) are the *amplitude equations*, which are non-linear and require an iterative solution scheme.

coupled cluster singles and doubles (CCSD)

When setting the truncation level κ to 2, we obtain the CCSD equations. Proceeding from Equations (1.10b) and (1.10c), one can readily derive the ‘master equations’, involving the excitation operators \hat{T}_i 's. However in this form, these equations are not amenable to code implementation, due to the lack of explicitly constructable arrays. For example, the CCSD ‘master equations’ are given below:

$$E_{\text{CC}} = \langle\Psi_0|\hat{\mathbf{H}}(1 + \hat{T}_2 + \frac{1}{2}\hat{T}_1^2)|\Psi_0\rangle \tag{1.11a}$$

$$E_{\text{CC}}t_i^a = \langle\Psi_i^a|\hat{\mathbf{H}}(1 + \hat{T}_1 + \hat{T}_2 + \frac{1}{2}\hat{T}_1^2 + \hat{T}_1\hat{T}_2 + \frac{1}{6}\hat{T}_1^3)|\Psi_0\rangle \tag{1.11b}$$

$$\begin{aligned}
 E_{\text{CC}}(t_{ij}^{ab} + t_i^a t_j^b - t_i^b t_j^a) &= \langle\Psi_{ij}^{ab}|\hat{\mathbf{H}}(1 + \hat{T}_1 + \frac{1}{2}\hat{T}_1^2 + \frac{1}{6}\hat{T}_1^3 \\
 &+ \frac{1}{24}\hat{T}_1^4 + \hat{T}_2 + \frac{1}{2}\hat{T}_2^2 + \hat{T}_2\hat{T}_1 + \frac{1}{2}\hat{T}_1^2\hat{T}_2)|\Psi_0\rangle
 \end{aligned} \tag{1.11c}$$

There are three, fundamentally equivalent, general strategies to generate so-called factorised, efficient and computer-friendly equations from the master equations:

1. **Configuration-space derivation** relies on the manipulation of first-quantisation expectation values based on the Slater-Condon rules [7, p. 70]. However, considerable effort is needed in this error-prone process to eliminate unknowns [6, Ch. 9.3.1], which becomes unmanageable quickly, even at the CCSDT level.
2. **Algebraic derivation** relies repeated applications of the generalised Wick's theorem [8] in second quantisation. This is equivalent to the previous derivation, but the second-quantisation formulation makes it more amenable to string-based computer manipulation [9].
3. **Diagrammatic derivation** is based on the representation of the algebraic derivation with Hugenholtz diagrams. It greatly simplifies the contractions between operators and the number of diagrams scales more favorably than the number of terms in configuration-space or algebraic derivations, due to the linked-diagram theorem [6, Ch. 5.8].

The CCSD(T) (coupled cluster with singles and doubles and perturbative triples) method [10] is celebrated as the 'gold standard' of quantum chemistry. However, it only provide sub-milihartree energy errors consistently near equilibrium geometries, and in systems free from orbital (quasi)degeneracies [11]. Much of chemistry, however, studies the energetics of bond-breaking, or that of exotic molecules (for example, the carbon and chromium dimers) where orbital degeneracies are commonplace. In these cases, CCSD(T)/[T] produce completely unphysical potential energy surfaces (PEsEs) littered with spurious energy barriers, due to divergences in the MBPT denominators when the involved orbitals are (quasi)degenerate, also known as the *intruder state problem* [5, Ch. 14.5]. In these cases, multi-reference coupled cluster methods are generally required. These methods correct the failures of the single-reference method by treating configurations that are expected to be significantly occupied on similar or equal footing as the reference configuration in single reference methods (for a comprehensive review, see [12]).

However, the derivation of the coupled cluster equations (and their perturbative corrections) at arbitrary truncation level is, regardless of the approach used, a challenging and error-prone process. This is even more true for MRCC theories. The challenge is made worse as there is no clear way to generalise a single-reference implementation to a multi-reference one.

1.1.4 Full configuration interaction

Full configuration interaction (FCI), also known as exact diagonalisation, is the exact eigen-decomposition of a Hamiltonian in a given basis set. FCI yields the exact ground (and excited) state energies, and FCI calculations are sought after as the true benchmark for other electronic

structure methods. A Hartree–Fock (HF) calculation with M basis functions and N electrons gives a set of $2M$ one-particle spin-orbitals ψ_i , and the approximate ground state, $|\Psi_{\text{HF}}\rangle$, for the system is the one in which the electrons fill the eigenfunctions according to the *Aufbau* principle, here given in a second-quantisation occupation-number (ON) vector [5, p. 1]:

$$|\Psi_{\text{HF}}\rangle = |\underbrace{1, \dots, 1}_N, \underbrace{0, \dots, 0}_{2M-N}\rangle \quad (1.12)$$

The basis for FCI is the set of all possible excitations from $|\Psi_{\text{HF}}\rangle$:

$$|k_1, k_2, \dots, k_{2M}\rangle, \quad k_P = \begin{cases} 1 & \text{if } \psi_P \text{ occupied} \\ 0 & \text{if } \psi_P \text{ unoccupied} \end{cases}, \quad (1.13)$$

with the total number of occupied states fixed at N . For an $M_s = 0$ system, there will be $\binom{M}{N/2}^2$ basis functions for FCI, hence its formal factorial ($\mathcal{O}(N!)$) scaling¹.

The most efficient FCI algorithms are based on the vectorised string formalism of Handy and Knowles [14], and improvements thereof [15]; for a review, see [16].

The largest FCI calculations to date involve at most about 10^{10} Slater determinants, on relatively modest systems such as N_2 [17], AIP [18], pentacene and Cr_3 [19].

If the allowed excitations are limited in Equation (1.13), then a series of approximations to full CI can be obtained, known as CISD (CI with singles and doubles excitations), CISDT (triples), CISDQ (quadruples), CISDTQ5, and so on. Their scaling is $\mathcal{O}(N^{2P+2})$, where P is the truncation level [16]. However, unlike other systematically truncated methods such as Møller–Plesset perturbation theory and coupled cluster theory, truncations of FCI are not size-consistent (*i.e.*, at infinite separation of parts of a system, the energy of the whole system is *not* equal to the sum of these parts), and as a whole less useful, especially for larger systems. The Davidson correction [20] (also known as the CISD+Q method) mitigates this problem, and the quadratic CISD (QCISD, QCISD(T) if a perturbative triples correction is added) [21] method is size-consistent.

¹Not to be confused with the ‘exponential wall’ first introduced by Walter Kohn in his Nobel lecture [13], which is about the number of variational parameters, which scales like p^{3N} , with p being the number of variational parameters per spatial degree of freedom

1.2 Quantum Monte Carlo: an overview

Quantum Monte Carlo (QMC) methods are a class of post-mean-field methods that solves the Schrödinger equation by stochastic integration in an appropriate phase space in contrast to the exact numerical integration in deterministic electronic structure methods.

Almost all of the QMC methods, with the notable exception of variational Monte Carlo, start with the *projector method*, based on the *time-dependent Schrödinger equation*:

$$i\frac{\partial\Psi}{\partial t} = \hat{\mathbf{H}}\Psi \quad (1.14)$$

A Wick rotation ($it \rightarrow \tau$) gives the *imaginary-time Schrödinger equation*:

$$\frac{\partial\Psi}{\partial\tau} = -\hat{\mathbf{H}}\Psi \quad (1.15)$$

which can be formally integrated to give:

$$\Psi(\tau) = \exp(-\tau(\hat{\mathbf{H}} - S))\Psi(0) \quad (1.16)$$

This can be regarded as the ‘master equation’ for the projector methods. The constant of integration, S , is also known as the arbitrary ‘shift’ parameter, explained more in detail in [Section 1.3.3](#).

QMC methods generally suffer from the Fermion sign problem [22], which is the incompatibility of the Monte Carlo algorithm which represents a Fermionic wavefunction Ψ as a collection of walkers with positive and negative weights, and the interpretation of $|\Psi|^2$ as a probability distribution function, meaning that most random-walk paths will eventually suffer from numerical cancellation, leaving the real contributions exponentially small as the algorithm progresses [23, p. 15.14].

At this point, the field diverges along the choice of the form of Ψ , into broadly two categories:

- **Real-space QMC** methods use real-space, continuous functions for Ψ . These include variational Monte Carlo (VMC) and diffusion Monte Carlo (DMC), where the former is now commonly used to prepare trial wavefunctions for the latter. For a recent review on the state-of-the art of these methods, see [24]. DMC generally ameliorates the sign problem by imposing the *fixed-node approximation* [25, 26], which imposes an infinite repulsive potential at nodal (hyper-)surfaces of a wavefunction of the same system taken from a cheaper theory, with Hartree–Fock (HF) and Kohn–Sham density functional theory (KS-DFT) being commonly used. A ‘self-healing’ DMC algorithm was proposed [27] that iteratively improves the nodal structure by iteratively improving the nodal structure.

- **Fock-space QMC** methods use linear combinations of Slater determinants for Ψ . These include the auxiliary-field quantum Monte Carlo (AFQMC) [28], full configuration-interaction quantum Monte Carlo (FCIQMC) [29], coupled cluster Monte Carlo (CCMC) [30] and density matrix quantum Monte Carlo (DMQMC) [31]. As Slater determinants are anti-symmetrised, there is no problem of converging to a Bosonic solution, as can happen in DMC, and this reduces the severity of the sign problem somewhat. AFQMC stands in its own sub-class, and suppresses the sign problem with the constrained path [32] and phaseless [33] approximations. The remaining methods belongs to a family of related algorithms, where the sign problem is addressed elegantly by *walker annihilation* [34]. This class of algorithms are implemented in the HANDE-QMC package [35].

1.3 Fock-space QMC methods

1.3.1 FCIQMC

Theory

Continuing from Equation (1.16), we can choose an initial trial wavefunction $|\Phi\rangle$ (usually this is the Hartree–Fock solution, but the only constraint is that it has non-zero overlap with the exact ground state). We can expand $|\Phi\rangle$ formally in a basis of the FCI eigenvectors:

$$|\Phi\rangle = \sum_i c_i |\Psi_i^{\text{FCI}}\rangle \quad (1.17)$$

where each of the FCI eigenvectors are themselves linear combinations of various excitations of Ψ^{HF} . The exponential projector has the following effect:

$$e^{-\tau(\hat{\mathbf{H}}-S)}|\Phi\rangle = \sum_i e^{-\tau(E_i-S)}|\Psi_i^{\text{FCI}}\rangle, \quad (1.18)$$

where E_i are the exact eigenvalues of the Hamiltonian. Hence, the effect of the projector is to exponentially decay away excited FCI states:

$$\lim_{\tau \rightarrow \infty} e^{-\tau(\hat{\mathbf{H}}-S)}|\Phi\rangle \propto |\Psi_0^{\text{FCI}}\rangle, \text{ for } S = E_0 \quad (1.19)$$

At this point, the equation is written in an iterative form

$$\Psi(\tau + \delta\tau) = e^{-\delta\tau(\hat{\mathbf{H}}-S)}\Psi(\tau) \quad (1.20)$$

and approximated by a first-order Taylor expansion

$$\Psi(\tau + \delta\tau) = [1 - \delta\tau(\hat{\mathbf{H}} - S)]\Psi(\tau) \quad (1.21)$$

Left-multiplying with $\langle D_i |$ and integrating to reveal the CI coefficients, we have

$$\begin{aligned} c_i(\tau + \delta\tau) &= c_i(\tau) \\ &- \delta\tau(H_{ii} - S)c_i(\tau) - \delta\tau \sum_{j \neq i} H_{ij}c_j(\tau) \end{aligned} \quad (1.22)$$

The time step, $\delta\tau$ obeys the relation, in common with DMC

$$\delta\tau \leq \frac{2}{E_{\max} - E_0} \quad (1.23)$$

with the denominator known as the *spectral radius* of $\hat{\mathbf{H}}$, and is easily seen as a result of the requirement that the following power iterations do not diverge:

$$\lim_{N \rightarrow \infty} [1 - \delta\tau(\hat{\mathbf{H}} - S)]^N \Psi(0) \quad (1.24)$$

Algorithm

Equation (1.22) can be now transparently translated into a walker-based Monte Carlo algorithm, which is schematically depicted in Figure 1.1, where signed walkers reside on determinants $|D_i\rangle$ whose signed walker population signifies their CI coefficients c_i :

1. **Initialisation:** an initial distribution of walkers is generated, usually just on the reference determinant $|D_0\rangle$.
2. **Cloning and death:** the diagonal action of the Hamiltonian is sampled, where the walker ‘dies’ or is ‘cloned’, depending on the sign of the probability, on the same determinant with a probability proportional to $\delta\tau(H_{ii} - S)c_i(\tau)$.
3. **Spawning:** the off-diagonal action of the Hamiltonian is sampled, where for each walker, a walker can be created on a connected determinant (*i.e.*, $H_{ij} \neq 0$, in other words, the bit-string distance or half the Hamming distance of \mathbf{i} and \mathbf{j} is no more than two), with a probability proportional to $\delta\tau H_{ij}$, depending on the excitation generator used (see [29, 36–38]).
4. **Annihilation:** for every determinant that is populated, positive and negative walkers cancel each other out. This prevents the sign problem where the representations of Ψ and

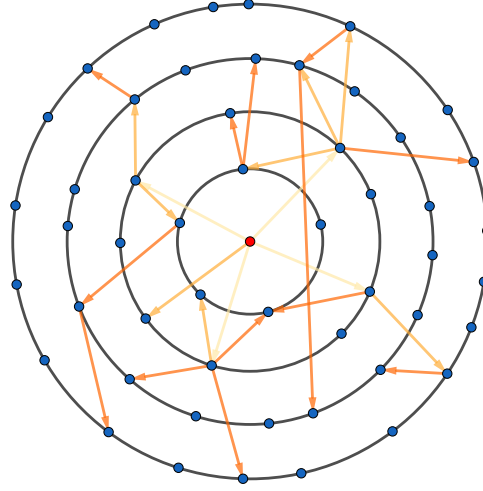


Fig. 1.1 Schematic representation of the FCIQMC propagation. The central red dot is the reference determinant, and the arrows represent spawning, with darker colors representing more recent Monte Carlo moves. The innermost ring represent the space of single excitations, and the next doubles, and so on. Assuming a restricted HF reference, only double excitations will be spawned in the first iteration due to Brillouin's theorem [7, p. 128].

$-\Psi$ grow together, causing uncontrollable noise [34]. This concludes a Monte Carlo step, return to step 2.

At the beginning of a calculation, the arbitrary shift is generally fixed at the (HF) reference energy, enabling exponential growth of total walker population, driven by the scarcity of death events. However, after a system-specific target population is reached, the shift is allowed to vary, such that it produces a stable population, and become negative to match E_{corr} . The target population is usually determined by running an unrelaxed calculation (*i.e.*, with a very large target population), and observing the height of a plateau feature in a plot of total population against iteration.

1.3.2 CCMC

The formulation of CCMC closely matches that of FCIQMC, with the difference that instead of residing on determinants, walkers reside on *excitors*, \hat{a}_n , defined as $\hat{a}_n|D_0\rangle = |D_n\rangle$. Replacing the FCI wavefunction by the coupled cluster *ansatz* in Equation (1.21) and left-multiplying by $\langle D_i|$ gives

$$\begin{aligned} \langle D_i|\Psi^{\text{CC}}(\tau + \delta\tau)\rangle = & \langle D_i|\Psi^{\text{CC}}(\tau)\rangle \\ & - \delta\tau \langle D_i|(\hat{\mathbf{H}} - S)|\Psi^{\text{CC}}(\tau)\rangle \end{aligned} \quad (1.25)$$

The coupled cluster *ansatz* parametrises the wavefunction with cluster amplitudes in a non-linear fashion (see Equation (1.9)). The mapping of CI coefficients to cluster amplitudes can be done by a simple projection, which reveals contributions from multiple clusters. For example in a CCSD wavefunction (*i.e.*, $\hat{T} = \hat{T}_1 + \hat{T}_2$)

$$\langle D_{ij}^{ab} | e^{\hat{T}} \Psi^{\text{HF}} \rangle = t_{ij}^{ab} + t_i^a t_j^b - t_i^b t_j^a \quad (1.26)$$

with the negative sign arising from the fact that $\hat{a}_b^\dagger \hat{a}_i \hat{a}_a^\dagger \hat{a}_j = -\hat{a}_a^\dagger \hat{a}_i \hat{a}_b^\dagger \hat{a}_j$, due to the anti-commutation relations of the second-quantised creation and annihilation operators [5, p. 8]. Terms like t_{ij}^{ab} are known as *non-composite* cluster amplitudes, and the rest as *composite* cluster amplitudes. Here we make the approximation that composite clusters have much smaller contributions than the non-composite ones, their changes will be negligible per time step, and hence we can cancel out the $\mathcal{O}(\hat{T}^2)$ contributions on both sides to write

$$t_i(\tau + \delta\tau) = t_i(\tau) - \delta\tau \langle D_i | (\hat{\mathbf{H}} - S) | \Psi^{\text{CC}}(\tau) \rangle \quad (1.27)$$

Compared to FCIQMC, an additional step needs to be performed for each Monte Carlo iteration: the sampling of the exponential *ansatz*: for N_{ex} total walkers, also called *excips* in CCMC, $\mathcal{O}(N_{\text{ex}})$ clusters are formed randomly by combining them according to specific biasing rules [39].

Finally, the intermediate normalisation ([6, p. 20]) is redefined to give the CCMC *ansatz*:

$$|\Psi_{\text{CCMC}}\rangle = N_0 e^{\hat{T}/N_0} |D_0\rangle, \quad (1.28)$$

which introduces the reference population as a new independent variable, solving the problem that Equation (1.25) cannot update the case for $|D_i\rangle = |D_0\rangle$.

1.3.3 Estimators

As stochastic algorithms, all physical observables in FCIQMC and CCMC are approximated by estimators, the simplest of which is the estimator for the expectation value of a variable O : $\langle O \rangle = \frac{1}{N} \sum_{i=1}^N O_i$.

However the variance of the variable is also needed to gauge the error in the estimates. Naively this can involve time auto-correlation functions, reviewed in [40, Sec. III], which is computationally expensive and requires some subjective choices.

A more economical method, known as the *blocking method*, was recapitulated in the same paper. The HANDE-QMC package uses the blocking method [41] to obtain error bounds on all observable quantities.

The main realisation behind the blocking method is that the expectation value and the variance are invariant under a *blocking transformation* where a new data set of half the size is obtained from taking sets of averages of adjacent data points in the original data set; and also that the lower bound of the variance approaches the true value every time a blocking transformation is applied.

The shift parameter

As alluded to above, the arbitrary shift parameter S is kept constant at the start of a simulation to grow the total population so that the correct sign structure of the ground state is represented, and then allowed to relax to serve as an estimator of the ground state energy. The update is performed every A steps, and is given by [29]:

$$S(\tau + A\delta\tau) = S(\tau) - \frac{\zeta}{A\delta\tau} \ln \frac{N_w(\tau + A\delta\tau)}{N_w(\tau)} \quad (1.29)$$

where N_w is the number of walkers as a function of imaginary time, and ζ is a dampening factor. The shift is guaranteed to converge onto the true ground state energy as Equation (1.29) reduces the shift if there's a net gain in walkers in a set of A steps, signifying that the shift is higher than the ground state energy (alternatively $\mathbf{H} - S\mathbf{I}$ has at least one positive eigenvalue); and conversely the shift is raised if it is lower than the ground state energy. The shift remains unchanged When the population is stationary, signifying that the zero eigenvector, *i.e.*, the ground state vector of $\mathbf{H} - S\mathbf{I}$ has been located.

The projected energy

Another, independent estimator for energy is the *projected energy*:

$$\begin{aligned} E_{\text{proj}}(\tau) &= \frac{\langle D_0 | \hat{\mathbf{H}} | \Psi(\tau) \rangle}{\langle D_0 | \Psi(\tau) \rangle} \\ &= \langle D_0 | \hat{\mathbf{H}} | D_0 \rangle \frac{N_0(\tau)}{N_0(\tau)} + \sum_{j \neq 0} \langle D_j | \hat{\mathbf{H}} | D_0 \rangle \frac{N_j(\tau)}{N_0(\tau)} \\ &= E^{\text{HF}} + \sum_{j \neq 0} \langle D_j | \hat{\mathbf{H}} | D_0 \rangle \frac{N_j(\tau)}{N_0(\tau)} \end{aligned} \quad (1.30)$$

In FCIQMC, after each iteration, this sum is explicitly performed over singly and doubly excited determinants with respect to the HF determinant; in CCMC, as the parametrisation is non-linear, the numerator in Equation (1.30) would contain products of single cluster amplitudes, rendering direct looping infeasible. In practice, the numerator and the denominator are accumulated as

two separate variables in the calculation, and the estimator for the projected energy is given by the ratio of the averages, with its error estimate being the covariance of the two quantities [41, 34].

1.3.4 Recent developments

FCIQMC and CCMC are both still under active development, in the HANDE-QMC package [35] (which also includes DMQMC) and the NECI package [38] (which only has FCIQMC).

The initiator approximation

Proposed for FCIQMC in [42] and adapted for CCMC [39], the initiator approximation reduces the total number of walkers needed to reach convergence. It works by making some determinants *initiators*, which are allowed to spawn onto previously unoccupied determinants. Non-initiators are only allowed to spawn onto previously occupied determinants, unless two or more non-initiators spawn onto the same unoccupied determinant. The initiator space can be made dynamic by granting the initiator status to determinants with populations larger than a user-set threshold (the ‘initiator threshold’).

However the approximation does introduce a systematic error in the converged energy that becomes zero in the limit of very large walker populations. Various proposals were introduced to remove the *initiator error*, including using extrapolation [39, Sec. VI and Appendix A], or with a second-order Epstein–Nesbet (EN2) perturbation theory correction based on discarded spawning attempts [43].

The less severe sign problem in i-FCIQMC has been attributed to a higher rate of annihilation, suppressing the growth of an unphysical solution to the FCIQMC dynamical equations [34, Sec. VI].

Recasting of FCIQMC in the fast randomised iteration framework

Recently, the Berkelbach group has advanced a re-formulation of FCIQMC [44–46] in the language of the fast randomised iteration (FRI) framework [47]. In their approach, FCIQMC is a specific instance of what they term the FRI-FCI method, which is comprised of 1) a vector compression scheme, 2) a ‘hierarchical’ matrix factorisation scheme in which a dense-matrix-compressed-vector multiplication can be performed as a series of sparse matrix-compressed-vector multiplications, and finally, 3) a sampling scheme, which is used in compressing the vectors and factorising (and compressing in the process) the Hamiltonian. It has been shown that this approach yields FCI accuracy at up to 1000 times higher efficiency than vanilla FCIQMC.

The quasi-Newton acceleration

Proposed in [48], in which Equation (1.21) is viewed as a steepest-descent update equation, and naturally replaceable by any other optimisation algorithm:

$$\mathbf{c}(\tau + \delta\tau) = \mathbf{c}(\tau) - \delta\tau \mathbf{A}\mathbf{g}(\tau) \quad (1.31)$$

where $\mathbf{g} = (\mathbf{H} - \mathbf{I}S)\mathbf{c}$ is the gradient, and $\mathbf{A} = \tilde{\mathbf{H}}^{-1}$ is the Hessian:

$$\tilde{H}_{ij} = \frac{\partial g_i}{\partial c_j} \propto \langle D_i | \hat{\mathbf{H}} - S | D_j \rangle \quad (1.32)$$

The inversion of the exact Hessian is manifestly exponentially expensive. However, as the FCI Hamiltonian is diagonally dominant, $\tilde{\mathbf{H}}$ can be approximated by zeroing all the off-diagonal elements. This essentially has the effect of weighting the Hamiltonian elements by appropriate sums of HF orbital energies in spawning:

$$p_{\text{spawn}}(\mathbf{i} \rightarrow \mathbf{j}) \propto \delta\tau \frac{\langle D_i | \hat{\mathbf{H}} | D_j \rangle}{E(D_j)} \quad (1.33)$$

where $E(D_j)$ is the difference in energy between D_i and D_0 :

$$E(D_j) = \sum_{i \text{ in } \mathbf{j}} \epsilon_i - \sum_{i' \text{ in } \mathbf{0}} \epsilon_{i'} \quad (1.34)$$

However, the death step (diagonal action of the Hamiltonian), originally written as

$$p_{\text{death}}(\mathbf{i}) \propto \delta\tau \langle D_i | \hat{\mathbf{H}} - S | D_i \rangle \quad (1.35)$$

cannot simply be scaled due to the determinant-dependence of the scaling factor, which can cause the true solution to drift if S is not equal the correct energy (S , in this sense, is a less true estimator of the energy as the imaginary time evolution is discretised). To address this, the death step is modified with the introduction of a new population control variable ρ :

$$p_{\text{death}} \propto \delta\tau \left[\frac{\langle D_i | \hat{\mathbf{H}} - E_{\text{proj}} | D_i \rangle}{E(D_i)} + \rho(E_{\text{proj}} - S) \right] \quad (1.36)$$

where the projected energy E_{proj} will always be the true energy if we have the true solution, and hence will not cause a similar drift if the shift is used.

The quasi-Newton algorithm in HANDE allows further a ‘quasi-Newton threshold’, Δ_{QN} , which is a cut-off value for the small $E(D_j)$, and serves as a numeric device to avoid division by small numbers, and ρ is usually set to the same value as Δ_{QN} .

Jacobi preconditioning

Suggested in [49], in common with the quasi-Newton approach, the starting point is viewing the imaginary time propagation from a different angle, this time as an iterative eigenvalue problem, like the power method that the projector method is a reformulation of, or the Davidson’s method ([50]).

$$\mathbf{c}^{(n+1)} = \mathbf{c}^{(n)} - \gamma^{(n)} \mathbf{P}^{-1}[(\mathbf{H} - \mathbf{I}S^{(n)})\mathbf{c}^{(n)}] \quad (1.37)$$

where \mathbf{P} is the *preconditioner*, which is the identity matrix in the original FCIQMC and CCMC algorithms. Note the equivalence of this equation with Equation (1.31) when $\gamma^{(n)} = \delta\tau$. The Jacobi preconditioner is given by

$$P_{ij} = (H_{ii} - S)\delta_{ij} \quad (1.38)$$

This then can be straightforwardly translated to simple modifications in the spawning (off-diagonal) and death (diagonal) routines. In spawning, each spawned walker will have its amplitude multiplied by $1/(H_{ii} - S)$, and in death, every determinant will have its amplitude multiplied by $1 - \delta\tau$. A further modification to ensure controllable stochastic noise is to allow each walker to have multiple spawning attempts N_{spawn} , with the resulting spawns’ amplitudes divided by N_{spawn} .

The Jacobi preconditioner has allowed much larger (up to unity is reported) time steps, however, the need to use a rather large N_{spawn} , essentially dividing $\delta\tau$ by N_{spawn} , cancels most of the time savings (see for example figure 6 in [49]).

Full non-composite and even selection

These two modifications are relevant for CCMC only. A consequence of the original CCMC algorithm is that both the spawning and death probabilities of a cluster are proportional to

$$\frac{w_e}{n_a p_{\text{select}}(e)} = \frac{2^{s+1}}{s!} \left(\frac{N_{\text{ex}}}{N_0} \right)^{s-1} \quad (1.39)$$

where $p_{\text{select}}(e)$ is the probability of selecting a combination of excitors e with the product of weights on them being w_e , and s is the number of excitors involved in forming the cluster. Given that $N_{\text{ex}}/N_0 > 1$ normally, this means that large, composite clusters have much larger

spawning and death probabilities compared to non-composite ones. This causes what is known as ‘blooms’, in which a large amount of walkers are generated on a relatively unimportant excitor, potentially causing the overlap between the stochastic wavefunction and the true wavefunction to be too small for continued projection, and also creating load balancing and memory issues.

The solutions proposed in [51] aim to address blooms by fixing $w_e/p_{\text{select}}(e)$ to be unity. The first and partial solution is termed *full non-composite*, which fixes the above-mentioned quantity to unity only for the non-composite clusters, *i.e.*, for $s = 0, 1$, by explicit looping of all stored excitors. This approach already shows significant improvements in calculation stability and especially reduced noise in the projected energy, as most single and double excitations are instantaneously stored.

The second solution essentially removes the possibility of blooms, by requiring that the quantity be fixed at unity for all s , arriving at

$$n_a = N_{\text{ex}} \sum_{s=0}^{l+2} \frac{1}{s!} \left(\frac{N_{\text{ex}}}{N_0} \right)^{s-1} \quad (1.40)$$

which shows that the number of attempts scales exponentially with higher truncation levels. It then suggests ways that this exponential increase may be alleviated, by *truncated selection*. However in practice even selection does increase the computational cost appreciably. A cheaper replacement is using full non-composite with the `cluster_multispawn_threshold` keyword, which splits up potential blooms into multiple spawning attempts.

Chapter 2

Towards massively multi-reference coupled cluster Monte Carlo

In this chapter, we propose a series of algorithmic adaptations that enable the multi-reference formulation of CCMC to be applied to large reference spaces efficiently. These included a BK-tree based determinantal search algorithm, a symmetry-screening procedure, and a cluster discarding threshold. Each of these are individually studied, and a combination of them are applied to the carbon dimer to obtain a binding curve that is close to FCIQMC quality.

2.1 Theory

2.1.1 Formulation of multi-reference CCMC

The multi-reference formulation of the CCMC algorithm (MR-CCMC) [52] implemented a multi-reference method that retained a single-reference formalism, in common with what [12, Chap. 5] termed as the SRMRCC methods. The flexibility of the HANDE code base allowed the MR-CCMC adaptation to consist of a set of minimal changes, made to the existing CCMC code, bypassing what would be a challenging process in deterministic codes. Essentially, for a truncation level P , the algorithm allows any number of determinants to become a ‘secondary reference’ determinant, and store excitors that are within P excitations from *any* references (instead of just the HF determinant), and allow clusters to form that are within $P + 2$ excitations from *any* reference. We call the set of references the model or reference space. To summarise, the algorithmic modifications of the original CCMC are:

- Store all the secondary references in a certain searchable data structure, and additionally store the highest excitation level from the reference determinant among the secondary references, k_{\max} .

- **Cluster expansion:** allow clusters with excitation level of up to $k_{\max} + P + 2$ to form, instead of $P + 2$.
- **Spawning:** for a randomly generated spawnee (*i.e.*, $\langle D_n |$), check that it is within P excitations of *any* secondary references.
- **Cloning/death:** allow death on excitors that are within P excitations from *any* secondary references.

2.1.2 Excitation rank as a metric space

Natural to the implementation of CCMC as a Fock-space QMC method, determinants are stored in the bit-string representation:

$$|1_M, 0_{M-1}, \dots, 1_3, 0_2, 1_1\rangle \Rightarrow '10\dots 101', \quad (2.1)$$

note that the highest index comes first in the occupation-number vector notation, as in the bit-string representation. The excitation level between two determinants (with the same number of electrons) is defined as half the number of *unique* creation and annihilation operators needed between them such that they have unit overlap. For example,

$$1 = \langle 1, 0, 0, 1 | \hat{a}_4^\dagger \hat{a}_3 \hat{a}_2 \hat{a}_1^\dagger | 0, 1, 1, 0 \rangle, \quad (2.2)$$

the excitation level from one determinant to the other is $4/2 = 2$. In the bit-string representation, this is efficiently evaluated with a bit-wise exclusive-OR (XOR or \oplus) operation ($A \oplus B$ is true if *only* one of A or B is true), followed by a bit-counting operation:

$$\text{count_bit}(1001 \oplus 0110)/2 = \text{count_bit}(1111)/2 = 2. \quad (2.3)$$

Where $\text{count_bit}(f_1 \oplus f_2)$ is simply the *Hamming distance* [53] between two bit-strings f_1 and f_2 . We can now define the excitation-rank as a metric being equal to half of the Hamming distance between two bit-strings of equal number of set bits.

The Hamming distance is a well-known example of a (discrete) metric, which satisfies all properties of a metric:

- **Non-negativity:** the distance between A and B is always non-negative, with zero distance obtained if and only if the A and B are identical;
- **Reversibility:** the distance between A and B is the same as the distance between B to A ;

- **Triangle inequality:** the distance between A and B is always less than or equal to the distance between A to B via a third point C .

Figure 2.1 illustrates that the effect of including secondary references is to modify the model (darker colors) and spawning (lighter colors) spaces. To aid visualisation, the discrete excitation-rank metric space is visualised in the continuous Euclidean metric space. This visualization however can be misleading, especially in a limited basis set, but even in the infinite basis size limit: for a system with n electrons and infinite orbitals, the highest excitation level is n , but any two maximally excited determinants are at most n excitations apart, that is to say, the triangle inequality, in this case $n + n \leq 2n$, gives a poor upper bound to the excitation rank between two determinants in this metric space. As a consequence, again in the imperfect visual language, the largest circle should fit more ‘snugly’ around the spawning spaces.

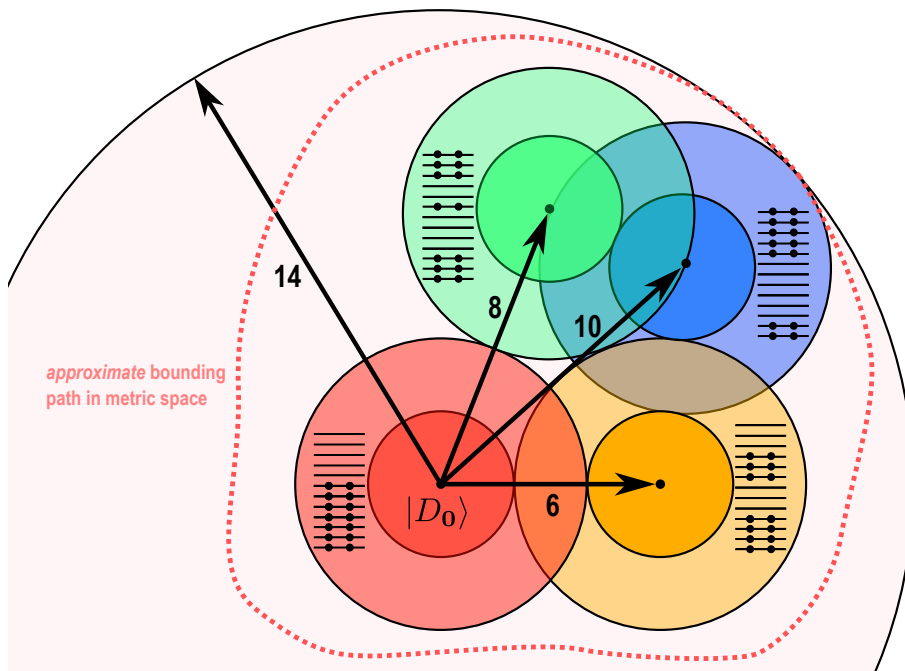


Fig. 2.1 An illustration of the encoded (dark colors) and spawning (light colors) spaces in a MR-MC-CCSD calculation with three secondary references, 6 (yellow), 8 (green), and 10 (blue) excitations away from the reference determinant. The encoded space, being up to P excitations away from the reference, represents the space in which excitors (or cluster amplitudes) are stored, and the spawning space, which are two excitations higher than the encoded space, represent the set of clusters that spawning attempts can be made. The biggest circle is the bounding path in the metric space, within which clusters can be generated, in this case up to $10 + 2 + 2 = 14$ -fold excitation from the reference can be considered. As explained in the text, although the circle lends itself to a simpler geometrical understanding, the non-geometricity of the metric space results in a more ‘snug’ bounding path represented by the dashed red path.

2.2 Efficient approximate search in an excitation-rank metric space

In the overview of the modifications entailed by MR-CCMC at the start of this chapter, we stressed that the secondary references need to be stored in a searchable format. This is because in the spawning and cloning/death routines we need to check whether an arbitrary determinant is within P excitations away from *any* secondary reference determinant. When the number of secondary references is small, checking the references one-by-one would not be rate-limiting. However the computational cost of this simple checking process can become significant when a large set of secondary references, for example, a complete active space (CAS), is used. The task we need to perform is essentially one of approximate string matching: similar to a fuzzy word search in a dictionary, only with bit-strings and a ‘dictionary’ of secondary references. A commonly used data structure for this task is the BK tree [54], depicted in Figure 2.2. The data structure is built from a list of secondary references. The BK tree has the property that all sub-trees contain nodes with the same excitation level to the node one level up. For example, all secondary references in the bottom branch of Figure 2.2 are single excitations from the reference determinant. Once built, the data structure allows approximate matching queries at a time complexity of $\mathcal{O}(\log(N))$. Figure 2.3 illustrates the building and searching algorithms.

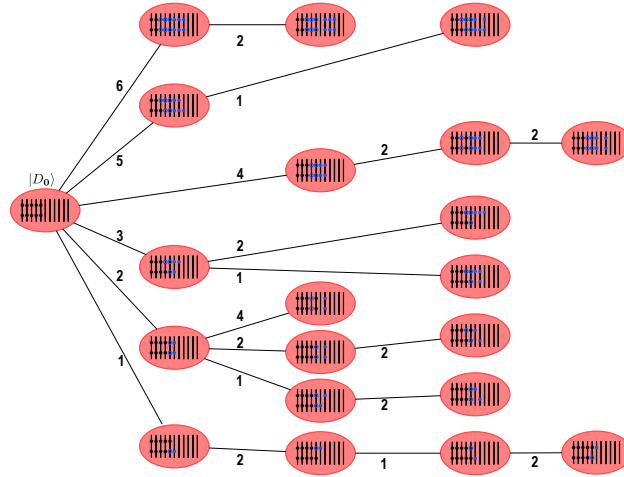


Fig. 2.2 The BK tree can conduct efficient nearest neighbour searches in a discrete metric space, like the excitation rank. In this figure a BK tree built from 20 arbitrary determinants is shown. The topology of the tree is not unique, and is dependent on the order the nodes were added to the tree.

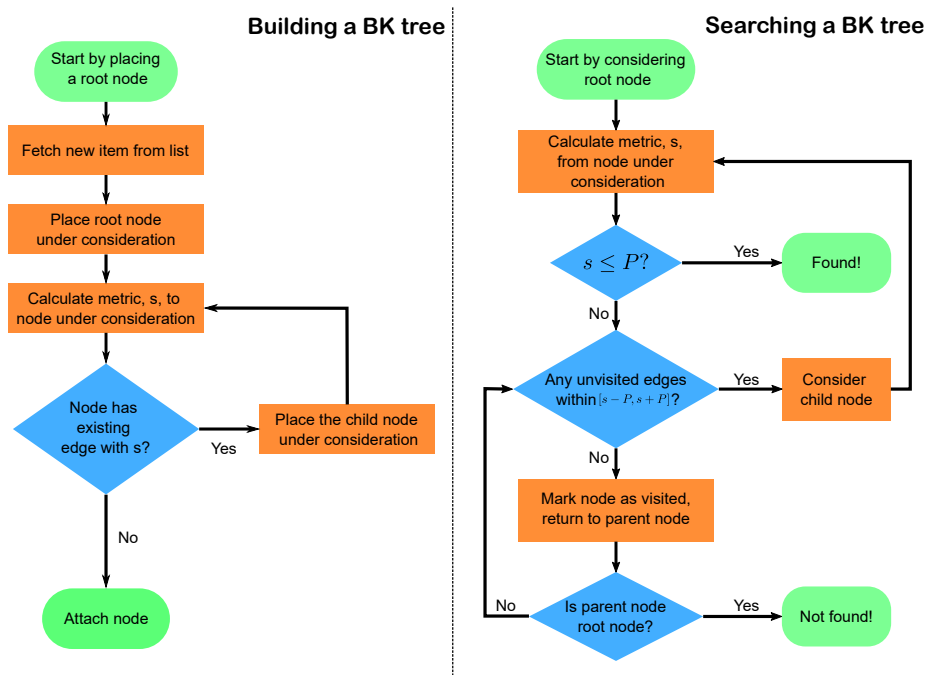


Fig. 2.3 Flowcharts for the building and searching of a BK-tree.

2.3 Compression of the model space

Whereas many classical MRCC methods work with CASes, the MR-CCMC algorithm as presented here is highly flexible as to the shape of the model space, and as such can be considered a general model space (GMS) method [12]. This enables us to consider arbitrary subsets of the CAS as the model space, and fine-tune the balance between cost and accuracy. We outline the formulation of such a compression method in [Appendix A](#).

2.4 Methods and computational details

2.4.1 Basis sets and point group symmetries

In this work we will study the carbon and beryllium (in [Chapter 3](#)) dimers. For these systems, Dunning's cc-pVXZ basis sets are used [55]. The required electron integrals are generated by the Psi4 [56] and PySCF [57] packages. The electron integrals are generated in the D_{2h} point group symmetry and transformed into the basis of \hat{L}_z eigenfunctions based on the TransLz.f90 script provided in the NECI package [38], which we re-wrote to interface with PySCF. Unless otherwise noted, the core $1s$ electrons of C_2 are frozen. The 'heat bath' excitation generator [36] is used whenever possible, otherwise the renormalised excitation generator [58] is used.

The use of the \hat{L}_z eigenfunctions helps not only further reduce size of the symmetry sector, but also helps distinguish low-lying states that would descend to the same irreducible representation (‘irrep’) in D_{2h} . For C_2 , this would be the $^1\Sigma_g^+$ state and the $^1\Delta_g$ states, which both descend into the 1A_g state in D_{2h} . The two states approach and cross each other [59, 60], which would prove challenging, if not impossible, to distinguish in D_{2h} .

2.4.2 Symmetry screening

The full $(8e, 8o)$ CAS model space of C_2 contains $(^8C_4)^2 = 4900$ model space determinants that have $M_s = 0$. However, like most classical quantum chemistry programs, HANDE performs calculations strictly in the symmetry sector requested by the user, which in our case is always the totally symmetric irreducible representation, unless otherwise specified. This brings into question the effect, in any, of including secondary references outside the symmetry sector under consideration. We first note that the secondary references are only used to define the shape of the spawning/death space, and are not required to exist in the `psip_list` or be occupied. It is conceivable that there are determinants/excitors in the correct symmetry sector that are included in the spawning space only by virtue of being connected (but of course not coupled by the Hamiltonian) to a wrong-symmetry secondary reference. To quantify the effect of these wrong-symmetry secondary references, we implemented a simple symmetry-screening switch in HANDE, which when turned on, only processes secondary references of the currently considered symmetry.

2.4.3 Cluster discarding

A persistent problem in CCMC calculations is the occurrence of large population blooms. This occurs when a large number of excips are created on a single, usually unimportant, excitor. These blooms have a destabilising effect on the calculation, and they create opposite spikes in shift and projected energy, causing the reblocking procedure to give unreliable energy estimates due to the non-symmetrical distribution of the samples around the true energy. In an analysis by [51], this is shown to be caused by the spawning probability scaling exponentially in the number of excitors that constitute the cluster. This means that, however infrequently, a large cluster can collapse onto an unimportant excitor, and spawn a large number of excips, and when these excips are created onto a likewise unimportant excitor, the calculation can be easily destabilised. The even-selection scheme (see Section 1.3.4) addresses exactly this problem, and practically eliminates blooms. However, in practice, the scheme requires a greatly increased number of samples taken per time step (see Equation (1.40)) that increases exponentially with the largest

allowed excitation level. Therefore, for the MR-CCMC algorithm applied to the carbon dimer, this renders the calculation too slow to be practical.

We have investigated a simple modification to the selection criterion, which discards clusters with spawning probabilities larger than a threshold, defined as $|A_c|/p_{\text{select}}$, with A_c being the amplitude of the cluster. This is a brute-force but guaranteed method of preventing blooms when the even selection algorithm is too expensive to be applied. We note that this has the same expression as the `cluster_multispawn_threshold`, which uses it to split up the processing a bloom, in hopes that the spawns can be more spread out. If both thresholds are used, then it is sensible to make the discard threshold larger than the multi-spawn threshold.

2.5 Results and discussions

2.5.1 BK-tree

For a C_2 system with a full $(8e, 8o)$ CAS as the model space without symmetry screening (4900 references that preserve the $M_s = 0$ symmetry). The BK-tree search is benchmarked against a naïve linear search, which loops over all secondary references and terminates search when one of the references is within P excitations away. The validity of the BK-tree search is separately established by performing a normal calculation with either search algorithms using the same random number generator seed, and asserting that the results are the same. The results are as follows: In the case of [Table 2.1](#), an apparent $8\times$ speedup is observed. Without performing a

	Overall timing / s	Time per spawning attempt / μs
BK tree	809.28	12.761
Linear	5995.16	94.533

Table 2.1 Timing comparison between the BK tree and naive search algorithms.

full profiling study, the actual reduction in time cost of the acceptance search is expected to be greater than $8\times$ as a complex series of operation is performed per spawning attempt on top of the acceptance search.

2.5.2 Symmetry screening

The results for the same system over the same range of bond lengths, but with symmetry screening turned on, are shown in [Figure 2.4](#). We can see that, although statistically significant, including the symmetry-forbidden secondary references only captures a negligible amount of

additional correlation energy. The full set of 4900 references are reduced to 635 symmetry-allowed references, while the compressed set of 722 references, whose results are not shown here, are reduced to 109 references. Both of these bring about a roughly 8-fold reduction of the model space size.

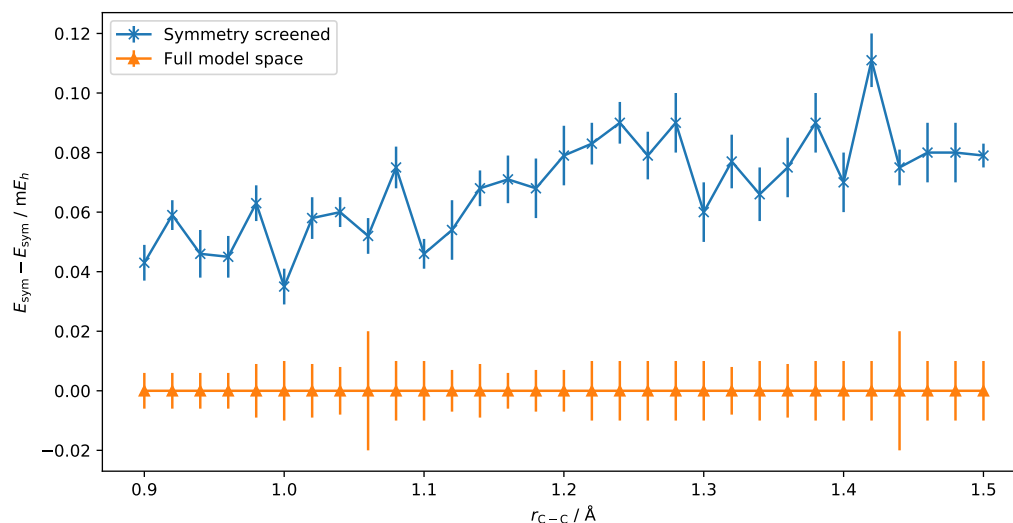


Fig. 2.4 The differences in energy between the full set of secondary references, E_{full} , and the set of symmetry-screened secondary references, E_{sym} , in units of mE_h . The very small error bars are thanks to the semi-stochastic algorithm (see [Chapter 5](#)).

2.5.3 Model space compression

For the $(8e, 8o)$ (the 2s and 2p space) CAS used for C_2 , the compression theorem ([Theorem A.0.4](#)) tells us the uniquely connected determinants are singles and doubles out of the lowest and highest two determinants in the CAS ($Q = 8/2 = 4$, $P = 2$ for CCSD), giving a total of 722 determinants in the compressed model space. We are able to obtain results for the $C_2/\text{cc-pVDZ}$ system at separations of 0.9 to 1.5 Å. The performance of the compression scheme is shown in [Figure 2.5](#). Here and elsewhere, unless otherwise noted, we have employed the default quasi-Newton acceleration (see [Section 1.3.4](#)). We can see that despite the almost 7-fold reduction in the model space (and consequently a similar reduction in computational cost), the errors are within chemical accuracy ($1.6 mE_h$).

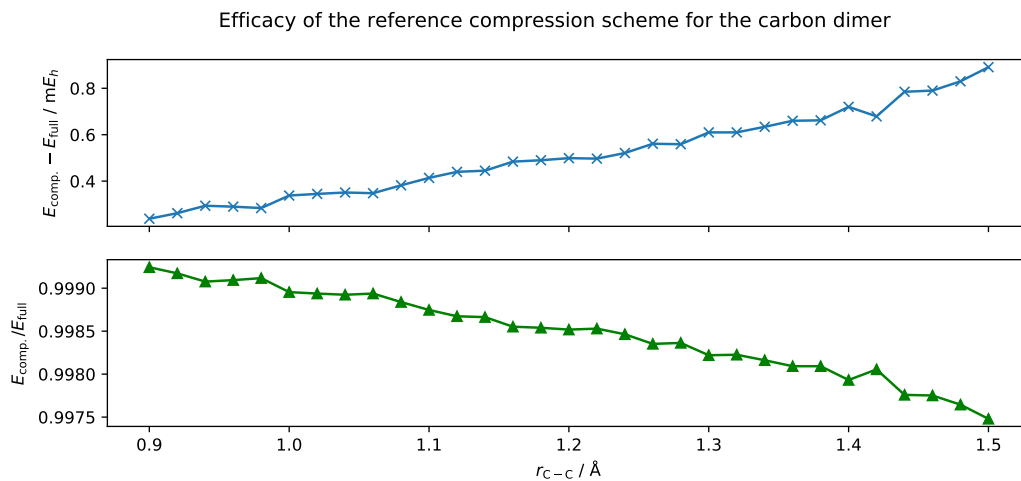


Fig. 2.5 The results from same system at 0.9 to 1.5 Å with the compressed set of 721 secondary references. We can observe that, despite a 7-fold reduction in the size of the model space, the reductions in the correlation energy captured are much smaller, and is an attractive trade-off. The error bars are plotted but are too small to be seen, due to the use of the semi-stochastic algorithm, outlined in [Chapter 5](#)

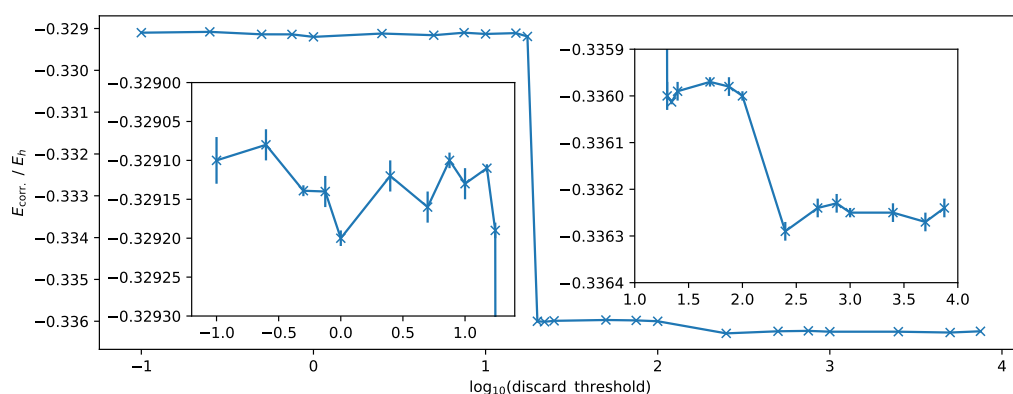


Fig. 2.6 The results from the $C_2/\text{cc-pVDZ}$ system at 1.2 Å separation, using the symmetry-screened uncompressed set of references, at a range of discarding thresholds.

2.5.4 Cluster discarding

The cluster discarding algorithm as described above seems to locate two distinct coupled cluster solutions in [Figure 2.6](#). At either solution, there does not seem to be clear, extrapolatable behaviour. Therefore we suggest that the cluster discarding algorithm be kept as a blunt tool of last resort, and only with careful benchmarking.

2.5.5 Binding curve of the carbon dimer

We studied the $^1\Sigma_g^+$ state of the carbon dimer in the cc-pVDZ basis. The carbon dimer is a challenging test case for electronic structure methods, and the challenge is two-fold: firstly, as mentioned in [Section 2.4.1](#), the $^1\Sigma_g^+$ state becomes very nearly degenerate with the exceptionally low-lying Δ_g state at stretched bond lengths, and both states descend to the A_g state in the commonly used D_{2h} point group symmetry, rendering it very challenging to distinguish both states without the use of the L_z symmetry, with one paper resorting to tracking individual CI coefficients [\[59\]](#); secondly, there is an abundance of avoided crossings, and specifically, the first excited $^1\Sigma_g^+$ state participates in an avoided crossing with the ground state at a bond length of around 1.6 Å [\[61\]](#), resulting in a change in the most weighted diabatic state (*i.e.*, determinant). The binding curve presented in [Figure 2.7](#) used the full (8e, 8o) CAS as the model space. Both the frozen-core (fc-MR-CCMC) and the full system were studied. For both, cluster discarding was disabled, but symmetry screening and semi-stochastic (see [Chapter 5](#)) were only enabled in the frozen-core calculations. The fully correlated MR-CCMC results are not parallel to the frozen core calculations, which is slightly surprising, since the core orbitals are fairly low-lying (with RHF eigenvalues of $\approx -11 E_h$ compared to the non-core orbitals being all above $\approx -1.5 E_h$), and are not expected to significantly affect the energies. However, we do note that the fully correlated calculations were run for fewer units of imaginary time, and were carried out without the semi-stochastic algorithm, which may impact the convergence of the calculations.

The non-parallelity errors (NPE), defined here as the difference between the maximal and minimal deviation from the FCIQMC energy, for all methods except DMRG (due to the mismatch of the bond lengths at which data are available), are shown in [Table 2.2](#). As already evident from the right inset of [Figure 2.7](#), MR-CCMC is virtually parallel to the FCIQMC curve, with the small gap being caused by the frozen-core approximation.

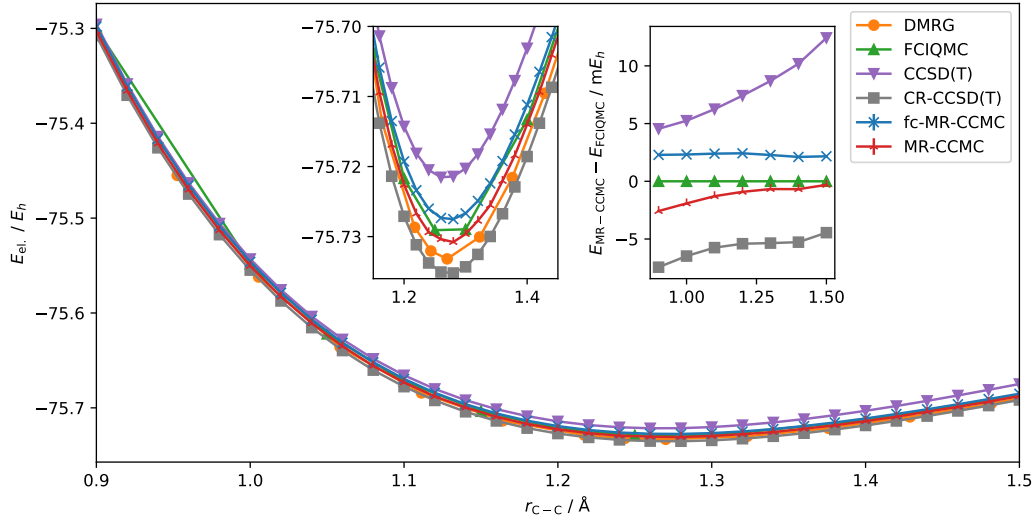


Fig. 2.7 The binding curve of the $^1\Sigma_g^+$ state of $C_2/cc\text{-pVDZ}$ in the range of 0.9-1.5 Å separation. The inset on the left shows the equilibrium region in more detail, and the inset on the right shows that the fc-MR-CCMC result and the FCIQMC result from [62] are fairly parallel in the region under study, unlike single-reference deterministic methods (note the units in mE_h). The fully correlated calculations show slightly larger variation with respect to FCIQMC. The DMRG results are from [59], and the CCSD(T) and CR-CCSD(T) (completely renormalised) are from our own implementations of the equations in [63], which were benchmarked against Psi4 [56] and GAMESS [64].

Method	NPE / mE_h
MR-CCMC	2.265
fc-MR-CCMC	0.316
CCSD(T)	7.874
CR-CCSD(T)	2.991

Table 2.2 The non-parallelity errors of the C_2 system under study for the three methods.

Chapter 3

FCIQMC-tailored multi-reference CCMC

We saw, in the previous chapter, that a compression scheme was able to systematically reduce the size of the reference space while retaining a large fraction of the correlation energy. Despite showing us that it is possible to strip a CAS reference space of certain ‘unimportant’ references without minimal loss in accuracy, the compression is one-off and not tunable in its final accuracy. A natural way to achieve a description of the CAS space with tunable accuracy is to leverage the pre-existing FCIQMC, or more accurately, CASCIQMC, algorithm, which naturally ranks the ‘importance’ of determinants by their CI expansion coefficients. We call this method tailored MR-CCMC (tMR-CCMC), and show with examples with various CAS sizes that this is a flexible algorithm that is able to capture varying degrees of static correlation, and show that qualitative descriptions can be obtained with much reduced cost compared to using the full CAS.

3.1 Motivation

In wavefunction-based electronic structure theory it is common to distinguish dynamic and non-dynamic correlation. This is because they are largely separate phenomena, and each require different methods to be treated adequately. Roughly speaking, static correlation occurs when two or more configurations have non-negligible weights in the exact wavefunction (see [12, Sec. 2.3]). Dynamic correlation, on the other hand, arises from the correlated motion of electrons by the mutual electrostatic repulsion of electrons (a classical effect); and the anti-symmetry of the overall wavefunction (a quantum mechanical effect).

The presence of both static and dynamic correlation requires the use of a multi-determinantal wavefunction, and indeed, in the limit of a full CI calculation, both effects will be captured in full, and no distinction between the two need to be made. However, we obtain a *single-reference* situation when only one determinant dominates the overall wavefunction; and a *multi-reference* situation otherwise. MBPT-based methods such as the MP_n family of methods, low-truncation

coupled cluster methods like CCSD and perturbative corrections thereof, like CCSD(T), usually suffice for capturing dynamic correlation. This is because when the perturbation in Equation (1.6) is small, the wavefunction would consist of a large number of very small contributions from highly excited determinants, whose weights are well approximated by products of weights on lower excited determinants. This can be seen in the accuracy of CCSD in single-reference systems, as higher-than-doubles amplitudes are approximated by products of singles and doubles amplitudes.

The idea of combining methods that separately excel at treating dynamic and static correlation has a long history. The most well known method in this class is probably the CASPT2 method [65], where a complete active space SCF (CASSCF) calculation that captures the static correlation is followed by a MBPT calculation to capture the remaining dynamic correlation. In the same vein, if instead of a CASSCF reference, a CASCI reference is used, a theory known as NEVPT (n -electron valence perturbation theory) results [66–68].

Another trend, which uses coupled cluster instead of MBPT as the dynamic correlation solver, has been that of ‘external correction’, with the idea that the coupled cluster amplitude equations at most contain up to four-body clusters, and if these cluster amplitudes were exact, we could obtain the FCI energy [69, 70]. Externally corrected coupled cluster methods commonly extract approximations to higher order cluster amplitudes (usually the three- and four-body ones) from an *external source*, such as a CASCI calculation, for example, [71] gets these amplitudes from an adaptive CI ([72]) calculation, and [73–75] extract amplitudes from FCIQMC and CCMC for the CC(P ; Q) methods [76]. Another sub-class of externally corrected coupled cluster methods is the *tailored* coupled cluster [77–79], where the external amplitudes remain frozen throughout the calculation, with the benefit that the computational scaling remains the same as the underlying single-reference calculation.

3.2 Towards a black-box generation of MR-CCMC model space

As an overview of the process, we run a CASCIQMC calculation in the CAS under study. After equilibration, a representation (which is finer-grained than instantaneous snapshots of the CASCIQMC wavefunction) of the wavefunction is extracted by time-averaging walker populations on the determinants, and using a cut-off scheme to only keep the important determinants. Here CASCIQMC is used as a solver for static correlation. These important determinants are then made into secondary references in a MR-CCMC calculation in the full space, which is used as a dynamic correlation solver. Hence, using mostly existing machinery in HANDE, we can

combine the separate treatments of static and dynamic correlation with black-box operation, with the only user input being the initial CAS and the accuracy of the CASCIQMC selection (which we will describe below).

3.2.1 FCIQMC as a static correlation solver

The use of the initiator approximation [42] (i-FCIQMC) is widely adopted. Its parameter, *initiator threshold*, n_a , leads naturally to a tunable granularity of the wavefunction, with $n_a = 0$ recovering FCIQMC. However, the convergence of n_a and the error to FCI energy (known as the *initiator error*) is complex and not well understood (see Table I of [42]). Better understood, however, is the convergence of the initiator error with total walker population N_w (see Figure 3 of [80] and Section VI of [39]). This then suggests an attractive way to control the error in the CASCI wavefunction, analogous to the σ parameter in adaptive CI (ACI) ([72]). However the exact form of the fitting requires more investigation.

A simplistic way to obtain the ‘important’ determinants is to rank the (absolute) populations of determinants, and use a cut-off scheme to only include the highly occupied determinants. It is important to not just take instantaneous snapshots of the wavefunction, as instantaneous occupation is too coarse-grained for all but the most highly occupied determinants (see for example Figure 2 of [80]). Instead, time-averaging these instantaneous snapshots is beneficial, especially when they are not strongly correlated. The correlation between two adjacent snapshots can be conveniently controlled by the `ncycles` parameter, which controls the number of MC cycles between report loops, as we only take snapshots at the end of report loops. Two cut-off schemes are implemented:

- Number of determinants: the user can specify the number, `ndets`, of determinants to produce at the end, and the number of report loops to average over.
- Percentage of total wavefunction: instead of capturing a fixed number of determinants, capture a fixed percentage of the wavefunction at each time step.

3.2.2 MR-CCMC as a dynamic correlation solver

After the list of secondary references is generated, a MR-CCMC calculation is started automatically using the list of secondary references. We then run an MR-CCSD calculation from the set of references/model space. This is because the FCIQMC run essentially brings all important high-order excitations into the cluster selection space, and as a result, the remaining dynamic correlation is expected to be well captured by products of singles and doubles amplitudes from the model space exciters.

3.3 Algorithm

We have implemented two truncation schemes, one based on the number of determinants ('fixed-number'), and the other based on the percentage weight of the wavefunction ('fixed-weight'). For both schemes, we output both the determinants and the time-averaged signed population on these determinants.

We separately implemented the ability to initialise a MR-CCMC calculation with the time-averaged populations. They are read in and scaled by the ratio between the time-averaged population and the reference population, so that they obey the normalisation scheme of the CCMC *ansatz*. The populations are also sign-corrected in the process of mapping CI coefficients to excitor amplitudes (see Equation (5.5)). This initialisation scheme can potentially ameliorate long equilibration times in systems with broken ergodicity ([81]), where two ergodic pockets are only weakly connected by a few Hamiltonian elements, such that if the calculation is only initialised in one pocket, a long time is needed on average to spawn to the other pocket, and have that spawn survive and maintain a stable population in that pocket. Initialising populations with the correct sign structure in a large CAS, which are likely to contain determinants that are weakly connected to the reference, is expected to speed up equilibration considerably. However we leave this for future work.

The set of references is also spin-augmented such that all determinants have their spin-flipped partner in a $M_s = 0$ calculation, to ensure as little spin contamination as possible occurs in the MR-CCMC calculation.

3.3.1 Fixed-number scheme

In this scheme, the user specifies the number of determinants to store, N_d . At the end of each report loop, N_d highest occupied determinants and their signed populations are collected and merged into the main array. The main array remains sorted by absolute population, but also stores the signed populations in order for the population merge to be performed correctly. The main array is made larger than N_d , so that statistical fluctuations near the tail-end of the array can be taken into account. At the end of the averaging process, the N_d highest occupied determinant are kept.

As (F)CIQMC is MPI-parallelised, we also parallelise this algorithm by simply gathering main arrays from each MPI process at the end by an `MPI_Gatherv` call, merging and sorting the resulting array, and keeping N_d most populated determinants.

3.3.2 Fixed-weight scheme

A more physically motivated scheme is the fixed-weight scheme, where a tunable parameter controls the amount of static correlation to capture. This is especially useful when a binding curve is under study - as the degree of multi-reference character varies across the binding curve, the same percentage of the static correlation can be captured by a variable number of model-space determinants.

The algorithm of the fixed-weight scheme is largely similar to the fixed-number scheme, but instead of collecting a fixed number of determinants, we collect the first N_d determinants such that the sum total of the normalised weights add up to η_w , which is a number between 0 and 1 provided by the user, *i.e.*, for the largest contiguous subset \mathcal{S} of all determinants on this process sorted high-to-low by absolute populations $|N_i|$ such that

$$\sum_{i \in \mathcal{S}} \left(\frac{N_i}{\mathcal{N}} \right)^2 \leq \eta_w, \quad (3.1)$$

where

$$\mathcal{N} = \left(\sum_{\text{all } i} N_i^2 \right)^{1/2} \quad (3.2)$$

is the normalisation constant.

We can make the truncation scheme as exact as possible by keeping a running list of all instantaneously occupied determinants and their cumulative populations, and only make the truncation at the end, this would have the memory complexity of $\mathcal{O}(N_{\text{tot}})$, and the time complexity of $\mathcal{O}(N_{\text{inst.}} \log N_{\text{tot.}})$, where $N_{\text{inst.}}$ is the number of instantaneously occupied states, and $N_{\text{tot.}}$ is the cumulative number of occupied states. The memory complexity is likely to be more severe. Alternatively, we can impose a once-in-never-out policy for the states, where we truncate at every time step, but once in the list, the states can never leave. This approximation will over-capture some of the least important determinants compared to the exact algorithm.

In parallelising the fixed-weight scheme, we note that [Equation \(3.1\)](#) requires the determinants to be ranked by absolute population and the knowledge of the normalisation constant over those determinants. This implies that it is impractical to perform these operations globally since that requires gathering all states onto at least one process, which can impose serious memory and speed constraints. We instead make the choice to only use the local wavefunctions for the truncation scheme, only synchronising at the end. If we used the exact algorithm, we will have to truncate the arrays locally before the parallel merge, as a single MPI process is unlikely to be able to hold all states that have ever existed on all processes; if we used the approximate algorithm, we can merge the arrays directly. The merged list will contain η_w of

the total time-averaged wavefunction, but only approximately. This is because we take the approximation that

$$\left[\sum_i^{n_{\text{procs}}} \left(\frac{\sum_{\mathbf{j} \in \mathcal{S}_i} N_{\mathbf{j}}}{\mathcal{N}_i} \right)^2 \right] / n_{\text{procs}} \approx \frac{\sum_{\mathbf{j} \in \mathcal{S}} N_{\mathbf{j}}^2}{\sum_i^{n_{\text{procs}}} \mathcal{N}_i^2}. \quad (3.3)$$

This is a warranted approximation, because if we consider a two-process merge with $a = \sum_{\mathbf{j} \in \mathcal{S}_0} N_{\mathbf{j}}^2$, and $b = \mathcal{N}_0^2$ for process 0, and c and d being the same quantity as a and b respectively, but for process 1, then the error in Equation (3.3) is

$$\frac{a}{b} + \frac{c}{d} - 2 \times \frac{a+c}{b+d} = \left(\frac{a}{b} - \frac{c}{d} \right) \times \frac{b-d}{b+d}. \quad (3.4)$$

Each term in the outer sum on the LHS of Equation (3.3) are all close to η_w by definition (*i.e.*, $a/b - c/d \ll 1$), and the determinant hashing procedure for load balancing in HANDE can reduce the magnitude of $(b-d)/(b+d)$ (though strictly load balancing aims to minimise $\sum N_{\mathbf{j}}$).

3.4 Results and discussion

3.4.1 Application to the carbon dimer

To demonstrate the correctness of the algorithm, and also the convergence property with respect to the number of (tailored) secondary references, we apply the tailoring algorithm to $\text{C}_2/\text{cc-pVDZ}$ at 1.2 Å separation. The $(8e, 8o)$ CAS as the tailoring space was used, with time-averaging over 200 CASCIQMC reports 50 MC iterations apart, starting 200 reports after the shift starts to vary. We can see in Figure 3.1 that the error to the full CAS energy monotonically decreases as more secondary references are captured, suggesting that we are indeed capturing a growing set of important determinants, with each successive set approximately a superset of the previous set.

3.4.2 Breaking the beryllium dimer

The beryllium dimer is known to be moderately multi-reference [82, 83]. This is commonly acknowledged to be due to the $2p$ orbitals being energetically close to the $2s$ orbitals, leading to significant occupation of the entire valence manifold. This leads to the $(4e, 8o)$ complete active space being the smallest CAS that is expected to provide an adequate description of the qualitative behaviour of the system. An extended $(8e, 10o)$ CAS is also studied, which includes additionally the core electrons, which are comparatively higher-lying than other first-row dimers, and hence are commonly included in correlation calculations. Being a relatively

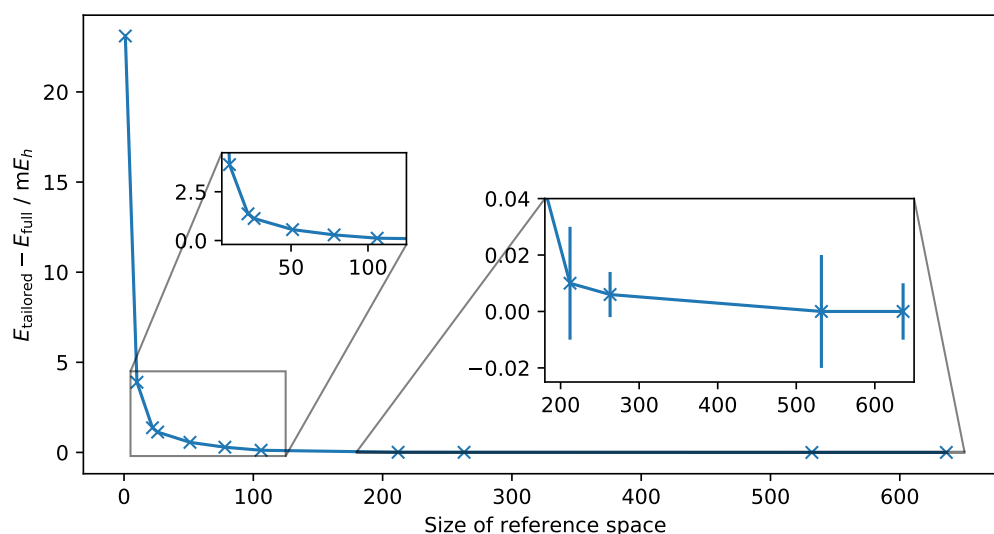


Fig. 3.1 Deviation of correlation energy from the result using the full CAS against the number of tailored references. Here the fixed-number tailoring scheme is applied to $\text{C}_2/\text{cc-pVDZ}$ at 1.2 Å separation, using the semi-stochastic algorithm (see [Chapter 5](#)) to achieve the small error bars. All of the reference spaces have been spin-augmented (see [Section 3.3](#)). The first point is a deterministic, single-reference CCSD correlation energy from Psi4, while the last point, with 635 secondary references, is calculated without the tailoring scheme, having read in the full list of $(8e, 8o)$ CAS determinants, with symmetry screening turned on.

small system, FCI benchmark results are available, with several at the complete basis set limit (CBS) [84, 85, 83].

Experimental potential energy curves extrapolated from spectroscopic studies can be found in [86], which puts the experimental well depth, D_e , at $934.8 \pm 0.3 \text{ cm}^{-1}$. To put that into perspective, the well depth is equal to $4.26 \text{ m}E_h$, which shows that any electronic structure method that attempts to study it need to be very accurate indeed. The experimental potential energy curve of Be_2 has a ‘shoulder’ feature, or change in gradient, at slightly above 3 \AA , this has been variously interpreted as a switching from multi- to single-reference regime ([83]); or from covalent interaction to van der Waals interaction ([87]). Therefore, to study the Be_2 molecule, the method needs to balance the need to treat both static correlation in the short range, and dynamic correlation in the long range, the latter of which also requires a large, and sufficiently diffuse basis set.

First, we carried out calculations in the $(4e, 8o)$ CAS with the cc-pVTZ basis, with L_z symmetry enabled, and then with a model space tailored by the $(8e, 10o)$ CAS, set to capture 98% of the tailoring wavefunction (‘tMR-CCMC(8,10)/0.98’), with the results shown in Figure 3.2. Unless otherwise specified, for the Be_2 calculations, the shift and the projected energy have been averaged (with appropriate error propagation), as the two can become symmetrically distributed in the intermediate range due to small reference populations. We note that the full $(8e, 10o)$ CAS would have been a more ideal set of calculations to compare to, but due to the very large reference space size we could not converge them in time. However qualitative behaviour are not expected to be drastically different for the two CASes as the core electron does not significantly participate in the bonding.

The cc-pVTZ basis set appears to over-bind the molecule by almost 600 cm^{-1} . The fact that small basis sets yielding over-estimations of the well depth has been pointed out elsewhere ([85]). However, we can still use this system to test the usefulness of the tailored MR-CCMC method: as can be seen in the inset of Figure 3.2, the tailored calculations, which all yielded about 20 secondary references, compared to 783 secondary references for the full $(4e, 8o)$ CAS, reach within $50 \text{ cm}^{-1} = 2.3 \text{ m}E_h$ of the full CAS results near the equilibrium, and rapidly converge to statistically identical energies at stretched bond lengths. Also of note here is the (approximate) size-consistency of both MR-CCMC and tMR-CCMC, as shown by their asymptotic convergence to the isolated atom limits (which were obtained by performing calculations on the Be atom with a $(2e, 4o)$ CAS, or tailored by a $(4e, 5o)$ CAS, respectively). Referring to the bottom inset in Figure 3.2, the tailoring method can be seen to work as intended, capturing roughly constant percentages of the correlation energy. The fact that the energy deviations are not constant, however, results from the fact that the correlation energies are very large at the head of the binding curve, as the HF potential is entirely repulsive [83]. Therefore, the correlation energies

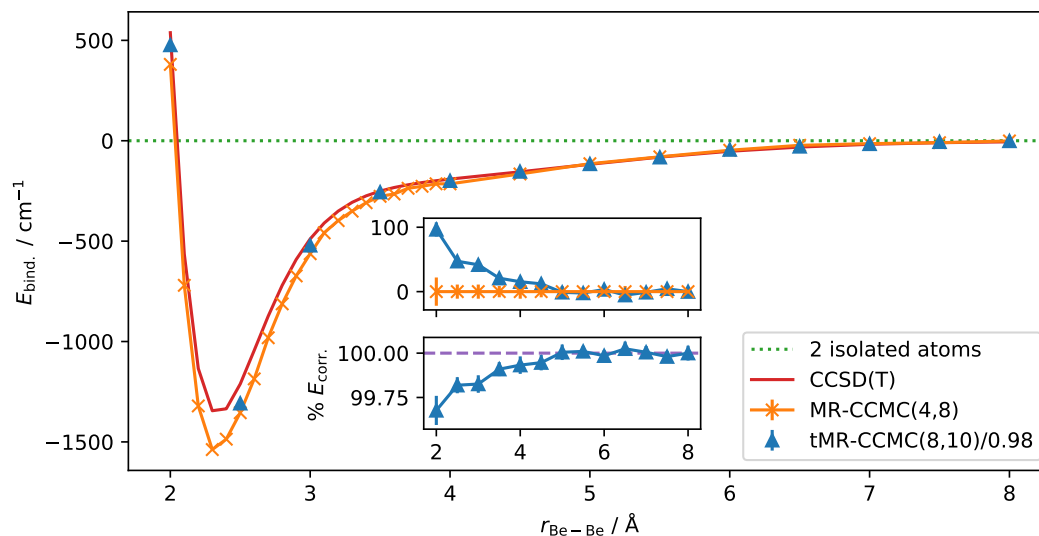


Fig. 3.2 The binding curve of $\text{Be}_2/\text{cc-pVTZ}$, with the model space being the $(4e, 8o)$ CAS, or after tailoring by the $(8e, 10o)$ CASCIQMC, compared to the single-reference CCSD(T) results obtained from Psi4. The top inset shows the deviation of the tailored results from the $(4e, 8o)$ CAS, and the bottom inset shows the ratio between the correlation energies of the tailored and CAS calculations, with the dotted purple line at 100% serving as a guide to the eye.

in the region of small separation are simply larger, and a constant percentage of them would result in larger errors in the electronic energies. This can be improved by using an energy criterion in the truncation scheme, like the degeneracy-corrected perturbation theory used in adaptive CI [72].

The results obtained from the larger cc-pVQZ basis set is shown in Figure 3.3. Due to time constraints, we attempted fewer points here, and as such only a qualitative behaviour can be understood. The cc-pVQZ basis set appears to more accurately describe the well, with the tMR-CCMC well depth being around 800 cm^{-1} . However, the tMR-CCMC method barely described the potential energy curve better than CCSD(T). This suggests that a larger percentage of the tailoring wavefunction need to be captured.

3.4.3 Automerisation of cyclobutadiene

The global ground state of cyclobutadiene (CBD), C_4H_4 , is in a D_{2h} rectangular geometry. The D_{4h} (square geometry) ground state is higher in energy due to a Jahn-Teller effect (which is the basis for its ‘anti-aromaticity’). The energy barrier between the D_{2h} and D_{4h} ground states is known as its *automerisation barrier*. This reaction is shown in Figure 3.4. This barrier has been a test bed of both electronic structure methods and experimental techniques, as

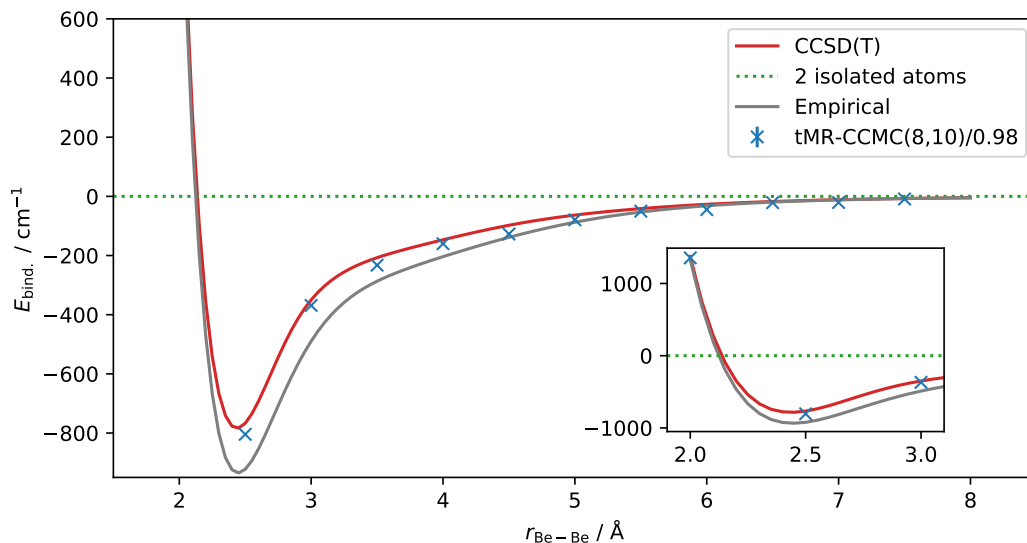


Fig. 3.3 The binding curve of $\text{Be}_2/\text{cc-pVQZ}$, with the model space being the $(4e, 8o)$ CAS, or after tailoring by the $(8e, 10o)$ CASCIQMC, compared to the single-reference CCSD(T) results obtained from Psi4. The empirical fit from [86] is also given.

the square intermediate is very multi-reference, and requires a CAS as large as $(12e, 12o)$ to describe accurately. Following [88, 79], we parametrise this automerisation pathway with a single interpolation parameter, λ , as follows:

$$x(\lambda) = (1 - \lambda)x + c, \quad x \in \{a, b\} \quad (3.5)$$

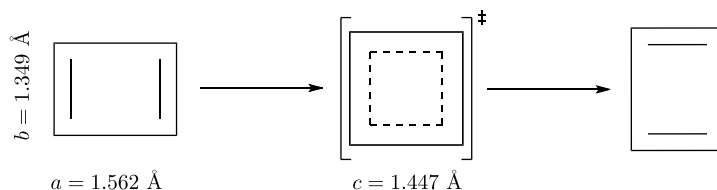


Fig. 3.4 The CBD automerisation reaction pathway. The bond lengths are obtained from optimised structures from [88].

The tMR-CCMC calculations employ the cc-pVDZ basis set, and a tailoring CAS of $(12e, 12o)$, set to capture 99.5% of the wavefunction over 200 reports that are 100 MC cycles apart from each other. The resulting model spaces are then run in a MR-CCMC calculation with the carbon $1s$ orbitals frozen, $\delta\tau = 0.005$, target population of 2×10^8 , and a discard threshold of 10. These tailoring calculations yielded around 10 references throughout the reaction coordinate, compared to the approximately $(^{12}C_6)^2/8 = 106722$ references (with the

factor of 8 to account for the A_g symmetry in D_{2h}). We note that the full CAS-MR-CCMC calculations would be prohibitively expensive. The discard threshold was enabled as otherwise the calculations would not converge within time constraints, and also since we are primarily interested in the barrier height, there is (as we will show in Figure 3.5) an error cancellation.

We show in Figure 3.5 the results obtained by tMR-CCMC compared to those of CCSD obtained from PySCF (with the carbon $1s$ core orbitals frozen as well). CCSD, being a single reference method, exhibits a sharp, unphysical cusp at the square geometry. This can be attributed to a failure to treat the avoided crossing at the square geometry properly, which at a minimum requires a $(2e, 2o)$ CAS of the HOMO and the LUMO; or alternatively, due to two RHF states crossing each other. As can be seen, our calculations yields a much improved potential energy curve for this reaction. In fact, our barrier height of 8.50 ± 0.13 kcal mol $^{-1}$ compares very favourably with what is commonly regarded as the best theoretical result of 8.8 kcal mol $^{-1}$ (from MR-AQCC, see [88]). This can also be seen in Figure 3.6, where we compare a range of theoretical estimates against our result.

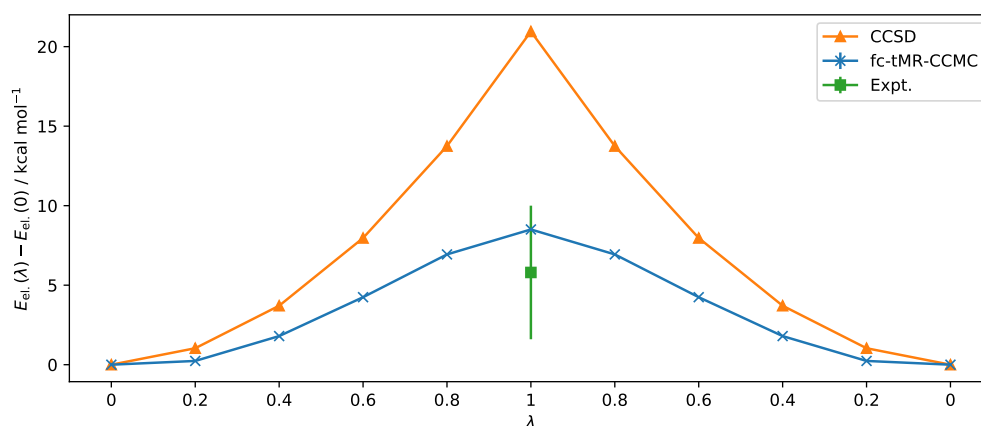


Fig. 3.5 The potential energy curves of the CBD automerisation reaction, as computed by a frozen-core CCSD and tMR-CCMC. The spread of the experimental values are indicated by the green error bar.

We note however that the use of the discard threshold resulted in a reduction of correlation energy being captured, such that the raw energy curves would have the CCSD curves below our calculations, but once shifted to the starting point, the two curves show qualitatively similar behaviour as those in [79]. A set of calculations without discard thresholds, which is expected to be fairly parallel to the current set, will be available in a future publication.

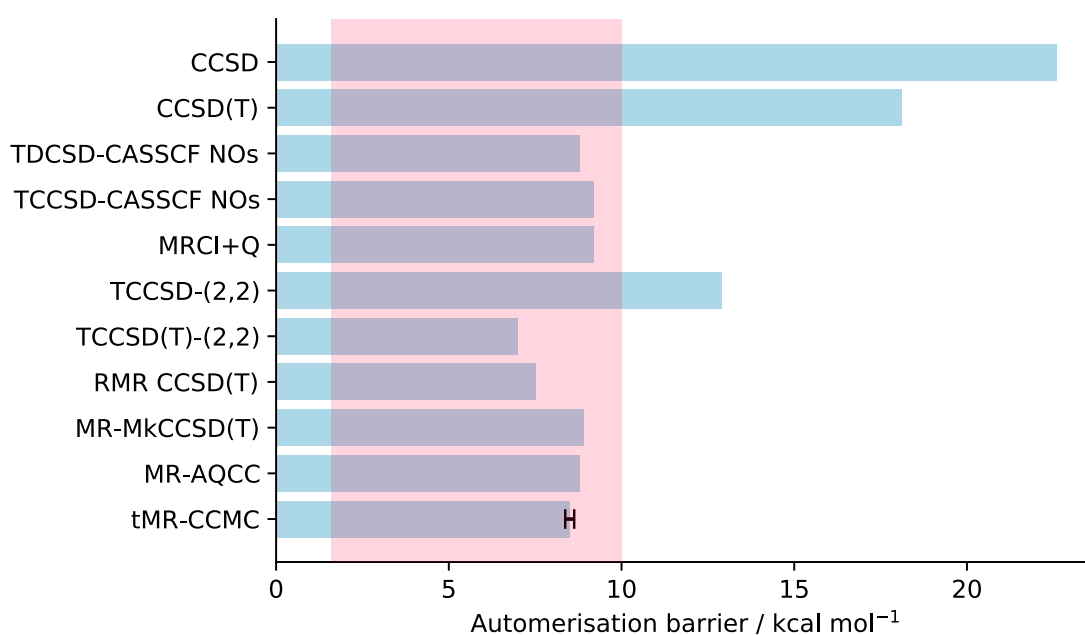


Fig. 3.6 Comparisons of various theoretical estimates for the barrier height. The experimental range is from [89, 90]. CCSD and CCSD(T) results are from PySCF, the TD/CCSD using CASSCF natural orbitals (NOs) are from [79], the MRCI+Q results are performed in Molpro [91] by [79], the TCCSD/(T)-(2,2) results are from [92], the RMR CCSD(T) is from [93], the MR-MkCCSD(T) is from [94], and the MR-AQCC result is from [88].

Chapter 4

Accelerating convergence with non-linear projectors

As reviewed in [Section 1.3.4](#), there have been various attempts at improving the linear Taylor projector that FCIQMC and CCMC employ. In this chapter, we start by reviewing the general theory of ground-state projectors, and then introduce the wall-Chebyshev projector. We will show that the wall-Chebyshev projector brings about higher efficiency than the default linear projector, to no detriment of the statistical convergence of the underlying methods.

4.1 Theory of projectors

4.1.1 The ground state projector

Following [\[95\]](#), the ground state projector, $\hat{P}_{\text{GS}}(\hat{\mathbf{H}})$, brings an arbitrary trial wavefunction $|\Phi\rangle$ to the ground state, $|\Psi_0\rangle$, of the target Hamiltonian $\hat{\mathbf{H}}$:

$$|\Psi_0\rangle = N_P \hat{P}_0(\hat{\mathbf{H}}) |\Phi\rangle, \quad (4.1)$$

where the trial wavefunction should be normalisable and has nonzero overlap with the ground state, *i.e.*, $\langle\Phi|\Psi_0\rangle \neq 0$, and N_P enforces the normalisation of $|\Psi_0\rangle$.

We restrict ourselves to ground state projectors that can be written in an iterative form:

$$\hat{P}_0 = \lim_{n \rightarrow \infty} g^n(\hat{\mathbf{H}}), \quad (4.2)$$

where g is termed the *generator* in [\[95\]](#), but in keeping with common QMC terminology, we refer to g as the underlying projector of the ground state projector \hat{P}_0 , or simply the projector.

As an example, we are reminded of the imaginary time propagator, g^{exp} , given by

$$g^{\text{exp}}(\hat{\mathbf{H}}) = e^{-\delta\tau(\hat{\mathbf{H}}-S)}. \quad (4.3)$$

When taken to infinite imaginary time, it yields the ground state projector for the Hamiltonian:

$$\lim_{n \rightarrow \infty} [e^{-\delta\tau(\hat{\mathbf{H}}-S)}]^n = \hat{P}_0(\hat{\mathbf{H}}). \quad (4.4)$$

Evidently, the projector has to discriminate between eigenstates, which means that it scales each eigenstate differently:

$$g(\hat{\mathbf{H}})|\Phi\rangle \equiv |\Psi^{(1)}\rangle = \sum_i g(\hat{\mathbf{H}})c_i|\psi_i\rangle = \sum_i g(E_i)c_i|\psi_i\rangle, \quad (4.5)$$

which reveals the action of the ground state projector:

$$\hat{P}_0(\hat{\mathbf{H}})|\Phi\rangle = \lim_{n \rightarrow \infty} |\Psi^{(n)}\rangle = \lim_{n \rightarrow \infty} \sum_i g(E_i)^n c_i |\psi_i\rangle, \quad (4.6)$$

where $\{\psi_i\}$ is the eigenbasis of $\hat{\mathbf{H}}$, and $g(E_i)$ are the factors by which eigenfunctions are scaled, and $|\Psi^{(i)}\rangle$ is the i -th intermediate wavefunction after i applications of the projector.

To achieve ground state projection, we must require that $|g(E_0)| > |g(E_i)|$ for all $i \neq 0$, which means all excited states decay to zero in the $n \rightarrow \infty$ limit. Clearly, if we knew exactly the ground state energy, E_0 , we can simply set $g(E_0) = 1$ (without loss of generality), and $g(E_i) = 0$, $\forall i \neq 0$, but that would be equivalent to having solved the problem beforehand. To make progress, we can additionally insist that our projector fulfil the ‘variationality’ condition: that if we have an upper bound for E_0 , $\tilde{E}_0 \geq E_0$, that is in the neighbourhood of E_0 , then $g(E_0)$ needs to be always greater than $g(\tilde{E}_0)$. We summarise these conditions below:

$$|g(E_0)| > |g(E_i)|, \forall E_i \in (E_0, E_{N-1}] \text{ (ground state)} \quad (4.7a)$$

$$|g(x)| > |g(y)|, \text{ if } x < y \in [E_0, \tilde{E}_0] \text{ (variationality)} \quad (4.7b)$$

The exponential projector trivially fulfils these conditions, and so does the first-order Taylor expansion of g^{exp} , g^{lin} :

$$g^{\text{lin}}(x) = 1 - \delta\tau(x - S), \quad (4.8)$$

which is none other than the linear projector used in the basic FCIQMC and CCMC algorithms.

4.2 The wall-Chebyshev projector

One may reasonably ask the question: why not just go to higher orders of the Taylor expansion? Unfortunately, as we show in [Appendix B.2](#), that there is no benefit in doing so whatsoever. So one has to look elsewhere. A Chebyshev expansion of the wall function was first proposed in [\[95\]](#), where the wall function

$$\text{wall}(x) = \begin{cases} \infty, & x \leq 0 \\ 1, & x = 0 \\ 0, & x > 0 \end{cases}, \quad (4.9)$$

can be seen as the infinite time limit of the exponential projector:

$$\lim_{\tau \rightarrow \infty} e^{-\tau(x-S)} = \text{wall}(x - S), \quad (4.10)$$

which is the underlying functional form of the ground state projector $\hat{P}_{\text{GS}}(\hat{\mathbf{H}})$.

While a Taylor series expansion does not exist for the discontinuous wall function, a Chebyshev expansion, like a Fourier expansion, is trivial. The Chebyshev polynomials of the first kind, defined as $T_n(\cos(\theta)) = \cos(n\theta)$, form an orthogonal basis for functions defined over $x \in [-1, 1]$:

$$\int_{-1}^1 T_m(x) T_n(x) (1-x^2)^{-1/2} dx = \delta_{mn} \pi / (2 - \delta_{m0}). \quad (4.11)$$

To facilitate the following discussion, we define the *spectral range*, R , of a Hamiltonian as $R = E_{N-1} - E_0$. We then rescale x so that $x \in [-1, 1]$, where $x = 2(E - E_0)/R - 1$. We show in [Appendix B.3](#) that the m -th order Chebyshev expansion of the wall function is

$$g_m^{\text{wall-Ch}}(x) = \frac{1}{1 + 2m} \sum_{k=0}^m (2 - \delta_{k0}) T_k(-x). \quad (4.12)$$

We plot several orders of Chebyshev expansion in [Figure 4.1](#), where we can also observe the monotonic divergence to $+\infty$ for $x < E_0$. The other tail also diverges to $\pm\infty$ depending on the parity of the order. We can see here another reason why a Chebyshev expansion is used: it provides the best approximations to functions in the maximum norm sense ([\[96\]](#)), as can be seen by the large gradient near the lower bound of the higher order expansions.

Yet another reason for using the Chebyshev polynomials is that, in this instance, the nodes of Equation (4.12) are analytically known as (which we derive in Appendix B.3)

$$a_\nu = E_0 + \frac{R}{2} \left(1 - \cos \frac{\nu\pi}{m + 1/2} \right). \quad (4.13)$$

Which allows us to decompose the m -th order projector into a product of m linear projectors, each with their own weight that ensures $g_m^{\text{wall-Ch}}(E_0) = 1$:

$$g_m^{\text{wall-Ch}}(x) = \prod_{\nu=1}^m \frac{x - a_\nu}{E_0 - a_\nu}. \quad (4.14)$$

A decomposition for a fifth order Chebyshev expansion of the wall function can be seen in Figure 4.2.

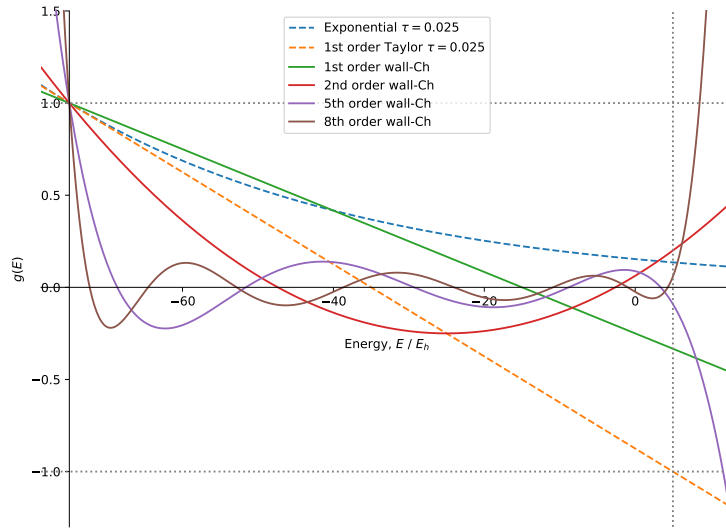


Fig. 4.1 The Chebyshev expansions of the wall function in an arbitrary range of $[-75, 5]$, compared to the linear projector with the maximal time step of $\delta\tau = 0.025$, and its corresponding exponential projector.

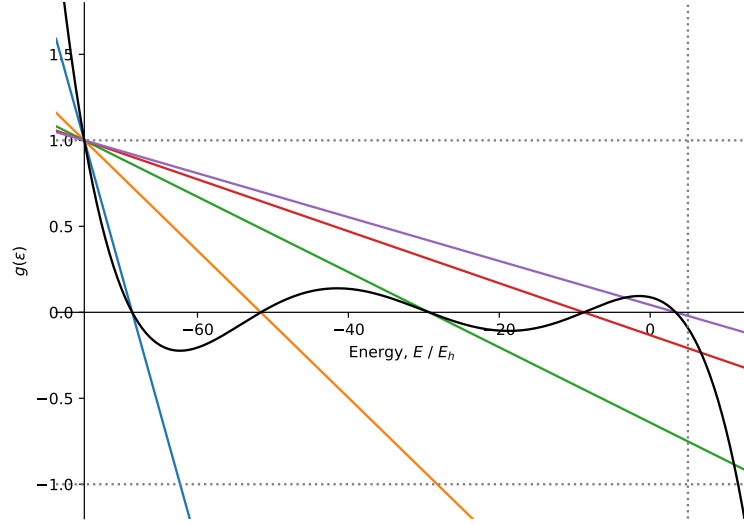


Fig. 4.2 The fifth order Chebyshev expansion of the wall function, shown here to decompose into a product of 5 linear projectors, each with their own effective time steps.

4.3 Application to FCIQMC and CCMC

In FCIQMC and CCMC, the lowest eigenvalue estimate is the shift, S , and the upper spectral bound can be a constant, estimated from the Gershgorin circle theorem ([97]) as

$$\tilde{E}_{N-1} = H_{N-1,N-1} + \sum_{\mathbf{j} \in \{S, \mathcal{D}\}}' H_{N-1,\mathbf{j}}, \quad (4.15)$$

where the sum is over all determinants connected to the highest determinant (singles and doubles), and the “'” on the sum restricts it to $\mathbf{j} \neq |D_{N-1}\rangle$. Due to the approximate nature of the estimation, the upper spectral range estimate is scaled up by 10% by default, but users are also given the options to override, or shift and scale the Gershgorin estimate as they see fit.

The action of the wall-Chebyshev projector on $|\Psi^{(n,0)}\rangle = [g^{\text{wallCh}}(\hat{\mathbf{H}})]^n |\Phi\rangle$ is

$$g^{\text{wallCh}}(\hat{\mathbf{H}}) |\Psi^{(n,0)}\rangle = |\Psi^{(n+1,0)}\rangle, \quad (4.16)$$

which gives the wavefunctions after integer number of applications of the projector. We can additionally define the ‘intermediate’ wavefunctions as

$$|\Psi^{(n,\mu)}\rangle = \left[\prod_{\nu=0}^{\mu} \frac{\hat{\mathbf{H}} - a_{\nu}}{S - a_{\nu}} \right] [g^{\text{wallCh}}(\hat{\mathbf{H}})]^n |\Phi\rangle. \quad (4.17)$$

We are now ready to derive the update equations for FCIQMC and CCMC. We start with the slightly more involved derivation for CCMC first. Projecting these intermediate wavefunctions with excitors, we have

$$\langle D_{\mathbf{m}} | \Psi^{(n,\nu+1)} \rangle = \frac{1}{S - a_{\nu}} \langle D_{\mathbf{m}} | \hat{\mathbf{H}} - a_{\nu} | \Psi^{(n,\nu)} \rangle \quad (4.18)$$

It’s important now to distinguish between $\tilde{t}_{\mathbf{m}}$ and $t_{\mathbf{m}}$, with the former including unconnected (‘composite’) contributions:

$$\begin{aligned} \tilde{t}_{\mathbf{m}} &= -\frac{1}{a_{\nu} - S} \left[\sum_{\mathbf{n} \neq \mathbf{m}} H_{\mathbf{mn}} \tilde{t}_{\mathbf{n}} + (H_{\mathbf{mm}} - a_{\nu}) \tilde{t}_{\mathbf{m}} \right] \\ \tilde{t}_{\mathbf{m}} - t_{\mathbf{m}} + t_{\mathbf{m}} &= -\frac{1}{a_{\nu} - S} \left[\sum_{\mathbf{n} \neq \mathbf{m}} H_{\mathbf{mn}} \tilde{t}_{\mathbf{n}} + (H_{\mathbf{mm}} - a_{\nu}) \tilde{t}_{\mathbf{m}} \right] \\ t_{\mathbf{m}} &= t_{\mathbf{m}} - \frac{1}{a_{\nu} - S} \left[\sum_{\mathbf{n} \neq \mathbf{m}} H_{\mathbf{mn}} \tilde{t}_{\mathbf{n}} + (H_{\mathbf{mm}} - S) \tilde{t}_{\mathbf{m}} \right] \end{aligned} \quad (4.19)$$

Comparing with the original update equations

$$t_{\mathbf{m}} = t_{\mathbf{m}} - \delta\tau \left[\sum_{\mathbf{n} \neq \mathbf{m}} H_{\mathbf{mn}} \tilde{t}_{\mathbf{n}} + (H_{\mathbf{mm}} - S) \tilde{t}_{\mathbf{m}} \right], \quad (4.20)$$

we reach the conclusion that the only modifications needed are

1. Set $\delta\tau = 1$
2. Loop over the linear components, scale Hamiltonian elements in spawning and death by $1/(a_{\nu} - S)$ (‘Chebyshev weights’)

The same analysis can be performed on FCIQMC, which is without the complication of composite amplitudes, and obtain a similar set of update equations:

$$c_i = c_i - \frac{1}{a_\nu - S} \left[\sum_{j \neq i} H_{ij} c_j + (H_{ii} - S) c_i \right]. \quad (4.21)$$

In terms of code implementation, the two sets of update equations are identical, and can share the same code.

Analysis ([95]) of the asymptotic rate of convergence (see [Appendix B.1](#)) shows that the theoretical speedup of an order m wall-Chebyshev projector relative to the linear projector with largest allowed $\delta\tau$ is $(m + 1)/3$. But due to blooms the largest $\delta\tau$ is never reached, so real speedups are expected to be larger.

4.4 Restoring the shift update procedure

Due to the time step $\delta\tau$ being set to unity, as can be seen in [Equation \(1.29\)](#), the shift update procedure is expected to become rather unresponsive to the changes in particle population. As a consequence, there can be vastly uncontained spawning unchecked by the lower-than-expected deaths result in unmanageable population growths. To remedy this, initially, a scaled update procedure was experimented with:

$$S^{(i+1)} = S^{(i)} - \zeta \sum_{\nu=1}^{\mu} [a_\nu^{(i)} - S^{(i)}] \ln \frac{N_w^{(i,\nu)}}{N_w^{(i,\nu-1)}}, \quad (4.22)$$

which seemed attractive as it reduces to [Equation \(1.29\)](#) in the first-order case where the sum only contains one term or if all Chebyshev weights are the same. However, this was not successful in reigning in the population growth. We believe this is because the intermediate wavefunctions in [Equation \(4.17\)](#) are ill-behaved due to being generated by an effective time step potentially larger than τ_{\max} , hence the population information from these intermediate wavefunctions should not be used. Put in other words, a series of population changes that start and end at $N^{(n)}$ and $N^{(n+1)}$ respectively can produce very different values of shift update in [Equation \(4.22\)](#), and the shift update produced is very sensitive to the unreliable intermediate values.

Another procedure that was more successful was simply increasing the shift damping parameter ζ from the default 0.05, which helps make the shift more responsive to the changes in population, which in turn helps stabilise the population. We also use the improved shift update

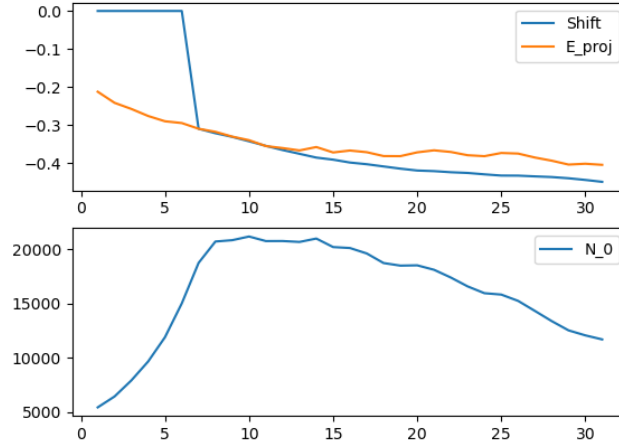


Fig. 4.3 $C_2/cc\text{-pVDZ}$ at 2.0 \AA separation, with a fifth-order wall-Chebyshev projector. With default settings, the Chebyshev propagator can cause the shift to become unresponsive to the large changes in total population, resulting in uncontained population growth and slow convergence.

procedure outlined in [98], where an additional term is added to the shift-update procedure:

$$S^{(n+A)} \leftarrow -\frac{\xi}{A\delta\tau} \ln \left(\frac{N_w^{(n+A)}}{N_t} \right), \quad (4.23)$$

where ξ is the ‘forcing strength’, and N_t is the target population. This has the effect of additionally stabilising the population by ‘pinning’ the population to the target population. A further proposal from the same paper, arising from an argument from a scalar model of population dynamics, is for critical damping to be achieved by setting $\xi = \zeta^2/4$. This is also found to be helpful. Altogether, these modifications result in greatly improved population control and we were able to obtain dynamics that can be automatically reblocked, as shown in Figure 4.4, for example.

In practice, we have also found that with increasing order of Chebyshev projector, a larger target population is usually needed, otherwise the calculation may exhibit a sign problem-like divergence, as expected from a smaller-than-required target population. This can be attributed to the larger effective time steps that the higher order projectors use, this is documented elsewhere, for example, see [99, Fig. 2].

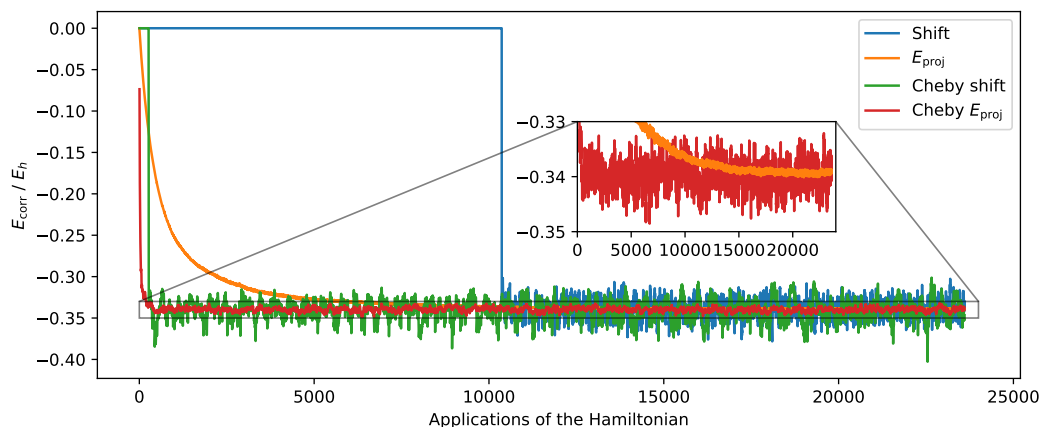


Fig. 4.4 A fifth order Chebyshev projector applied to $C_2/cc\text{-pVDZ}$ at 1.2 \AA separation, with a full $(8e, 8o)$ CAS as the model space, with a target population of 2×10^6 and a shift damping parameter of 0.5, as compared to a linear projector with $\delta\tau = 0.001$, a target population of 1×10^6 , and a shift damping parameter of 0.05. Both calculations are carried out with a two-stage harmonic forcing shift update scheme. The inset shows that the projected energy only barely stabilises around the true value at the end of the calculation using the linear projector. This means that the reblocking algorithm will disregard essentially all of the iterations shown here, due to the shift and the projected energy not agreeing.

4.5 Results

Figure 4.4 shows an example of the power of the Chebyshev propagation. The shoulder height is reached after around 50 iterations, and the calculation is equilibrated essentially instantaneously, which means all that is left to do is collecting statistics. Without the Chebyshev projector, the same calculation would take around 24 hours with 12 physical cores to give the same statistical error bar, the calculation in the figure reached the statistical error bar after being run for only 2 hours on 6 physical cores.

Part of the benefit of our Chebyshev propagator algorithm is the automatic determination of the effective time steps, or ‘Chebyshev weights’, *via* the Gershgorin circle theorem, which in the first-order expansion limit reduces to an automatic way of choosing a good time step, instead of using trial and error. In our experience, users may simply choose to use intuition that could be wrong, or a safe and low $\delta\tau$, both resulting in inefficiencies. The following example shows a smaller, modestly multi-reference system of Be_2 cast in the $cc\text{-pVQZ}$ basis set. Referring to Figure 4.5, compared with the linear projector with a guessed $\delta\tau = 0.002$, the second-order Chebyshev expansion, there is clearly a speed-up in convergence in the Chebyshev calculation. In fact, the Chebyshev calculation took 66 applications of the Hamiltonian to reach the target

population of 3×10^6 , whereas the linear projector took 3034 applications to reach the same target population.

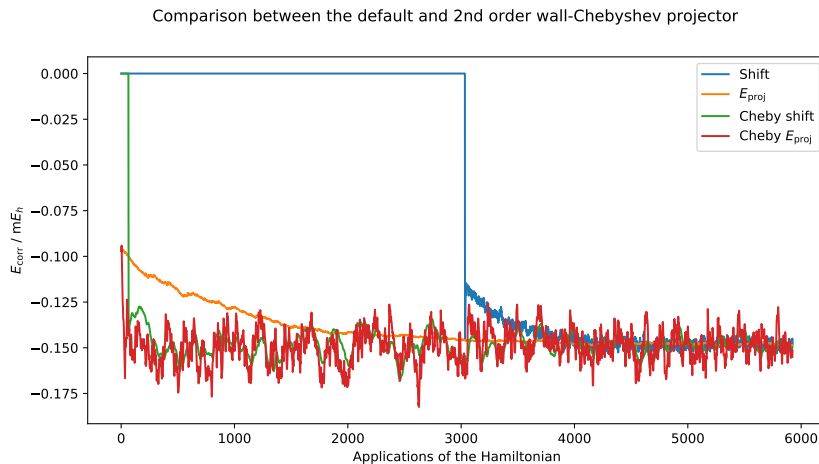


Fig. 4.5 The second order projector and the default linear projector at $\delta\tau = 0.002$ applied to the $\text{Be}_2/\text{cc-pVQZ}$ at 2.5 \AA separation, with a symmetry-screened $(4e, 8o)$ (full $2s, 2p$ valence) CAS as the model space. Both calculations have a target population of 3×10^6 .

However, the second-order Chebyshev projector is expected to be as efficient as the linear projector with the maximum allowed time step (see Section 4.3). To provide a fairer comparison, we present in Figure 4.6 comparisons of the first, second and fourth order Chebyshev projector applied to the $\text{Be}_2/\text{cc-pVQZ}$ at 2.5 \AA system. The first order Chebyshev projector is equivalent to a linear projector with $\delta\tau = 3/(E_{N-1} - E_0)$, which is $2/3$ of $\delta\tau_{\text{max}}$, but this maximal time step is commonly found to give rise to destabilising population blooms, so the first order Chebyshev projector gives an estimate for a practical time step to use. Here we can most clearly see the reduction in time needed to reach the shoulder height. It is worth bearing in mind that the three calculations require different target populations to stabilise, with the first and second order projectors having target populations of 3×10^6 , and the fourth order projector having a target population of 5×10^6 , which slightly increases the number of iterations required to reach the target population.

An even clearer example is shown in Figure 4.7, where we simulate the effect of the first order Chebyshev projector by compressing the imaginary time evolution of the linear projector with $\delta\tau = 0.001$ in Figure 4.4 accordingly.

In summary, our implementation of the wall-Chebyshev projector is generally applicable to a range of systems, in FCIQMC and CCMC. It brings about faster statistical convergence at a reduced computational cost, and at a minimum, helps automate the usually tedious trial-and-error process of obtaining an optimal time step.

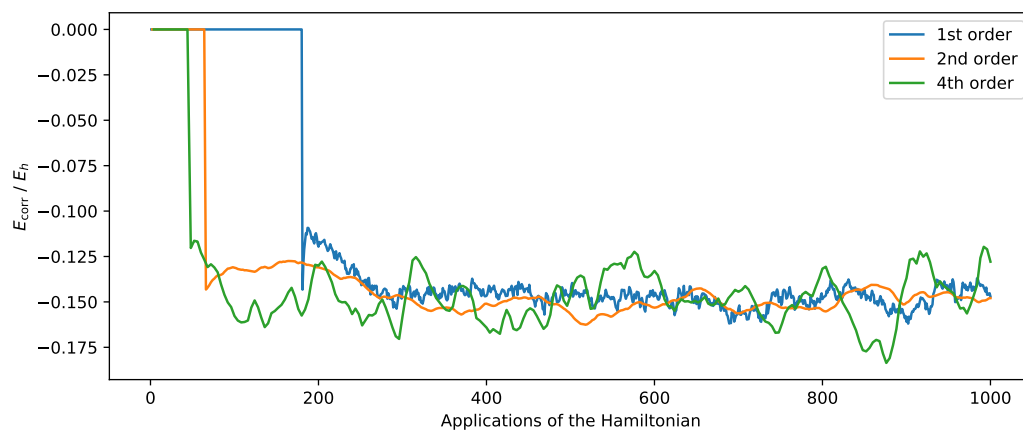


Fig. 4.6 The $\text{Be}_2/\text{cc-pVQZ}$ at 2.5 \AA separation with the $(4e, 8o)$ CAS model space run with the first, second and fourth order Chebyshev projectors. Only the time evolution of the shift parameters is shown for clarity.

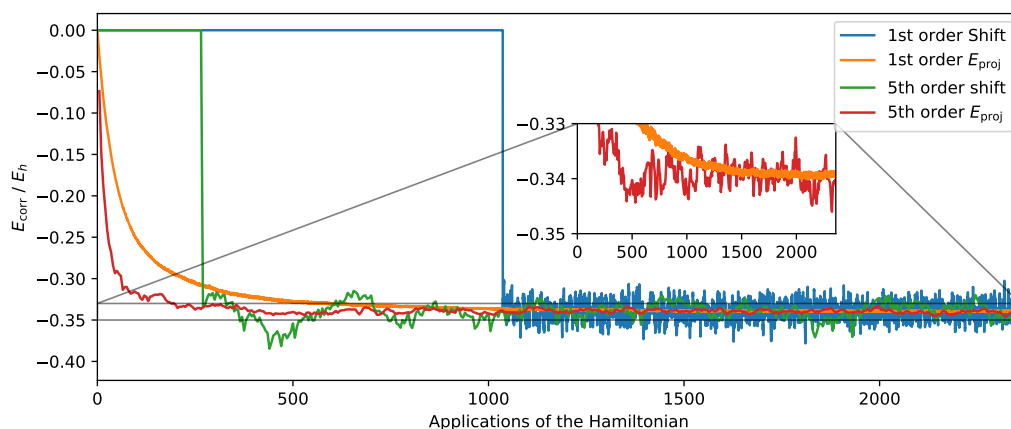


Fig. 4.7 $\text{C}_2/\text{cc-pVDZ}$ at 1.2 \AA separation, with a full $(8e, 8o)$ CAS model space, run with the first (simulated) and fifth order Chebyshev projectors.

Chapter 5

Semi-stochastic CCMC

Keeping our focus on the projector, but returning for now to the linear projector, in this chapter we propose the semi-stochastic CCMC algorithm. Viewing the CCMC algorithm as a series of massive stochastic matrix-vector multiplications, we perform the dense part of the matrix-vector multiplication deterministically to reduce the final stochastic noise. We show with examples of multi-reference systems that this can indeed be achieved with sometimes dramatic reduction in projection noise, which leads to faster statistical convergence of the algorithm.

5.1 Theory

5.1.1 Semi-stochastic FCIQMC

First introduced in [100], and further expounded in [101], the semi-stochastic formulation of the FCIQMC algorithm has been in routine use in production-level calculations. We start by noting that the FCIQMC algorithm is essentially a stochastic power iteration algorithm: the action of the linear projector $g^{\text{lin}} \equiv \hat{P} = \mathbf{I} - \delta\tau(\hat{\mathbf{H}} - S\mathbf{I})$ can be written as

$$\mathbf{c}_0 = \mathbf{c}^{(\infty)} = \lim_{n \rightarrow \infty} [\mathbf{I} - \delta\tau(\hat{\mathbf{H}} - S\mathbf{I})]^n \mathbf{c}^{(0)}, \quad (5.1)$$

where \mathbf{c}_0 is the ground state wave vector, $\mathbf{c}^{(n)}$ is the approximate ground state vector at iteration n , with $c_i^{(n)}$ being the population on determinant $|\mathbf{i}\rangle$ at iteration n . By partitioning the Hilbert space into a deterministic space, \mathcal{D} , and the complementary stochastic space \mathcal{S} , the overall projector

can be likewise partitioned into a deterministic projector, $\hat{P}^{\mathcal{D}}$, and a stochastic projector, $\hat{P}^{\mathcal{S}}$:

$$\hat{P}^{\mathcal{D}} = \sum_{\mathbf{i}, \mathbf{j} \in \mathcal{D}} P_{\mathbf{ij}} |\mathbf{i}\rangle \langle \mathbf{j}| \quad (5.2a)$$

$$\hat{P}^{\mathcal{S}} = \left(\sum_{\mathbf{i}, \mathbf{j} \in \mathcal{S}} + \sum_{\substack{\mathbf{i} \in \mathcal{D} \\ \mathbf{j} \in \mathcal{S}}} + \sum_{\substack{\mathbf{i} \in \mathcal{S} \\ \mathbf{j} \in \mathcal{D}}} \right) P_{\mathbf{ij}} |\mathbf{i}\rangle \langle \mathbf{j}|. \quad (5.2b)$$

The action of the overall projector on the vector of determinant populations can be likewise decomposed as follows (the iteration superscript is omitted for clarity):

$$\begin{aligned} \hat{P}\mathbf{c} &= (\hat{P}^{\mathcal{D}} + \hat{P}^{\mathcal{S}})(\mathbf{c}^{\mathcal{D}} + \mathbf{c}^{\mathcal{S}}) \\ &= \hat{P}^{\mathcal{D}}\mathbf{c}^{\mathcal{D}} + \hat{P}^{\mathcal{S}}\mathbf{c}^{\mathcal{S}} + \hat{P}^{\mathcal{S}}\mathbf{c}^{\mathcal{D}}, \end{aligned} \quad (5.3)$$

where the other ‘mixed’ term, $\hat{P}^{\mathcal{D}}\mathbf{c}^{\mathcal{S}}$, vanishes as $\hat{P}^{\mathcal{D}}$ does not act on stochastic basis states. Denoting the diagonal part of a Hamiltonian $\hat{\mathbf{H}}_{\text{d}}$, and the off-diagonal part $\hat{\mathbf{H}}_{\text{od}}$, then the semi-stochastic FCIQMC (ss-FCIQMC) algorithm can be summarised as follows:

- **Stochastic spawning** ($-\delta\tau\hat{\mathbf{H}}_{\text{od}}^{\mathcal{S}}(\mathbf{c}^{\mathcal{D}} + \mathbf{c}^{\mathcal{S}})$): Iterate over all occupied states, and for each \mathbf{i} attempt spawning onto a state \mathbf{j} with some probability $p_{\mathbf{ij}}$. If both $\mathbf{i}, \mathbf{j} \in \mathcal{D}$, abandon attempt as this will be performed in the deterministic projection; else a new walker on \mathbf{j} is created with signed weight $-\delta\tau H_{\mathbf{ji}}c_{\mathbf{i}}/p_{\mathbf{ij}}$
- **Stochastic death/cloning** ($-\delta\tau\hat{\mathbf{H}}_{\text{d}}^{\mathcal{S}}\mathbf{c}^{\mathcal{S}}$): If $\mathbf{i} \in \mathcal{S}$, spawn a walker on \mathbf{i} with signed weight $-\delta\tau(H_{\mathbf{ii}} - S)c_{\mathbf{i}}$.
- **Deterministic spawning and death** ($\hat{P}^{\mathcal{D}}\mathbf{c}^{\mathcal{D}}$): A matrix-vector multiplication and a vector-vector addition are performed on the vector containing deterministic populations.
- **Annihilation** ($\mathbf{I} - \hat{P}\mathbf{c}$): Add the weights of all walkers on the same determinant. In practice this is performed separately for deterministic and stochastic states.

A sensible choice of the deterministic space would be the set of determinants with strong connections to the reference determinant which means $\hat{\mathbf{H}}^{\mathcal{D}}$ would be relatively dense (vanishing elements can still occur due to symmetry, for example). We can then view a single step of ss-FCIQMC as a massive matrix-vector multiplication with the dense part performed exactly and the sparse part performed stochastically, which is guaranteed to reduce the stochastic noise.

5.1.2 Semi-stochastic CCMC

As CCMC is algorithmically related to FCIQMC, we expect a semi-stochastic CCMC (ss-CCMC) algorithm to be viable and likewise reduce the stochastic noise in the CCMC method.

Comparisons to ss-FCIQMC

The differences between ss-CCMC and ss-FCIQMC relate to the underlying CCMC and FCIQMC algorithms. The most prominent difference is that the dynamical objects in FCIQMC are the many-body states $\{|D_i\rangle\}$, *i.e.*, Slater determinants, which cannot be combined; but in CCMC the dynamical objects are excitors $\{\hat{a}_i\}$, which are combined to form clusters. These clusters are then the object capable of ‘spawning’ onto another excitor (a single excitor can indeed form a cluster, but they’re conceptually distinct).

The major implication of this is that the populations on excitors are coupled (as evident from the name *coupled cluster*). Unlike in ss-FCIQMC, where the deterministic vector can be directly picked from the current wavefunction (*i.e.*, the `psip_list` object), in ss-CCMC we need to add up contributions of the non-composite cluster and multiple composite contributions from stochastically formed clusters.

The fact that the dynamical objects in CCMC need to be stochastically combined also requires that they frequently move across distributed memory partitions (*i.e.*, ‘processors’ in the MPI sense, since CCMC employs OpenMP for intra-node shared-memory communications), so that all possible combinations of excitors can be formed [102]. This has implications on the way we implement the MPI parallelism, which are discussed in [Section 5.4](#).

Another minor difference that nonetheless requires careful treatment is that the Hamiltonian elements are subject to sign changes with respect to their ss-FCIQMC counterparts, detailed below in [Section 5.3.2](#)

5.2 Selection of deterministic space

- **From the MP1 wavefunction:** The MP1 doubles amplitudes are correct to the first order [5, Ch. 14.3]. Therefore, including all excitors in the MP1 wavefunction is a sensible choice. This is simply done by including all double excitations from the reference determinant. This is similar to the strategy of including determinants in a truncated CI expansion in ss-FCIQMC.
- **From a complete active space (CAS):** When the system is significantly multi-reference, a CAS is a more suitable multi-determinantal zeroth order wavefunction. Especially in

conjunction with a multi-reference CCMC calculation that uses the CAS as the model space, this is expected to capture the important space quite well.

- **From a fully stochastic calculation:** Leveraging the ability of CCMC (and FCIQMC) to capture the important contributions to the wavefunction, a natural way to establish the deterministic space is to run a short but equilibrated calculation. We can establish a list of important excitors by directly ranking the excitor population in a snapshot or by time-averaging to achieve a finer-grained description of the important space.

All of the above selection criteria have been implemented in the HANDE-QMC code base.

5.3 Algorithmic considerations and OpenMP parallelism

5.3.1 Initialisation

After selecting the deterministic states, they are not treated differently than their stochastic counterparts: they reside in the same wavefunction object (`psip_list`). The only identifier is an array of ‘deterministic flags’, with one element assigned to every state in the `psip_list`.

A hash table of deterministic states *on all processors* is prepared for the inquiry of whether a cluster belongs to the deterministic space. A hash table is chosen for its $\mathcal{O}(1)$ lookup time as this needs to be performed whenever a cluster is selected, which needs to be one of the fastest processes in a CCMC calculation.

5.3.2 Deterministic Hamiltonian

Assuming a distribution of deterministic states onto each MPI processor has been performed, we can then form the deterministic Hamiltonian $\mathbf{H}^{\mathcal{D}}$, defined by

$$H_{ij}^{\mathcal{D}} = \langle D_i | \hat{\mathbf{H}} | D_j \rangle, \forall i, j \in \mathcal{D}. \quad (5.4)$$

Although $\mathbf{c}^{\mathcal{D}}$ is dense (as it contains the exact excitor amplitudes instead of the stochastically rounded ones that can be zero), and is therefore stored as an ordinary vector, $\mathbf{H}^{\mathcal{D}}$ can contain zeroes owing to vanishing integrals due to symmetry; due to the determinants being more than two excitations apart; or simply being smaller than a pre-set threshold. For this reason we store the deterministic Hamiltonian in a sparse format to save memory.

In this implementation, the ‘compressed sparse row’ (CSR) is used, which stores information about the non-zero elements in three separate arrays: `mat`, `col_ind`, and `row_ptr`. For an arbitrary matrix with n_{nz} non-zero elements and n_{row} rows, the first array, n_{nz} long, contains

the values of all non-zero entries; and the second array of the same length contains the column indices of the corresponding entries; the third list, of length $n_{\text{row}} + 1$, whose i -th element is the number of non-zero elements above the i -th row, plus one. Figure 5.1 illustrates the CSR format, in 1-indexing. As can be seen, this data structure allows easy access of the matrix row-by-row (via the `row_ptr` array), which is useful in performing a matrix-vector multiplication, one of the main computational tasks in a deterministic projection.

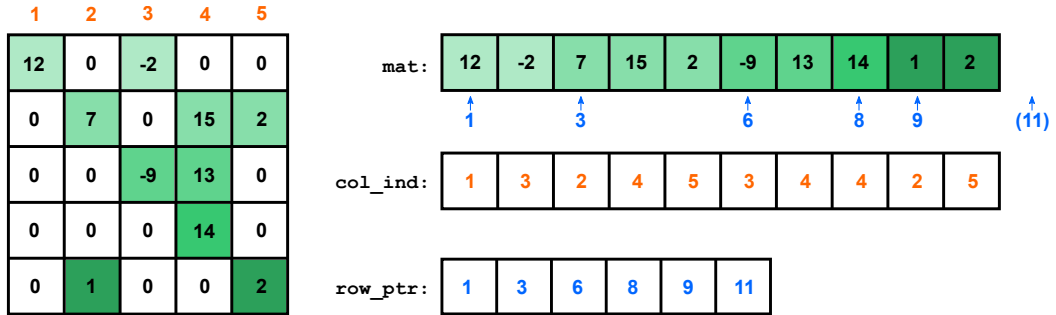


Fig. 5.1 The compressed sparse row (CSR) format of storing sparse arrays. This is, in fact, a poor use of the CSR format as 26 integers are stored instead of 25 in the full matrix, but the memory savings would be significant for larger and sparser matrices, such as most molecular Hamiltonians.

Another subtle detail is the sign changes for the Hamiltonian elements. This is due to the presence of annihilation operators in each of the excitors, so in applying one or more excitors to the reference determinant to obtain another excited determinant, anti-commutation rules between second-quantised creation and annihilation operators need to be applied. For example:

$$\begin{aligned}
 & \hat{a}_{ik}^{ab} |ijk\rangle \\
 &= \hat{a}^\dagger \hat{b}^\dagger \hat{k} \hat{i} \hat{i}^\dagger \hat{j}^\dagger \hat{k}^\dagger |\text{vac}\rangle \\
 &= \hat{a}^\dagger \hat{b}^\dagger \hat{k} \hat{j}^\dagger \hat{k}^\dagger |\text{vac}\rangle \\
 &= -\hat{a}^\dagger \hat{b}^\dagger \hat{k} \hat{k}^\dagger \hat{j}^\dagger |\text{vac}\rangle \\
 &= -\hat{a}^\dagger \hat{b}^\dagger \hat{j}^\dagger |\text{vac}\rangle \\
 &= -|abj\rangle
 \end{aligned} \tag{5.5}$$

where the negative sign is a result of the anti-commutation relation amongst the creation operators $[\hat{i}^\dagger, \hat{j}^\dagger]_+ = 0$ [5, Ch. 1.2.1].

5.3.3 Accumulation of the deterministic vector

The deterministic amplitudes are gathered by looping over all states on a processor, which are necessarily non-composite excitors, and copying the deterministic amplitudes when a deterministic flag is encountered. The original CCMC algorithm is fully stochastic in the cluster sampling step, hence lacking the deterministic looping over all non-composite clusters. The recent ‘full non-composite’ modification (Section 1.3.4, [51]) introduces this explicit looping, therefore the semi-stochastic CCMC algorithm requires it to be enabled.

As discussed in Section 5.1.2, in FCIQMC, this accumulation only has one contribution that is the population on a determinant. However, the mapping of CI expansion coefficients to coupled cluster amplitudes results generally in a sum, including a non-composite (single amplitude) contribution, and multiple composite (product of amplitudes) contributions. We define the CI coefficient for a determinant $|D_i\rangle$ in the CC formalism as $\tilde{t}_i \equiv c_i = \langle D_i | \Psi^{CC} \rangle$. For example $\tilde{t}_{ij}^{ab} = t_{ij}^{ab} + t_i^a t_j^b - t_i^b t_j^a$. Enumerating these contributions is possible, and reduces to a cluster analysis task [103]. But exactly summing these contributions is not practical for two reasons: firstly, this requires the repeated querying of positions in the `psip_list` of all the contributory excitors, many of which could be zero or simply not exist due to being in the stochastic space; secondly, some contributory excitors may exist on another processor altogether, so querying their positions, and fetching their populations, require time-consuming MPI communications.

Therefore, we propose to only accumulate the composite amplitudes stochastically, which requires no overhead in cluster analysis or MPI communications. This however, does mean a small noise in the calculation will be present even in the limit that all excitors are made deterministic, see Figure 5.3 for example. This is done in the ‘stochastic’ attempts in a CCMC iteration, where composite clusters are allowed to form from stochastic combinations of excitors. In our algorithm, if a composite cluster collapses into a deterministic excitor, the composite amplitude is added to the deterministic amplitude, after reweighting with the probability, p_{gen} , that the cluster could have been formed randomly, such that:

$$\tilde{t}_i = t_i + \sum_{\hat{a}_j \dots \hat{a}_k = \pm \hat{a}_i}^{\text{stoch.}} \frac{t_j \dots t_k}{p_{\text{gen}}}, \quad (5.6)$$

where the ‘stoch.’ superscript indicates a sum over stochastically formed clusters that happen to collapse onto \hat{a}_i . Further complications arising from the use of MPI parallelism are deferred to Section 5.4.

5.3.4 OpenMP parallelism

The adaptation of the above-mentioned algorithm with OpenMP parallelism is fairly straightforward, as the main sampling code is already OpenMP-parallelised. A single Boolean flag, `determ_parent`, is made private to each thread. It informs spawning routines whether the ket-cluster belongs to the deterministic space, for cancellation of the spawning attempt if the bra-excitor is also deterministic.

The routine that requires special attention is `set_determ_info`, which accumulates the deterministic amplitudes as described above. This routine finds the location in the deterministic vector that the current ket-determinant (or cluster) amplitude should augment, and also records its index in the overall `psip_list`. The ss-FCIQMC implementation relies on the fact that the loop counters are iterated through sequentially on an MPI processor, which allows a simple counter-based algorithm to perform both tasks. The direct analogue of this loop is the non-composite loop in CCMC, where we need to collect the non-composite amplitudes. With OpenMP parallelism, the order of the iterations becomes non-deterministic and we cannot simply reuse the FCIQMC code. A lightweight modification to the deterministic flags array. In ss-FCIQMC this is an integer array, with 0 meaning a deterministic state and 1 meaning a stochastic state. With the proposed modification, this array now stores non-negative values $\text{flag}(i)$, with $\text{flag}(i) = 0$ meaning the state at index i of the `psip_list` is a *stochastic* state, and $\text{flag}(i) = k > 0$ meaning the state at index i has the index of k in a sorted list of all the deterministic states. At the end of each iteration, the annihilation routines will shift the flags as new states are inserted or empty states removed, but as the `psip_list` remains sorted, the non-zero flags remain sorted.

The composite (and hence stochastic) contributions are treated differently, as they're formed of multiple excitors and hence does not have a deterministic flag associated with the cluster. We have to perform a binary search over the deterministic states to inquire the index that should be updated. This should not be overly expensive as the average time complexity of the binary search is $\mathcal{O}(\log n)$ [104], and furthermore we only perform this search if we know, from a hash lookup, that the cluster under consideration indeed collapses onto a deterministic state.

5.4 MPI parallelism

5.4.1 Accumulation of the deterministic vector

The main challenge to introducing MPI parallelism to the ss-CCMC algorithm arises from the fact that excitors are 'itinerant', *i.e.*, they move across processes to reduce biases in cluster sampling. This results in the need to manage the trade-off between memory and speed, specif-

ically the volume of MPI communications. Due to the presence of composite contributions to deterministic amplitudes, which can be formed in processes other than the one that the deterministic excitor resides in. Extra MPI communications are therefore inevitable, specifically, [Equation \(5.6\)](#) would now read:

$$\tilde{t}_i = t_i + \underbrace{\sum_{\substack{\text{stoch.} \\ \hat{a}_j \dots \hat{a}_k = \pm \hat{a}_i \\ \hat{a}_j, \dots, \hat{a}_k \in \text{iproc}}} \frac{t_j \dots t_k}{p_{\text{gen}}}}_{\text{From own process}} + \underbrace{\sum_{\substack{\text{stoch.} \\ \hat{a}_1 \dots \hat{a}_m = \pm \hat{a}_i \\ \hat{a}_1, \dots, \hat{a}_m \notin \text{iproc}}} \frac{t_1 \dots t_m}{p_{\text{gen}}}}_{\text{MPI-communicated}}, \quad (5.7)$$

where ‘iproc’ indicates the process that state i resides in. This extra MPI communication cannot be avoided because the stochastic states are itinerant, so the stochastic contributions from each process are necessarily unique, resulting in the need for the second sum to be performed by MPI.

5.4.2 Distribution of deterministic states

There are two overarching ways to introduce MPI parallelism to the foregoing algorithm, and they mainly differ in how the deterministic states are distributed.

Due to the need for cooperative spawning (*i.e.*, excitors in the `psip_list` combining to form clusters), excitors need to be shifted around MPI processors for all excitors to be able to ‘meet’ all other excitors on average. The unfortunate implication for the semi-stochastic algorithm is that we either need to move the deterministic states like all the other states and re-form the deterministic Hamiltonian at every time step, or we must cope with storing the full Hamiltonian on all the processors.

This choice is exposed to the user, as the former is more suitable for extended systems where the re-formation of the deterministic Hamiltonian is expected to be a negligible part of a time step, and the latter is suitable for small systems where only a few MPI processors are used. The memory requirement of the latter is also alleviated by the use of intra-node OpenMP parallelism, resulting in more memory being available for each MPI process.

If we choose to store the full deterministic Hamiltonian on each processor, we seem to have two, non-equivalent, ways to achieve this:

1. Have the full set of deterministic states on all processors. We term this option the ‘replicated sampling’ scheme. This was investigated but was deemed to be overly complicated, on top of having a steeper memory scaling than the alternative. We detail this scheme only in [Appendix C](#).

2. Each processor only gets a unique subset of deterministic states, as determined by the hash procedure outlined in [102, Sec. III]. This requires the states to be distributed by the pre-existing annihilation framework in HANDE, which automatically assigns processors to states and handles the MPI communications. We call this the ‘integrated sampling’ scheme.

5.4.3 Integrated sampling scheme

In this implementation, we require additional small auxiliary arrays to keep track of the deterministic states as they move MPI processes. The modification to the deterministic flags in Section 5.3.4 comes in especially handy as it makes performing the second sum in Equation (5.7) tractable: referring to Figure 5.2, we propose to accumulate all deterministic amplitudes, whether non-composite or composite, to the `full_vector` array, instead of `vector` as in ss-FCIQMC. For non-composite amplitudes, given an index i of an excitor in the `psip_list`, the index of `full_vector` that it should accumulate to can be quickly retrieved from `flag(i)`, and after the `MPI_AllReduce` call, the `vector` array holding amplitudes belonging to deterministic states on this processor can be quickly extracted from `full_vector` by inquiring `det_indices`. If a full Hamiltonian is stored, the appropriate rows of the Hamiltonian can also be extracted by `det_indices`.

After the deterministic projection, the redistribution of excitors will take place. The flags of the deterministic excitors are communicated *via* the `spawn` array, and the flags are then reinstated on the target processors by the annihilation framework, specifically, all actual spawns are given a spawn flag of 0, whether it is onto a deterministic excitor, and only redistributed deterministic excitors are given a spawn flag of its `flags` array value. In annihilation, bitwise OR operations are used to reinstate the deterministic flag of an excitor.

5.5 Results and discussion

Unless stated otherwise, all calculations, single- or multi-reference, are with truncation level 2 (CCSD) out of all references. MPI parallelisation is not used in these calculations, however, OpenMP parallelisation is employed.

We first present, in Figure 5.3, the simplest system under study: the square H_4 /STO-3G system at 1.0\AA separation. The RHF solution has 4 molecular orbitals, the two references we use are the lowest (HF) and highest determinants. The system has 10 determinants in the Hilbert space (the A_g symmetry sector under D_{2h}). It is a prototypical multi-reference system. The RHF solution does not predict the HOMO and the LUMO to be degenerate, as expected

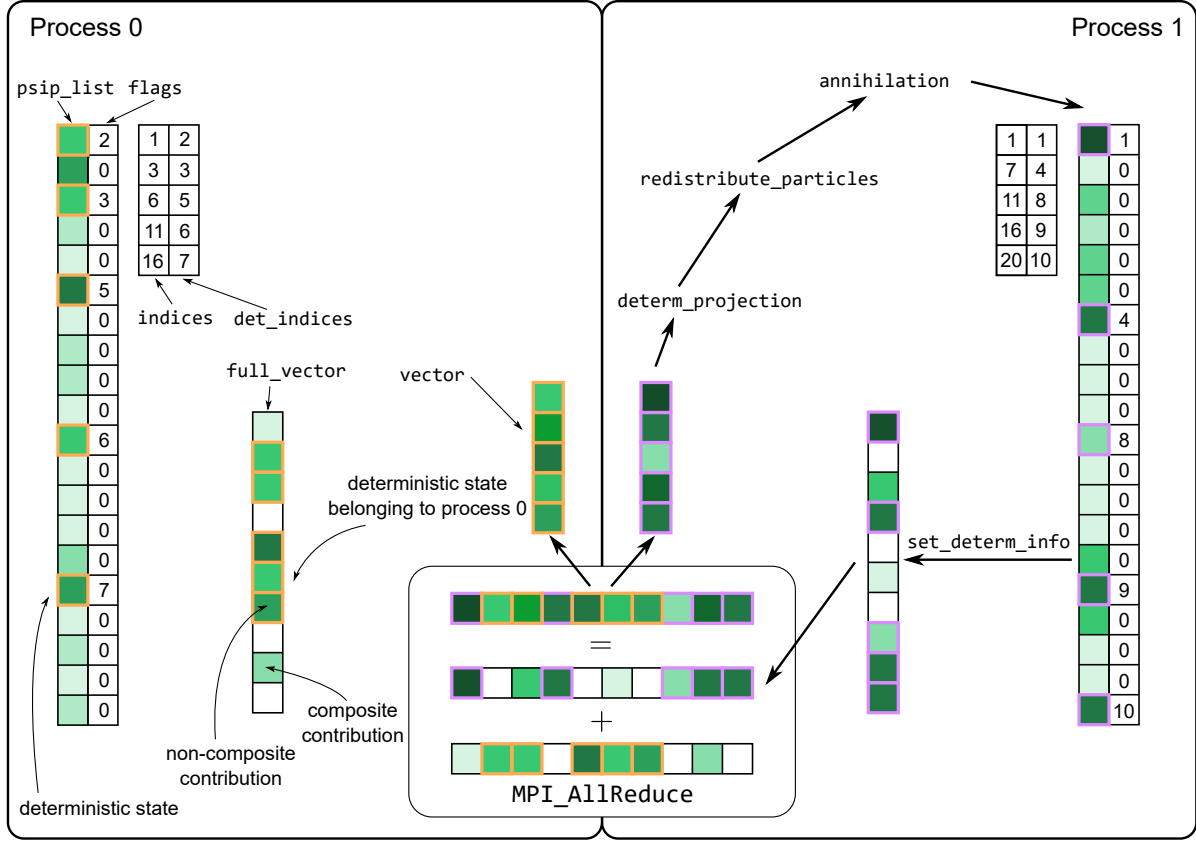


Fig. 5.2 An illustration of the MPI parallelism of the semi-stochastic CCMC algorithm. Each process has 20 states in total, of which 5 are deterministic. The `psip_list` stores the information on the local wavefunction, with each coloured square representing a unique excitor, and the strength of the green colour representing its absolute population. The thick border around an excitor means it is a deterministic excitor, with orange belonging to processor 0 and purple belonging to processor 1. During each CCMC iteration, `full_vector` is accumulated into. During the full non-composite loop, the deterministic exciters directly store their populations into indices of `full_vector` that their flags values corresponds to; and during the stochastic loop, if a sampled cluster collapses onto a deterministic state (which can be currently on any processor), the corresponding entry of `full_vector` is written into. After the sampling loops, the `full_vector` from all of the processors are added together to obtain the actual deterministic amplitudes belonging to each process. Each process extracts the correct amplitudes from `full_vector` to `vector` using the indices stored in `det_indices`. `vector` is then multiplied with the deterministic Hamiltonian. `indices` is used in the annihilation process to make sure the deterministic flags are merged correctly.

from a simple MO analysis. The multi-reference nature can be seen to arise from the need to recover the exact degeneracy by significantly occupying the lowest double excited determinant ($|{}_{22}^{33}\rangle$). The two-reference CCSD model is equivalent to FCI (red dotted line) and FCIQMC (Figure 5.4), whose results are easily available. The ss-CCMC algorithm can clearly reduce

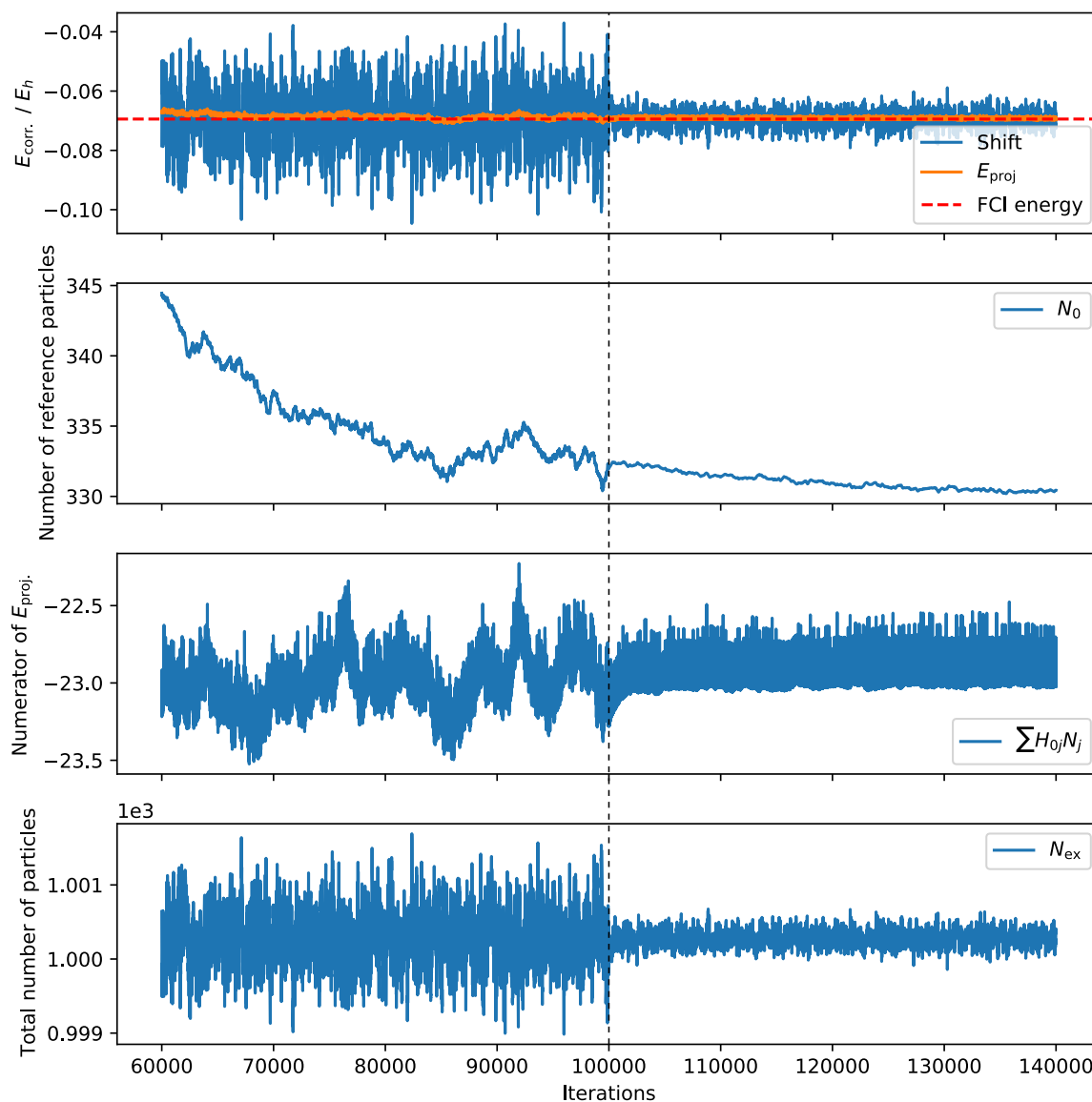


Fig. 5.3 The two-reference CCMC with the four-level linear H4 model in the STO-3G basis at 1.0 Å separation, with all 10 excitors included in the deterministic space. The switching on of the the semi-stochastic algorithm is indicated by the dotted line. Even with all excitors in the deterministic space, the residual sampling noise can still be observed. This is to be contrasted with the ss-FCIQMC result in Figure 5.4 on the same system, where no sampling noise is present.

stochastic noise dramatically. The above figure also shows that the algorithm is not able to eliminate noise completely, even if all states are in the deterministic space. The reason for this is that the sampling of the exponential *ansatz* is still stochastic, *i.e.*, the sum in Equation (5.6) is still stochastic. We can then conceptually break down the overall stochastic noise into two parts: *projection noise* and *sampling noise*, with the ss-CCMC algorithm being able to eliminate the former but not the latter. In the simpler algorithm of FCIQMC where only the projection noise is present, we expect the same system in FCIQMC to be completely noise-free, which is indeed the case in Figure 5.4, as it reduces to a simple, deterministic matrix-vector multiplication at each step.

The HOCl system in Figure 5.5 shows an example of when the semi-stochastic adaptation is of limited benefit: the size of the Hilbert space of the system approximately 4.45×10^3 at CCSD level, and with almost one-third of the Hilbert space in the deterministic space, the reduction in noise is modest. This is, however, expected as this is an essentially single-reference system (the \mathcal{T}_1 diagnostic [105] is 7.12×10^{-3} , whereas only systems with $\mathcal{T}_1 \geq 2 \times 10^{-2}$ are generally regarded as multi-reference), the wavefunction is dominated by a single reference determinant (the HF determinant). As a result the projection noise due to non-HF excitors is low in the first place, and sampling noise predominates. The reference excitor, being spawned from deterministically in the CCMC algorithm, has an inherently lower projection noise than other excitors, and no sampling noise at all. This can be seen from the fact that the noise in N_0 has decreased appreciably, with the only noise in it being from clusters that happen to spawn back onto the determinant *via* the random excitation generator, and with most of the doubles space being deterministic, and singles being unconnected to $|D_0\rangle$ by Brillouin's theorem, even this remaining sampling noise in N_0 is significantly reduced.

The foregoing suggests that the noise in N_0 can be significantly reduced by the semi-stochastic algorithm. The noise in $\sum_j H_{ij}N_j$ can be seen to also reduce. A similar argument to the above can be applied here. Additionally, the noise is reduced by the fact that most double excitors are in the deterministic space (we can enforce this by using the MP1 space, for example), and so will be sampled by the full non-composite loops. However, the sampling noise contributing to $\sum_j H_{ij}N_j$ is higher than that of N_0 's, since Brillouin's theorem does not apply to double excitors, that is to say, there will be more stochastic spawns onto double excitors. But overall the reduction in noise in both $\sum_j H_{ij}N_j$ and N_0 reduces the error in the estimator for projected energy (see Section 1.3.3).

A system that ss-CCMC is expected to be more applicable is the $C_2/cc\text{-pVDZ}$ system, shown in Figure 5.6. From our discussion before in Chapter 2, it is known to be highly multi-reference, and hence would suffer from significant projection noise without ss-CCMC. And indeed, a

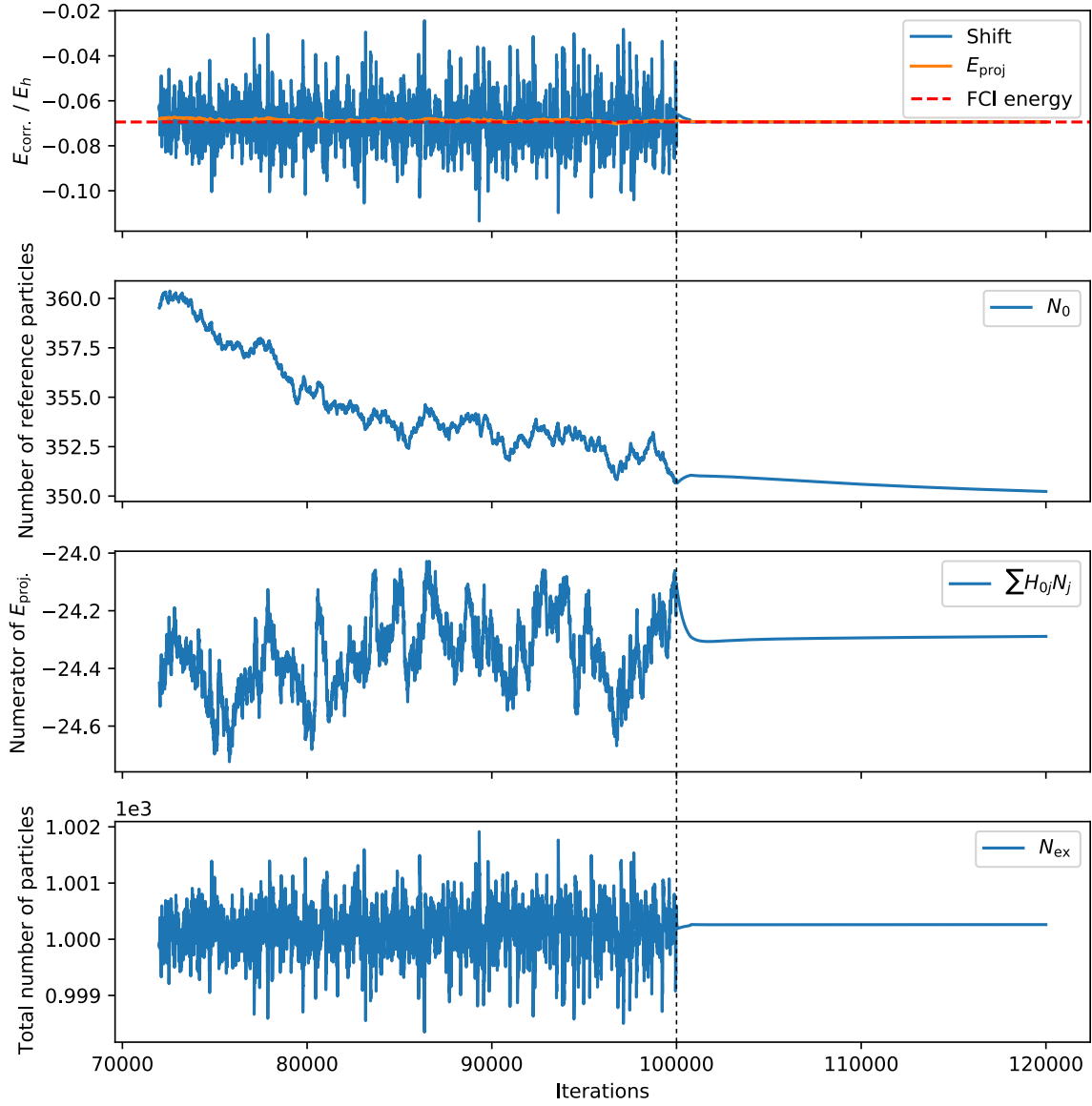


Fig. 5.4 FCIQMC results from the H4/STO-3G system run with a fully stochastic algorithm for 100000 iterations, after which semi-stochastic FCIQMC is turned on (indicated by the dotted line) with all determinants included in the deterministic space. As the entire calculation is now deterministic, no noise whatsoever is observed from iteration 100000 onwards.

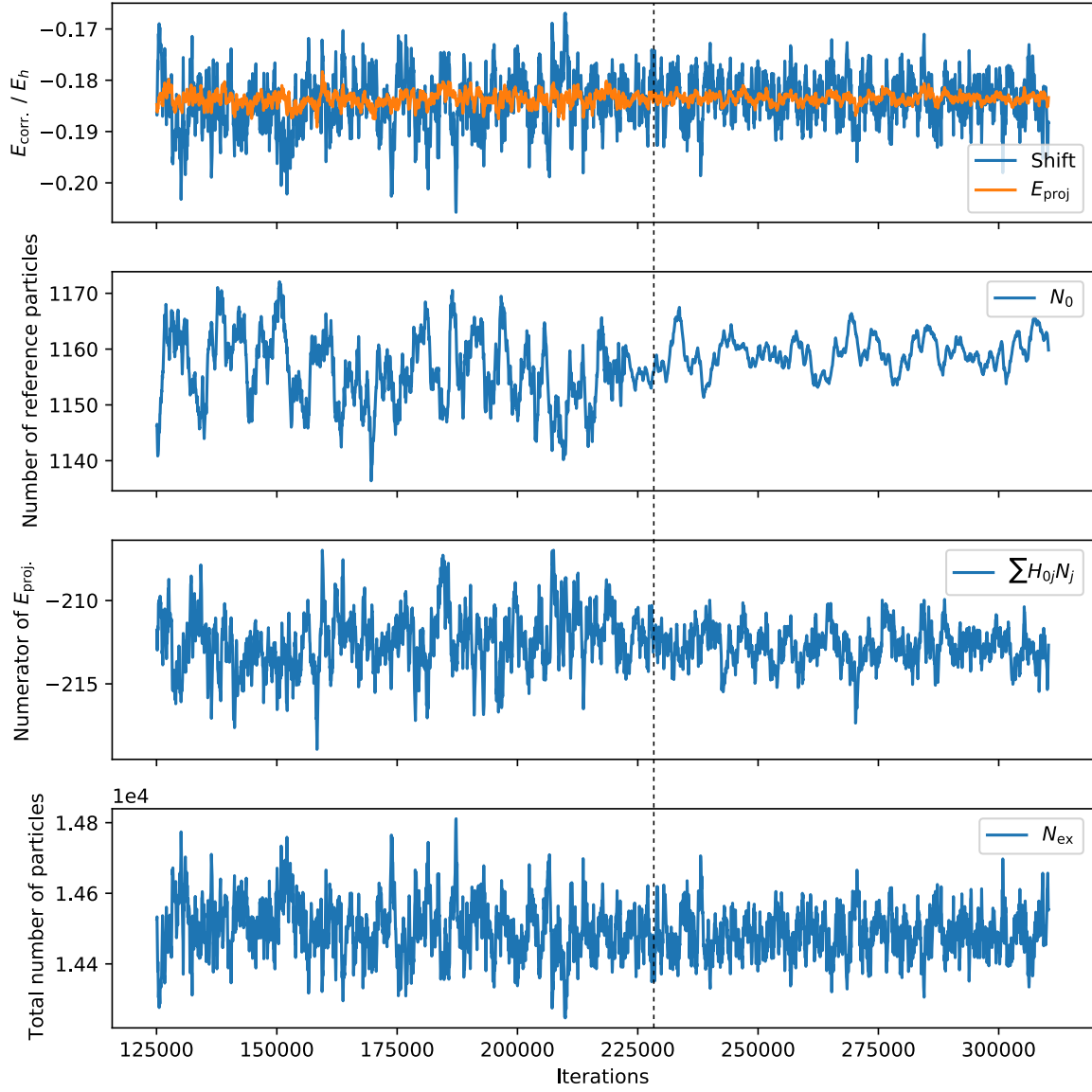


Fig. 5.5 The single-reference HOCI/6-31G system, at equilibrium geometry, with 1000 states that are instantaneously most populated chosen to be the deterministic space. The switching on of the semi-stochastic algorithm is indicated by the dotted line.

significant reduction in noise can be achieved by making a small fraction (2761 excitors) of the Hilbert space deterministic.

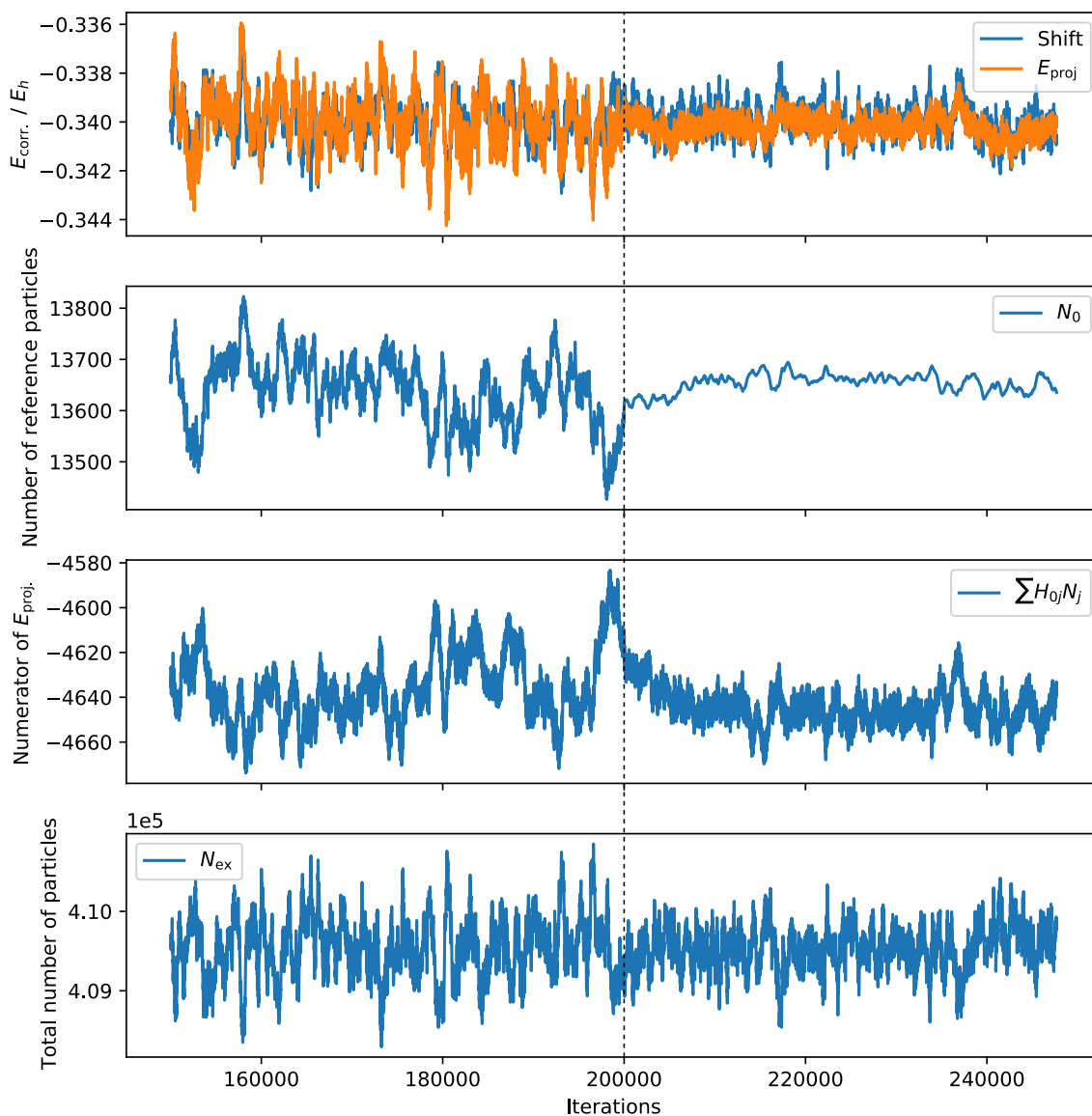


Fig. 5.6 The $C_2/cc\text{-pVDZ}$ system at 1.2\AA bond length, with the complete $(8e, 8o)$ CAS as the reference space, with a deterministic space consisting of all double excitors. The switching on of the the semi-stochastic algorithm is indicated by the dotted line.

Chapter 6

Conclusions and outlook

6.1 Concluding remarks

This work focused on accelerating the convergence of the MR-CCMC method, and making its operation more user-friendly and black-box. We achieved this goal by focusing development efforts on four main areas, each of them accelerates parts of the MR-CCMC method. Some of these are exact algorithms, while the others are approximations.

We started off in [Chapter 2](#) by introducing the BK-tree based acceptance search algorithm that speeds up considerably the most frequent processes in the CCMC algorithm, namely, cluster sampling, spawning and death. A series of further approximations were then introduced, including symmetry screening and cluster discarding. The former was shown to lead to almost no loss in accuracy, and the latter was shown to, contrary to initial expectations, not lead to a consistent and extrapolatable behaviour, and requires extensive benchmarking before use.

We then, in [Chapter 3](#), took further the idea that the reference space can be compressed, sometimes drastically, while retaining most of the correlation energy. We investigated using CASCIQMC as a static correlation solver that generates the model space in a MR-CCMC calculation, by letting important determinants emerge by a time-averaged calculation. We concluded that the algorithm provided a robust and black-box way of generating the model space for a multi-reference calculation, that is able to dynamically respond to how multi-reference a system is, and automatically adjust the size of the model space.

Taking a different approach in [Chapter 4](#), we investigated a series alternative projectors to the standard first-order Taylor expansion to the exponential projector, based on the Chebyshev polynomial expansion of the wall function, which is the underlying function of the ground state projector. The wall-Chebyshev projectors were shown to have a range of desirable qualities that make them more efficient than the standard projector, and also fairly easy to implement in code.

Back to the linear projector in [Chapter 5](#), but now with a part of the projection performed deterministically. A range of implementational considerations arising from the complex CCMC algorithm, especially concerning its mixed OpenMP/MPI parallelisation, were discussed in some detail. The resulting semi-stochastic CCMC algorithm is able to reduce statistical noise, and therefore speed up statistical convergence drastically while introducing minimal cost.

6.2 Future work

This thesis is mainly concerned with the theoretical formulation and code implementation of the methods introduced herein. These methods have allowed much larger systems to become within reach by the MR-CCMC algorithm, and made into a worthy competitor against FCIQMC. Therefore, a range of large system with significant static correlation can be considered, for example, Cr_2 ([\[106\]](#)), and the singlet-triplet gap of n -acenes ([\[107\]](#)).

Additionally, in the course of our investigations, the case of the carbon dimer at separations larger than 1.5 Å stood out as being uniquely difficult to treat with the MR-CCMC algorithm, even with all the new machinery being applied to it. We concluded that this was caused by the avoided crossing at slightly beyond 1.5 Å, causing the Hartree–Fock reference to be no longer the most highly occupied state. We are in the process of reworking the MR-CCMC method, which is essentially a modified single-reference method. This involves, in short, modifying the CCMC *ansatz*, currently $N_0 \exp(\hat{T}/N_0)|\Phi\rangle$, such that when N_0 is no longer the largest population, the exponential still converges. This work is ongoing, and initial tests showed promising results.

As mentioned in [Section 3.4.2](#), a simple extension to the tailoring algorithm can be to truncate by an energy criterion, which is expected to improve the non-parallelity error in binding curves.

On the computational side, the scaling behaviour of the semi-stochastic CCMC calculation can be investigated, and the MPI communication pattern can be optimised, if necessary. Faster approximate search algorithms have come to our attention, for example the SymSpell algorithm¹ that promises orders of magnitude faster performance than the BK-tree algorithm. These promise to essentially eliminate the cost of determinantal search in the MR-CCMC algorithm.

¹Available at <https://github.com/wolfgarbe/SymSpell>

Appendix A

The model space compression theorem

As mentioned in [Section 2.3](#), we now outline a theorem that enables us to obtain a compressed model space from a CAS. Assuming we have a (ne, no) CAS, and that n is even, one such subset is the *unique* overlap between the Hilbert space \mathcal{H}_P out of the full CAS model space, \mathcal{M}_P , at a lower, desired truncation level P , and the Hilbert space \mathcal{H}_Q out of a two-reference model space, \mathcal{M}_Q , at a truncation level Q where $Q > P$. The latter calculation is defined as two references at the bottom and top of the CAS (*i.e.*, filled with the *Aufbau* and ‘anti-*Aufbau*’ principles respectively), with a truncation level of $Q = n/2$ so that the two references are at least connected by one configuration [\[52\]](#). We partition the orbitals into core (C, doubly occupied in all CAS determinants), active (A, variably occupied in CAS determinants), and virtual (V, unoccupied in all CAS determinants) sets, and a general excitation from a model space determinant in which n core electrons is excited into m active orbitals and $(n - m)$ virtual orbitals, for example, is written as $n\text{C} \rightarrow m\text{A}(n - m)\text{V}$. An illustration of the set-up is shown in [Figure A.1](#).

Lemma A.0.1. \mathcal{H}_P does not contain determinants of the form $x\text{C} \rightarrow \dots$ and $\dots \rightarrow x\text{V}$ where $P < x \leq Q$, but \mathcal{H}_Q does.

Proof. Any such determinant will need at least $x > P$ electrons being excited from a model space determinant in \mathcal{M}_P , which requires a truncation level larger than P . \square

Lemma A.0.2. For the remaining determinants in \mathcal{H}_Q (*i.e.*, those involving P or less excitations), if an excitation involves a change in the number of active electrons, then it will be reachable within P excitations by more than one model space determinant in \mathcal{M}_P .

Proof. Consider a general excitation of $x\text{C}y\text{A} \rightarrow (x + y - z)\text{A}z\text{V}$, where $x, z \leq P$. Defining $k \equiv x - z$ as the change in the number of active electrons, then $|k| \leq P$. There will be x holes in C, z particles in V, and k holes or particles in A, depending on its sign. Consider the $k > 0$

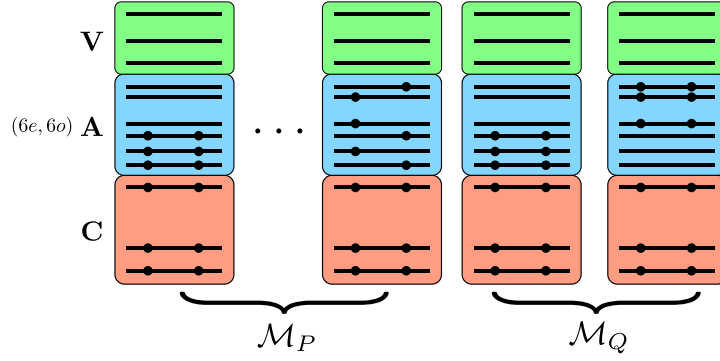


Fig. A.1 A generic system with a $(6e, 6o)$ CAS. The \mathcal{M}_P model space consists of all possible CAS determinants, while the \mathcal{M}_Q model space is made up of the bottom and top determinants in the CAS. We allow P -fold excitations from \mathcal{M}_P and Q -fold excitations from \mathcal{M}_Q , where $Q > P$. In this case, the sensible choice is $P = 2$ and $Q = 3$.

case now, which means there are z number of $C \rightarrow V$ excitations, which can be generated by any \mathcal{M}_P determinant, and k number of $A \rightarrow V$ excitations, which can be generated by any \mathcal{M}_P determinant with the same configuration, except for the k electrons that are excited into V , which can be anywhere in A , and since \mathcal{M}_P contains all arrangements of active electrons in active orbitals, there are more than one determinant in \mathcal{M}_P that satisfy the above. The argument for $k < 0$ is similar. An example is shown in Figure A.2. \square

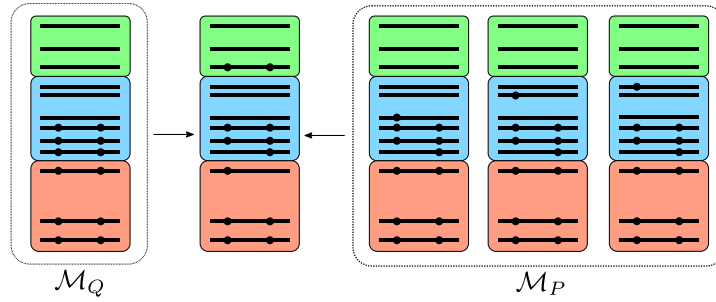


Fig. A.2 An example of Lemma A.0.2. The central configuration can be generated by a $1C1A \rightarrow 2V$ excitation from the bottom \mathcal{M}_Q determinant, which results in a decrease of 1 electron from the active space. On the right, we show that the same configuration can be generated by more than one \mathcal{M}_P determinant, via $1C1A \rightarrow 2V$ excitations, because the one active electron can come from any potential holes in the active space, given that the rest of the configuration is fixed.

Lemma A.0.3. *The inverse of the above only holds true when $x = P$.*

Proof. We would like to prove that, for excitations that preserve the number of active electrons, the excited determinant will be reachable within P excitations by only one determinant in \mathcal{M}_P if

$x = P$. We first need to prove that if $x < P$, the connection will not be unique. These excitations can be seen as a x -fold excitation from **C** to **V**, with $(P - x)$ internal **A** \rightarrow **A** excitations left, meaning more than one \mathcal{M}_P determinant can achieve the excitation. If $x = P$, all P available excitations will be used to generate the $x = P$ particles in **V**, leaving no remaining excitations to rearrange electrons in **A**, hence the determinants will be uniquely connected. A counterexample is shown in Figure A.3, where the readers can convince themselves that, if the left determinant were involved in an excitation of the type $1\mathbf{C}1\mathbf{A} \rightarrow 1\mathbf{A}1\mathbf{V}$, then the resulting configuration can only be generated by one \mathcal{M}_P determinant. \square

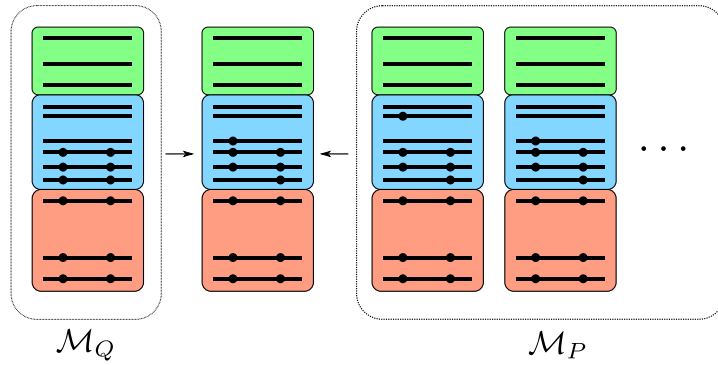


Fig. A.3 A counterexample of Lemma A.0.3. The central configuration is generated by a single excitation of the type $1\mathbf{A} \rightarrow 1\mathbf{A}$ excitation, which preserves the number of active electrons, from the bottom \mathcal{M}_Q determinant. We show on the right that this configuration can be generated by more than one \mathcal{M}_P determinant.

Theorem A.0.4. *The unique determinants in the overlap between \mathcal{H}_P and \mathcal{H}_Q can be enumerated by including up to $(Q - P)$ -fold excitations from the bottom and top determinants in \mathcal{M}_P .*

Proof. The above lemmas require $x = P$, which implies $y \leq (Q - P)$. $k = 0$ forces the required determinants to be generated by up to $(Q - P)$ -fold internal **A** \rightarrow **A** excitations from the \mathcal{M}_Q determinants, which are the bottom and top determinants. \square

Appendix B

Properties of projectors

B.1 Convergence properties of generators

We define here some summary properties of generators. The asymptotic rate of convergence of a propagator is dominated by the slowest-decaying eigencomponent:

$$\mu = \lim_{n \rightarrow \infty} \frac{||\Psi^{(n+1)} - \Psi_0||}{||\Psi^{(n)} - \Psi_0||} = \max_i \left| \frac{g(E_i)}{g(E_0)} \right|. \quad (\text{B.1})$$

[95] suggested that, in the common case that the first excited state is the slowest-decaying component, and that the first excited energy is small compared to the spectral range of \hat{H} , the above can be approximated as

$$\mu \approx |1 + (E_1 - E_0)g'(E_0)| \equiv |1 - \alpha\gamma|, \quad (\text{B.2})$$

where $\gamma = -g'(E_0)$ is the *convergence factor* for g . We now derive the relation given in [108] that γ is approximately the number of times, n , that g needs to be applied to achieve an error in the norm, $\epsilon = ||\Psi^{(n)} - \Psi_0||$ to the N -th decimal place:

$$\epsilon = 10^{-N} \approx (1 - \alpha\gamma)^n \quad (\text{B.3a})$$

$$10^{-N} \approx e^{-n\alpha\gamma} \quad (\text{B.3b})$$

$$n = \frac{N \ln 10}{\alpha\gamma} \equiv \kappa N \cdot \frac{1}{\gamma}, \quad (\text{B.3c})$$

where $\kappa = \ln 10 / (E_1 - E_0)$ is the convergence prefactor, which is inversely proportional to the first excited energy gap.

B.2 Higher Taylor expansions of the exponential projector

In [95] it was proposed that there is no gain in going to higher order Taylor expansions of the exponential projector, because all orders of expansion have $\gamma = \tau$ (see Appendix B.1). The conclusion is correct, but for a more subtle reason that we will now explain. The m -th order Taylor series expansion of g^{exp} is

$$\sum_{k=0}^m \frac{1}{k!} (-\tau)^k (x - E_0)^k. \quad (\text{B.4})$$

Equation (4.7a) requires that $g(E_{N-1}) < 1$, so, defining the *spectral range* $R = E_{N-1} - E_0$, we have

$$\left| \sum_{k=0}^m \frac{1}{k!} (-\tau)^k R^k \right| < 1. \quad (\text{B.5})$$

The $m = 1$ case leads to the familiar requirement in DMC, FCIQMC and CCMC that

$$\tau_{\text{max}} < \frac{2}{E_{N-1} - E_0} \quad (\text{B.6})$$

and solving Equation (B.5) numerically shows that higher order expansions lead to larger maximum allowed τ . In fact, asymptotically, τ_{max} increases linearly with a gradient of $1/e \approx 0.368$ (see Figure B.1). So, naïvely we can expect the efficiency to increase linearly with m . To prove the linearity, we note that $\tau_{\text{max}} R > 1$, and we can approximate $\sum_{k=0}^m |(-x)^k/k!|$ ($x \equiv \tau R$) with the leading order term $|(-x)^m|/m!$, and so we are left with

$$|(-x)^m| < m! \quad (\text{B.7a})$$

$$m \ln x \lesssim m \ln m - m \quad (\text{B.7b})$$

$$x < m e^{-1}, \quad (\text{B.7c})$$

where we used the Stirling's formula in the second line. Therein lies the real reason for not using higher order expansions: a naive implementation requires $m(m+1)/2$ applications of the Hamiltonian per projection, and even a factorised implementation would require m applications per projection, not to mention the lack of closed forms for the roots of the m -th order expansion, due to the Abel-Ruffini theorem ([109]), which shows that no analytical solution can exist for $m \geq 5$. In any case, the overall efficiency stays at best constant. Therefore, the conclusion that no gains can be made is correct, although a more tortuous argument is needed.

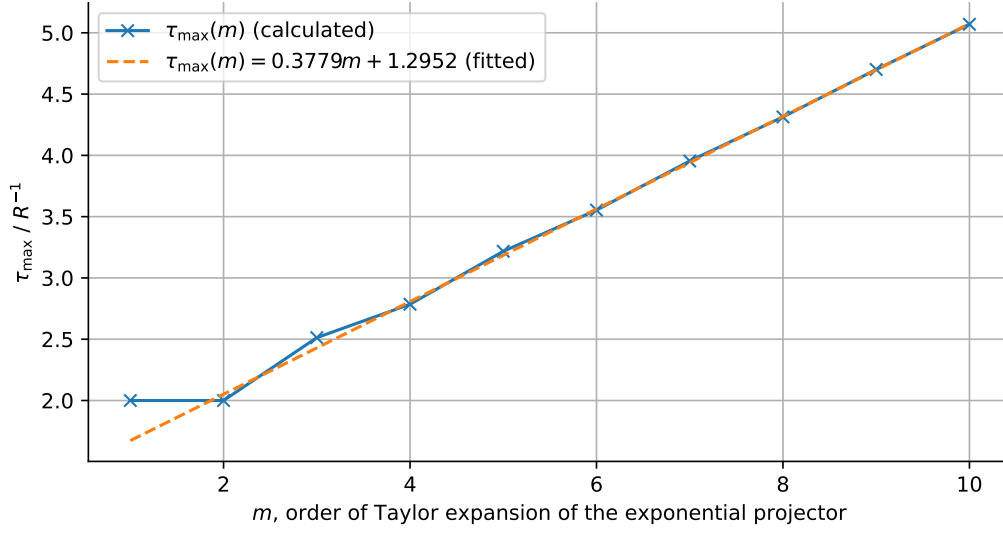


Fig. B.1 Calculated and fitted τ_{\max} as a function of the order of Taylor expansion of the exponential projector. There is indeed no gain whatsoever in going to the second order Taylor expansion, but there is in going to yet higher orders.

B.3 Properties of the wall-Chebyshev projector

Assuming the entire spectral range is re-scaled such that $x \in [-1, 1]$, where $x = 2(E - E_0)/(R - 1)$, and $R = E_{N-1} - E_0$ is the *spectral range* or the Hamiltonian, the Chebyshev expansion coefficients of the wall function is

$$\begin{aligned}
 c_k &= \int_{-1}^1 \text{wall}(x+1) T_k(x) (1-x^2)^{-1/2} dx \\
 &\equiv \int_{-1}^1 \text{wall}(x+1) T_k(x) \delta(x+1) dx \\
 &= (2 - \delta_{k0}) T_k(-1) = (2 - \delta_{k0}) (-1)^k,
 \end{aligned} \tag{B.8}$$

where the second line uses the fact that the wall function is zero everywhere but at the lower bound, so the weight function $(1-x^2)^{-1/2}$ has the same action as the delta function centred at -1 , $\delta(x+1)$. The last equality exploits a well-known identity of the Chebyshev polynomials

[110, p. 598]. We can then write the m -th order expansion as

$$\begin{aligned} g_m^{\text{wall-Ch}}(x) &= \frac{1}{1+2m} \sum_{k=0}^m (2 - \delta_{k0}) (-1)^k T_k(x) \\ &= \frac{1}{1+2m} \sum_{k=0}^m (2 - \delta_{k0}) T_k(-x), \end{aligned} \quad (\text{B.9})$$

where the last equality exploits the fact that T_k has the same parity as k [110, p. 597], and we scale the sum such that $g_m^{\text{wall-Ch}}(-1) = 1$.

To obtain an analytical expression for the zeroes of the wall-Chebyshev projector, we use the trigonometric definition of the Chebyshev polynomials. Inverting the sign of the argument in Equation (B.9), we have

$$\begin{aligned} g_m^{\text{wall-Ch}}(-\cos \theta) &\propto \sum_{k=0}^m (2 - \delta_{k0}) T_k(\cos \theta) \\ &= 1 + 2 \left[\sum_{k=0}^m \cos(k\theta) \right] \\ &= \frac{\sin[(m+1/2)\theta]}{\sin(\theta/2)}, \end{aligned} \quad (\text{B.10})$$

where the last equality is the Dirichlet kernel [111]. The zeroes of $g_m^{\text{wall-Ch}}(x)$ are then transparently

$$a_\nu = -\cos\left(\frac{\nu\pi}{m+1/2}\right), \quad \nu = 1, 2, \dots, m, \quad (\text{B.11})$$

where the negative sign is from account for the sign inversion in Equation (B.10). In an arbitrary spectral range other than $[-1, 1]$, these zeroes are

$$a_\nu = E_0 + \frac{R}{2} \left(1 - \cos \frac{\nu\pi}{m+1/2} \right). \quad (\text{B.12})$$

Knowing its zeroes, we can decompose $g_m^{\text{wall-Ch}}(x)$ into a product of linear projectors:

$$g_m^{\text{wall-Ch}}(x) = \prod_{\nu=1}^m \frac{x - a_\nu}{E_0 - a_\nu}, \quad (\text{B.13})$$

where the numerators ensure $g_m^{\text{wall-Ch}}(E_0) = 1$.

Appendix C

The replicated sampling scheme for semi-stochastic CCMC

In MPI-parallelising the ss-CCMC algorithm, if we choose to keep all deterministic states on all processes, we can make the sensible choice that, if a spawning is made onto a deterministic state, it will be sent to the spawning array destined for the same process, *i.e.*, we override the determinant hashing procedure in [102] for deterministic spawns.

This scheme appeared attractive at first, as it offered more stochastic cluster sampling of the deterministic states, *i.e.*, each deterministic state can ‘see’ all other states in a given time step, hence reducing stochastic noise from cluster sampling. It seemed that all we needed to do was to calculate p_{gen} differently for clusters containing deterministic excitors: originally for each excitor in the cluster, a factor of $1/N_p$ is applied to p_{gen} to account for the fact that the excitor could have resided in any other process; now we do not apply the factor if a constituent excitor is deterministic.

However, the main difficulty was the synchronisation of the deterministic populations. Referring to Figure C.1, assume we have a fully stochastic calculation with occupied stochastic states on all processes, and N_0 walkers on the reference. Now we choose a set of deterministic states, and they so happen to be all unoccupied except for the reference (which we always include in the deterministic space). For N_p MPI processes, we create the states on all processors, and for the reference we initialise its population to be N_0/N_p on all processes. After one time step, the deterministic projection and annihilation are performed, at which point all of the deterministic populations are still identical. However, after the merging of stochastic contributions onto the deterministic states, the deterministic populations on different processes will start to vary.

This synchronisation issue can only be solved by a ‘split’ spawning process, where if a spawn is from a stochastic state to a deterministic state, it is split evenly into N_p smaller spawns, which is then sent to all the processes. This would increase the volume of MPI communications,

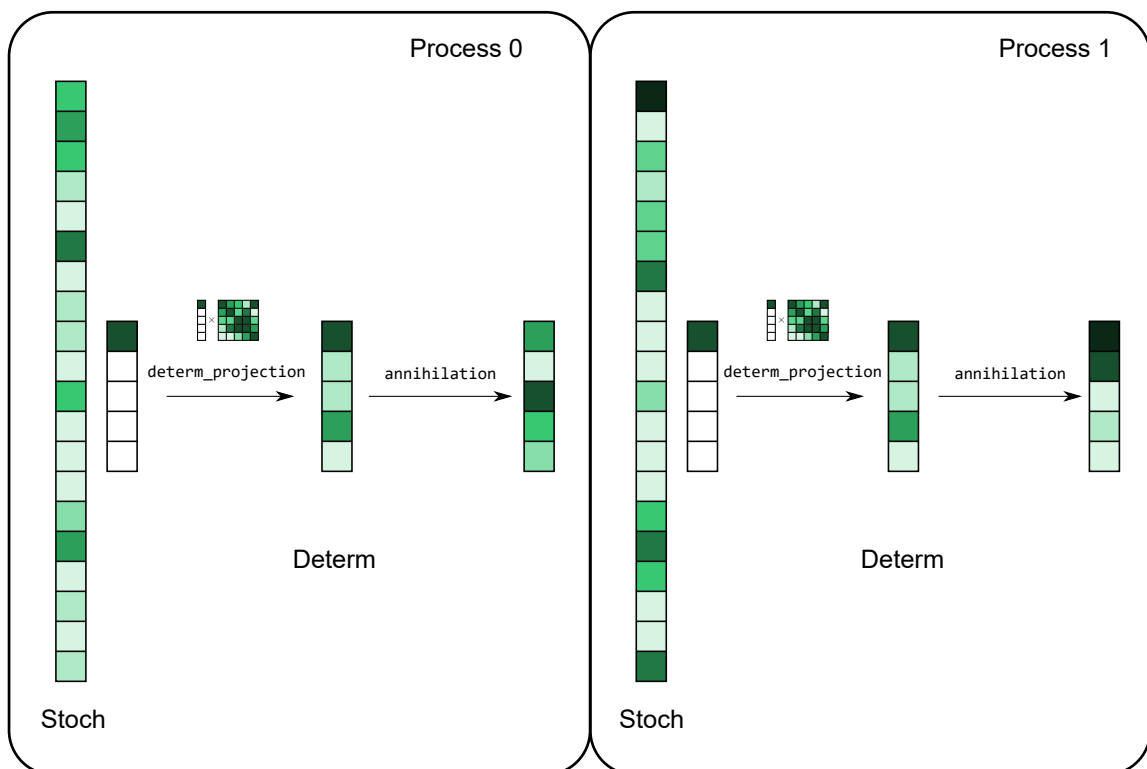


Fig. C.1 Here we illustrate a simple calculation with 2 MPI processes, each with 20 occupied stochastic states and 5 identical deterministic states, with only the first, reference, state occupied in the first semi-stochastic iteration. After the identical, deterministic Hamiltonian projection, the annihilation process brings spawns onto the deterministic states *only* from the local process.

and also complicate the implementation for a small reduction in cluster sampling noise, that can be alternatively decreased by increasing the number of stochastic samples taken, like in the ‘even selection’ approach [51]. For this reason, we chose instead to focus on the integrated sampling scheme in [Section 5.4.3](#), whose implementation is closer to the spirit of the MPI parallelism of the original CCMC algorithm.

References

- [1] John P. Perdew and Karla Schmidt. Jacob’s ladder of density functional approximations for the exchange-correlation energy. *AIP Conference Proceedings*, 577(1):1–20, July 2001.
- [2] C. C. J. Roothaan. New Developments in Molecular Orbital Theory. *Reviews of Modern Physics*, 23(2):69–89, April 1951.
- [3] G. G. Hall and John Edward Lennard-Jones. The molecular orbital theory of chemical valency VIII. A method of calculating ionization potentials. *Proceedings of the Royal Society of London. Series A. Mathematical and Physical Sciences*, 205(1083):541–552, March 1951.
- [4] Chr. Møller and M. S. Plesset. Note on an Approximation Treatment for Many-Electron Systems. *Physical Review*, 46(7):618–622, October 1934.
- [5] Trygve Helgaker, Poul Jorgensen, and Jeppe Olsen. *Molecular Electronic-Structure Theory*. John Wiley & Sons, 2014.
- [6] Isaiah Shavitt and Rodney J. Bartlett. *Many-Body Methods in Chemistry and Physics: MBPT and Coupled-Cluster Theory*. Cambridge Molecular Science. Cambridge University Press, Cambridge, 2009.
- [7] Attila Szabo and Neil S. Ostlund. *Modern Quantum Chemistry: Introduction to Advanced Electronic Structure Theory*. Dover Publications, 2012.
- [8] G. C. Wick. The Evaluation of the Collision Matrix. *Physical Review*, 80(2):268–272, October 1950.
- [9] Francesco A. Evangelista. Automatic derivation of fermionic many-body theories based on general Fermi vacua, May 2022.
- [10] Krishnan Raghavachari, Gary W. Trucks, John A. Pople, and Martin Head-Gordon. A fifth-order perturbation comparison of electron correlation theories. *Chemical Physics Letters*, 157(6):479–483, May 1989.
- [11] Frank Jensen. *Introduction to Computational Chemistry*. John wiley & sons, 2017.
- [12] Dmitry I. Lyakh, Monika Musiał, Victor F. Lotrich, and Rodney J. Bartlett. Multireference Nature of Chemistry: The Coupled-Cluster View. *Chemical Reviews*, 112(1):182–243, January 2012.

- [13] W. Kohn. Nobel Lecture: Electronic structure of matter—wave functions and density functionals. *Reviews of Modern Physics*, 71(5):1253–1266, October 1999.
- [14] Peter J. Knowles and Nicholas C. Handy. A determinant based full configuration interaction program. *Computer Physics Communications*, 54(1):75–83, April 1989.
- [15] Jeppe Olsen, Björn O. Roos, Poul Jo/rgensen, and Hans Jo/rgen Aa. Jensen. Determinant based configuration interaction algorithms for complete and restricted configuration interaction spaces. *The Journal of Chemical Physics*, 89(4):2185–2192, August 1988.
- [16] C. David Sherrill and Henry F. Schaefer. The Configuration Interaction Method: Advances in Highly Correlated Approaches. In Per-Olov Löwdin, John R. Sabin, Michael C. Zerner, and Erkki Brändas, editors, *Advances in Quantum Chemistry*, volume 34, pages 143–269. Academic Press, January 1999.
- [17] Elda Rossi, Gian Luigi Bendazzoli, Stefano Evangelisti, and Daniel Maynau. A full-configuration benchmark for the N₂ molecule. *Chemical Physics Letters*, 310(5):530–536, September 1999.
- [18] Zhengting Gan, Daniel J. Grant, Robert J. Harrison, and David A. Dixon. The lowest energy states of the group-III A–group-V A heteronuclear diatomics: BN, BP, AlN, and AlP from full configuration interaction calculations. *The Journal of Chemical Physics*, 125(12):124311, September 2006.
- [19] Konstantinos D. Vogiatzis, Dongxia Ma, Jeppe Olsen, Laura Gagliardi, and Wibe A. de Jong. Pushing configuration-interaction to the limit: Towards massively parallel MCSCF calculations. *The Journal of Chemical Physics*, 147(18):184111, November 2017.
- [20] Stephen R. Langhoff and Ernest R. Davidson. Configuration interaction calculations on the nitrogen molecule. *International Journal of Quantum Chemistry*, 8(1):61–72, 1974.
- [21] John A. Pople, Martin Head-Gordon, and Krishnan Raghavachari. Quadratic configuration interaction. A general technique for determining electron correlation energies. *The Journal of Chemical Physics*, 87(10):5968–5975, November 1987.
- [22] E. Y. Loh, J. E. Gubernatis, R. T. Scalettar, S. R. White, D. J. Scalapino, and R. L. Sugar. Sign problem in the numerical simulation of many-electron systems. *Physical Review B*, 41(13):9301–9307, May 1990.
- [23] Eva Pavarini, Erik Koch, and Ulrich Schollwöck, editors. *Emergent Phenomena in Correlated Matter*, volume 3 of *Schriften des Forschungszentrums Jülich. Reihe modeling and simulation*. Forschungszentrum Jülich GmbH Zentralbibliothek, Verlag, Jülich, September 2013.
- [24] R. J. Needs, M. D. Towler, N. D. Drummond, and P. López Ríos. Continuum variational and diffusion quantum Monte Carlo calculations. *Journal of Physics: Condensed Matter*, 22(2):023201, December 2009.
- [25] James B. Anderson. A random-walk simulation of the Schrödinger equation: H+3. *The Journal of Chemical Physics*, 63(4):1499–1503, August 1975.

- [26] James B. Anderson. Quantum chemistry by random walk. $\text{H } ^2P$, $\text{H}_3^+ D_{3h} ^1A'_1$, $\text{H}_2 3\Sigma_u^+$, $\text{H}_4 1\Sigma_g^+$, $\text{Be } ^1S$. *The Journal of Chemical Physics*, 65(10):4121–4127, November 1976.
- [27] F. A. Reboredo, R. Q. Hood, and P. R. C. Kent. Self-healing diffusion quantum Monte Carlo algorithms: Direct reduction of the fermion sign error in electronic structure calculations. *Physical Review B*, 79(19):195117, May 2009.
- [28] Shiwei Zhang and Henry Krakauer. Quantum Monte Carlo Method using Phase-Free Random Walks with Slater Determinants. *Physical Review Letters*, 90(13):136401, April 2003.
- [29] George H. Booth, Alex J. W. Thom, and Ali Alavi. Fermion Monte Carlo without fixed nodes: A game of life, death, and annihilation in Slater determinant space. *The Journal of Chemical Physics*, 131(5):054106, August 2009.
- [30] Alex J. W. Thom. Stochastic Coupled Cluster Theory. *Physical Review Letters*, 105(26):263004, December 2010.
- [31] N. S. Blunt, T. W. Rogers, J. S. Spencer, and W. M. C. Foulkes. Density-matrix quantum Monte Carlo method. *Physical Review B*, 89(24):245124, June 2014.
- [32] Shiwei Zhang, J. Carlson, and J. E. Gubernatis. Constrained path Monte Carlo method for fermion ground states. *Physical Review B*, 55(12):7464–7477, March 1997.
- [33] Malliga Suewattana, Wirawan Purwanto, Shiwei Zhang, Henry Krakauer, and Eric J. Walter. Phaseless auxiliary-field quantum Monte Carlo calculations with plane waves and pseudopotentials: Applications to atoms and molecules. *Physical Review B*, 75(24):245123, June 2007.
- [34] J. S. Spencer, N. S. Blunt, and W. M.c. Foulkes. The sign problem and population dynamics in the full configuration interaction quantum Monte Carlo method. *The Journal of Chemical Physics*, 136(5):054110, February 2012.
- [35] James S. Spencer, Nick S. Blunt, Seonghoon Choi, Jiří Etrych, Maria-Andreea Filip, W. M. C. Foulkes, Ruth S. T. Franklin, Will J. Handley, Fionn D. Malone, Verena A. Neufeld, Roberto Di Remigio, Thomas W. Rogers, Charles J. C. Scott, James J. Shepherd, William A. Vigor, Joseph Weston, RuQing Xu, and Alex J. W. Thom. The HANDE-QMC Project: Open-Source Stochastic Quantum Chemistry from the Ground State Up. *Journal of Chemical Theory and Computation*, 15(3):1728–1742, March 2019.
- [36] Adam A. Holmes, Hitesh J. Changlani, and C. J. Umrigar. Efficient Heat-Bath Sampling in Fock Space. *Journal of Chemical Theory and Computation*, 12(4):1561–1571, April 2016.
- [37] Verena A. Neufeld and Alex J. W. Thom. Exciting Determinants in Quantum Monte Carlo: Loading the Dice with Fast, Low-Memory Weights. *Journal of Chemical Theory and Computation*, 15(1):127–140, January 2019.
- [38] Kai Guthier, Robert J. Anderson, Nick S. Blunt, Nikolay A. Bogdanov, Deidre Cleland, Nike Dattani, Werner Dobrazt, Khaldoon Ghanem, Peter Jeszenszki, Niklas Liebermann, Giovanni Li Manni, Alexander Y. Lozovoi, Hongjun Luo, Dongxia Ma, Florian Merz,

- Catherine Overy, Markus Rampp, Pradipta Kumar Samanta, Laurretta R. Schwarz, James J. Shepherd, Simon D. Smart, Eugenio Vitale, Oskar Weser, George H. Booth, and Ali Alavi. NECI: N-Electron Configuration Interaction with an emphasis on state-of-the-art stochastic methods. *The Journal of Chemical Physics*, 153(3):034107, July 2020.
- [39] James S. Spencer and Alex J. W. Thom. Developments in stochastic coupled cluster theory: The initiator approximation and application to the uniform electron gas. *The Journal of Chemical Physics*, 144(8):084108, February 2016.
- [40] H. Flyvbjerg and H. G. Petersen. Error estimates on averages of correlated data. *The Journal of Chemical Physics*, 91(1):461–466, July 1989.
- [41] Tom Ichibha, Verena A. Neufeld, Kenta Hongo, Ryo Maezono, and Alex J. W. Thom. Making the most of data: Quantum Monte Carlo postanalysis revisited. *Physical Review E*, 105(4):045313, April 2022.
- [42] Deidre Cleland, George H. Booth, and Ali Alavi. Communications: Survival of the fittest: Accelerating convergence in full configuration-interaction quantum Monte Carlo. *The Journal of Chemical Physics*, 132(4):041103, January 2010.
- [43] Nick S. Blunt. Communication: An efficient and accurate perturbative correction to initiator full configuration interaction quantum Monte Carlo. *The Journal of Chemical Physics*, 148(22):221101, June 2018.
- [44] Samuel M. Greene, Robert J. Webber, Jonathan Weare, and Timothy C. Berkelbach. Beyond Walkers in Stochastic Quantum Chemistry: Reducing Error Using Fast Randomized Iteration. *Journal of Chemical Theory and Computation*, 15(9):4834–4850, September 2019.
- [45] Samuel M. Greene, Robert J. Webber, Jonathan Weare, and Timothy C. Berkelbach. Improved Fast Randomized Iteration Approach to Full Configuration Interaction. *Journal of Chemical Theory and Computation*, 16(9):5572–5585, September 2020.
- [46] Samuel M. Greene, Robert J. Webber, James E. T. Smith, Jonathan Weare, and Timothy C. Berkelbach. Full Configuration Interaction Excited-State Energies in Large Active Spaces from Subspace Iteration with Repeated Random Sparsification, April 2022.
- [47] Lek-Heng Lim and Jonathan Weare. Fast Randomized Iteration: Diffusion Monte Carlo through the Lens of Numerical Linear Algebra. *SIAM Review*, 59(3):547–587, January 2017.
- [48] Verena A. Neufeld and Alex J. W. Thom. Accelerating Convergence in Fock Space Quantum Monte Carlo Methods. *Journal of Chemical Theory and Computation*, 16(3):1503–1510, March 2020.
- [49] Nick S. Blunt, Alex J. W. Thom, and Charles J. C. Scott. Preconditioning and Perturbative Estimators in Full Configuration Interaction Quantum Monte Carlo. *Journal of Chemical Theory and Computation*, 15(6):3537–3551, June 2019.
- [50] Ernest R. Davidson. The iterative calculation of a few of the lowest eigenvalues and corresponding eigenvectors of large real-symmetric matrices. *Journal of Computational Physics*, 17(1):87–94, January 1975.

- [51] Charles J. C. Scott and Alex J. W. Thom. Stochastic coupled cluster theory: Efficient sampling of the coupled cluster expansion. *The Journal of Chemical Physics*, 147(12):124105, September 2017.
- [52] Maria-Andreea Filip, Charles J. C. Scott, and Alex J. W. Thom. Multireference Stochastic Coupled Cluster. *Journal of Chemical Theory and Computation*, 15(12):6625–6635, December 2019.
- [53] R. W. Hamming. Error detecting and error correcting codes. *The Bell System Technical Journal*, 29(2):147–160, April 1950.
- [54] W. A. Burkhard and R. M. Keller. Some approaches to best-match file searching. *Communications of the ACM*, 16(4):230–236, April 1973.
- [55] Thom H. Dunning. Gaussian basis sets for use in correlated molecular calculations. I. The atoms boron through neon and hydrogen. *The Journal of Chemical Physics*, 90(2):1007–1023, January 1989.
- [56] Daniel G. A. Smith, Lori A. Burns, Andrew C. Simmonett, Robert M. Parrish, Matthew C. Schieber, Raimondas Galvelis, Peter Kraus, Holger Kruse, Roberto Di Remigio, Asem Alenaizan, Andrew M. James, Susi Lehtola, Jonathon P. Misiewicz, Maximilian Scheurer, Robert A. Shaw, Jeffrey B. Schriber, Yi Xie, Zachary L. Glick, Dominic A. Sirianni, Joseph Senan O’Brien, Jonathan M. Waldrop, Ashutosh Kumar, Edward G. Hohenstein, Benjamin P. Pritchard, Bernard R. Brooks, Henry F. Schaefer, Alexander Yu. Sokolov, Konrad Patkowski, A. Eugene DePrince, Uğur Bozkaya, Rollin A. King, Francesco A. Evangelista, Justin M. Turney, T. Daniel Crawford, and C. David Sherrill. PSI4 1.4: Open-source software for high-throughput quantum chemistry. *The Journal of Chemical Physics*, 152(18):184108, May 2020.
- [57] Qiming Sun, Timothy C. Berkelbach, Nick S. Blunt, George H. Booth, Sheng Guo, Zhendong Li, Junzi Liu, James D. McClain, Elvira R. Sayfutyarova, Sandeep Sharma, Sebastian Wouters, and Garnet Kin-Lic Chan. PySCF: The Python-based simulations of chemistry framework. *WIREs Computational Molecular Science*, 8(1):e1340, 2018.
- [58] George H. Booth, Simon D. Smart, and Ali Alavi. Linear-scaling and parallelisable algorithms for stochastic quantum chemistry. *Molecular Physics*, 112(14):1855–1869, July 2014.
- [59] Sebastian Wouters, Ward Poelmans, Paul W. Ayers, and Dimitri Van Neck. CheMPS2: A free open-source spin-adapted implementation of the density matrix renormalization group for ab initio quantum chemistry. *Computer Physics Communications*, 185(6):1501–1514, June 2014.
- [60] Sandeep Sharma. A general non-Abelian density matrix renormalization group algorithm with application to the C₂ dimer. *The Journal of Chemical Physics*, 142(2):024107, January 2015.
- [61] A. J. C. Varandas. Extrapolation to the complete-basis-set limit and the implications of avoided crossings: The $X^1\Sigma_g^+$, $B^1\Delta_g$, and $B'^1\Sigma_g^+$ states of C₂. *The Journal of Chemical Physics*, 129(23):234103, December 2008.

- [62] George H. Booth, Deidre Cleland, Alex J. W. Thom, and Ali Alavi. Breaking the carbon dimer: The challenges of multiple bond dissociation with full configuration interaction quantum Monte Carlo methods. *The Journal of Chemical Physics*, 135(8):084104, August 2011.
- [63] Piotr Piecuch, Stanisław A. Kucharski, Karol Kowalski, and Monika Musiał. Efficient computer implementation of the renormalized coupled-cluster methods: The R-CCSD[T], R-CCSD(T), CR-CCSD[T], and CR-CCSD(T) approaches. *Computer Physics Communications*, 149(2):71–96, December 2002.
- [64] Giuseppe M. J. Barca, Colleen Bertoni, Laura Carrington, Dipayan Datta, Nuwan De Silva, J. Emiliano Deustua, Dmitri G. Fedorov, Jeffrey R. Gour, Anastasia O. Gunina, Emilie Guidez, Taylor Harville, Stephan Irle, Joe Ivanic, Karol Kowalski, Sarom S. Leang, Hui Li, Wei Li, Jesse J. Lutz, Ilias Magoulas, Joani Mato, Vladimir Mironov, Hiroya Nakata, Buu Q. Pham, Piotr Piecuch, David Poole, Spencer R. Pruitt, Alistair P. Rendell, Luke B. Roskop, Klaus Ruedenberg, Tosaporn Sattasathuchana, Michael W. Schmidt, Jun Shen, Lyudmila Slipchenko, Masha Sosonkina, Vaibhav Sundriyal, Ananta Tiwari, Jorge L. Galvez Vallejo, Bryce Westheimer, Marta Wloch, Peng Xu, Federico Zahariev, and Mark S. Gordon. Recent developments in the general atomic and molecular electronic structure system. *The Journal of Chemical Physics*, 152(15):154102, April 2020.
- [65] Kerstin. Andersson, Per Aake. Malmqvist, Bjoern O. Roos, Andrzej J. Sadlej, and Krzysztof. Wolinski. Second-order perturbation theory with a CASSCF reference function. *The Journal of Physical Chemistry*, 94(14):5483–5488, July 1990.
- [66] C. Angeli, R. Cimiraglia, S. Evangelisti, T. Leininger, and J.-P. Malrieu. Introduction of n-electron valence states for multireference perturbation theory. *The Journal of Chemical Physics*, 114(23):10252–10264, June 2001.
- [67] Celestino Angeli, Renzo Cimiraglia, and Jean-Paul Malrieu. N-electron valence state perturbation theory: A fast implementation of the strongly contracted variant. *Chemical Physics Letters*, 350(3):297–305, December 2001.
- [68] Celestino Angeli, Renzo Cimiraglia, and Jean-Paul Malrieu. N-electron valence state perturbation theory: A spinless formulation and an efficient implementation of the strongly contracted and of the partially contracted variants. *The Journal of Chemical Physics*, 117(20):9138–9153, November 2002.
- [69] Josef Paldus. Externally and internally corrected coupled cluster approaches: An overview. *Journal of Mathematical Chemistry*, 55(2):477–502, February 2017.
- [70] Ilias Magoulas, Karthik Gururangan, Piotr Piecuch, J. Emiliano Deustua, and Jun Shen. Is Externally Corrected Coupled Cluster Always Better Than the Underlying Truncated Configuration Interaction? *Journal of Chemical Theory and Computation*, 17(7):4006–4027, July 2021.
- [71] Gustavo J. R. Aroeira, Madeline M. Davis, Justin M. Turney, and Henry F. Schaefer. Coupled Cluster Externally Corrected by Adaptive Configuration Interaction. *Journal of Chemical Theory and Computation*, 17(1):182–190, January 2021.

- [72] Jeffrey B. Schriber and Francesco A. Evangelista. Communication: An adaptive configuration interaction approach for strongly correlated electrons with tunable accuracy. *The Journal of Chemical Physics*, 144(16):161106, April 2016.
- [73] J. Emiliano Deustua, Jun Shen, and Piotr Piecuch. Converging High-Level Coupled-Cluster Energetics by Monte Carlo Sampling and Moment Expansions. *Physical Review Letters*, 119(22):223003, November 2017.
- [74] J. Emiliano Deustua, Ilias Magoulas, Jun Shen, and Piotr Piecuch. Communication: Approaching exact quantum chemistry by cluster analysis of full configuration interaction quantum Monte Carlo wave functions. *The Journal of Chemical Physics*, 149(15):151101, October 2018.
- [75] J. Emiliano Deustua, Jun Shen, and Piotr Piecuch. High-level coupled-cluster energetics by Monte Carlo sampling and moment expansions: Further details and comparisons. *The Journal of Chemical Physics*, 154(12):124103, March 2021.
- [76] Jun Shen and Piotr Piecuch. Combining active-space coupled-cluster methods with moment energy corrections via the CC(P ; Q) methodology, with benchmark calculations for biradical transition states. *The Journal of Chemical Physics*, 136(14):144104, April 2012.
- [77] Tomoko Kinoshita, Osamu Hino, and Rodney J. Bartlett. Coupled-cluster method tailored by configuration interaction. *The Journal of Chemical Physics*, 123(7):074106, August 2005.
- [78] Maximilian Mörchen, Leon Freitag, and Markus Reiher. Tailored coupled cluster theory in varying correlation regimes. *The Journal of Chemical Physics*, 153(24):244113, December 2020.
- [79] Eugenio Vitale, Ali Alavi, and Daniel Kats. FCIQMC-Tailored Distinguishable Cluster Approach. *Journal of Chemical Theory and Computation*, 16(9):5621–5634, September 2020.
- [80] Deidre Cleland, George H. Booth, Catherine Overy, and Ali Alavi. Taming the First-Row Diatomics: A Full Configuration Interaction Quantum Monte Carlo Study. *Journal of Chemical Theory and Computation*, 8(11):4138–4152, November 2012.
- [81] Robert E. Thomas, Catherine Overy, George H. Booth, and Ali Alavi. Symmetry breaking and broken ergodicity in full configuration interaction quantum monte carlo. 10(5):1915–1922.
- [82] Jeremy M. Merritt, Vladimir E. Bondybey, and Michael C. Heaven. Beryllium Dimer—Caught in the Act of Bonding. *Science*, 324(5934):1548–1551, June 2009.
- [83] Muammar El Khatib, Gian Luigi Bendazzoli, Stefano Evangelisti, Wissam Helal, Thierry Leininger, Lorenzo Tenti, and Celestino Angeli. Beryllium Dimer: A Bond Based on Non-Dynamical Correlation. *The Journal of Physical Chemistry A*, 118(33):6664–6673, August 2014.

- [84] Wissam Helal, Stefano Evangelisti, Thierry Leininger, and Antonio Monari. A FCI benchmark on beryllium dimer: The lowest singlet and triplet states. *Chemical Physics Letters*, 568-569:49–54, May 2013.
- [85] Sandeep Sharma, Takeshi Yanai, George H. Booth, C. J. Umrigar, and Garnet Kin-Lic Chan. Spectroscopic accuracy directly from quantum chemistry: Application to ground and excited states of beryllium dimer. *The Journal of Chemical Physics*, 140(10):104112, March 2014.
- [86] Vladimir V. Meshkov, Andrey V. Stolyarov, Michael C. Heaven, Carl Haugen, and Robert J. LeRoy. Direct-potential-fit analyses yield improved empirical potentials for the ground $X^1\Sigma_g^+$ state of Be_2 . *The Journal of Chemical Physics*, 140(6):064315, February 2014.
- [87] X. W. Sheng, X. Y. Kuang, P. Li, and K. T. Tang. Analyzing and modeling the interaction potential of the ground-state beryllium dimer. *Physical Review A*, 88(2):022517, August 2013.
- [88] Mirjana Eckert-Maksić, Mario Vazdar, Mario Barbatti, Hans Lischka, and Zvonimir B. Maksić. Automerization reaction of cyclobutadiene and its barrier height: An ab initio benchmark multireference average-quadratic coupled cluster study. *The Journal of Chemical Physics*, 125(6):064310, August 2006.
- [89] David W. Whitman and Barry K. Carpenter. Limits on the activation parameters for automerization of cyclobutadiene-1, 2- d_2 . *Journal of the American Chemical Society*, 104(23):6473–6474, November 1982.
- [90] Barry K. Carpenter. Heavy-atom tunneling as the dominant pathway in a solution-phase reaction? Bond shift in antiaromatic annulenes. *Journal of the American Chemical Society*, 105(6):1700–1701, March 1983.
- [91] Hans-Joachim Werner, Peter J. Knowles, Frederick R. Manby, Joshua A. Black, Klaus Doll, Andreas Heßelmann, Daniel Kats, Andreas Köhn, Tatiana Korona, David A. Kreplin, Qianli Ma, Thomas F. Miller, Alexander Mitrushchenkov, Kirk A. Peterson, Iakov Polyak, Guntram Rauhut, and Marat Sibaev. The Molpro quantum chemistry package. *The Journal of Chemical Physics*, 152(14):144107, April 2020.
- [92] Dmitry I. Lyakh, Victor F. Lotrich, and Rodney J. Bartlett. The ‘tailored’ CCSD(T) description of the automerization of cyclobutadiene. *Chemical Physics Letters*, 501(4):166–171, January 2011.
- [93] Xiangzhu Li and Josef Paldus. Accounting for the exact degeneracy and quasidegeneracy in the automerization of cyclobutadiene via multireference coupled-cluster methods. *The Journal of Chemical Physics*, 131(11):114103, September 2009.
- [94] Kiran Bhaskaran-Nair, Ondřej Demel, and Jiří Pittner. Multireference state-specific Mukherjee’s coupled cluster method with noniterative triexcitations. *The Journal of Chemical Physics*, 129(18):184105, November 2008.
- [95] Tianyuan Zhang and Francesco A. Evangelista. A Deterministic Projector Configuration Interaction Approach for the Ground State of Quantum Many-Body Systems. *Journal of Chemical Theory and Computation*, 12(9):4326–4337, September 2016.

- [96] John P. Boyd. *Chebyshev and Fourier Spectral Methods*. Courier Corporation, 2001.
- [97] S. Geršgorin. Über die Abgrenzung der Eigenwerte einer Matrix. *Bulletin de l'Académie des Sciences de l'URSS. Classe des sciences mathématiques et na*, (6):749–754, 1931.
- [98] Mingrui Yang, Elke Pahl, and Joachim Brand. Improved walker population control for full configuration interaction quantum Monte Carlo. *The Journal of Chemical Physics*, 153(17):174103, November 2020.
- [99] W. A. Vigor, J. S. Spencer, M. J. Bearpark, and A. J. W. Thom. Understanding and improving the efficiency of full configuration interaction quantum Monte Carlo. *The Journal of Chemical Physics*, 144(9):094110, March 2016.
- [100] F. R. Petruzielo, A. A. Holmes, Hitesh J. Changlani, M. P. Nightingale, and C. J. Umrigar. Semistochastic Projector Monte Carlo Method. *Physical Review Letters*, 109(23):230201, December 2012.
- [101] N. S. Blunt, Simon D. Smart, J. a. F. Kersten, J. S. Spencer, George H. Booth, and Ali Alavi. Semi-stochastic full configuration interaction quantum Monte Carlo: Developments and application. *The Journal of Chemical Physics*, 142(18):184107, May 2015.
- [102] J. S. Spencer, V. A. Neufeld, W. A. Vigor, R. S. T. Franklin, and A. J. W. Thom. Large scale parallelization in stochastic coupled cluster. *The Journal of Chemical Physics*, 149(20):204103, November 2018.
- [103] J. Čížek, J. Paldus, and L. Šroubková. Cluster expansion analysis for delocalized systems. *International Journal of Quantum Chemistry*, 3(2):149–167, 1969.
- [104] Donald E. Knuth. *The Art of Computer Programming, Volume 3: Sorting and Searching*, volume 3. Addison-Wesley, 2 edition, June 1998.
- [105] Timothy J. Lee and Gustavo E. Scuseria. Achieving Chemical Accuracy with Coupled-Cluster Theory. In Stephen R. Langhoff, editor, *Quantum Mechanical Electronic Structure Calculations with Chemical Accuracy*, Understanding Chemical Reactivity, pages 47–108. Springer Netherlands, Dordrecht, 1995.
- [106] Henrik R. Larsson, Huanchen Zhai, Cyrus J. Umrigar, and Garnet Kin-Lic Chan. The chromium dimer: closing a chapter of quantum chemistry, 2022.
- [107] Johannes Hachmann, Jonathan J. Dorando, Michael Avilés, and Garnet Kin-Lic Chan. The radical character of the acenes: A density matrix renormalization group study. *The Journal of Chemical Physics*, 127(13):134309, oct 2007.
- [108] R. Kosloff and H. Tal-Ezer. A direct relaxation method for calculating eigenfunctions and eigenvalues of the schrödinger equation on a grid. *Chemical Physics Letters*, 127(3):223–230, June 1986.
- [109] Raymond G. Ayoub. Paolo Ruffini's contributions to the quintic. *Archive for History of Exact Sciences*, 23(3):253–277, 1980.

-
- [110] K. F. Riley, M. P. Hobson, and S. J. Bence. *Mathematical Methods for Physics and Engineering: A Comprehensive Guide*. Cambridge University Press, 3 edition, 2006.
 - [111] Peter Gustav Lejeune Dirichlet. Sur la convergence des séries trigonométriques qui servent à représenter une fonction arbitraire entre des limites données, 2008.